



저작자표시-비영리-변경금지 2.0 대한민국

이용자는 아래의 조건을 따르는 경우에 한하여 자유롭게

- 이 저작물을 복제, 배포, 전송, 전시, 공연 및 방송할 수 있습니다.

다음과 같은 조건을 따라야 합니다:



저작자표시. 귀하는 원저작자를 표시하여야 합니다.



비영리. 귀하는 이 저작물을 영리 목적으로 이용할 수 없습니다.



변경금지. 귀하는 이 저작물을 개작, 변형 또는 가공할 수 없습니다.

- 귀하는, 이 저작물의 재이용이나 배포의 경우, 이 저작물에 적용된 이용허락조건을 명확하게 나타내어야 합니다.
- 저작권자로부터 별도의 허가를 받으면 이러한 조건들은 적용되지 않습니다.

저작권법에 따른 이용자의 권리는 위의 내용에 의하여 영향을 받지 않습니다.

이것은 [이용허락규약\(Legal Code\)](#)을 이해하기 쉽게 요약한 것입니다.

[Disclaimer](#)

공학박사 학위논문

**Development of optical and electrical
neural stimulators for advanced neural
engineering applications**

첨단 신경 공학 응용을 위한 광학 및 전기 신경
자극기 개발

2020년 2월

서울대학교 융합과학기술대학원

융합과학부 나노융합전공

강 민 규

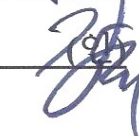
Development of optical and electrical neural stimulators for advanced neural engineering applications

지도 교수 : 송 윤 규

이 논문을 공학박사 학위논문으로 제출함
2020년 2월

서울대학교 융합과학기술대학원
융합과학부 나노융합전공
강 민 규

강민규의 공학박사 학위논문을 인준함
2020년 2월

위원장	김연상	
부위원장	송윤규	
위원	박원철	
위원	박상윤	
위원	강경태	

Abstract

Development of optical and electrical neural stimulators for advanced neural engineering applications

Mingyu Kang

Program in Nano Science and Technology

Graduate School of Convergence Science & Technology

Seoul National University

Electrical stimulation is the most common neural stimulation technique applied to modern medicine and improved over the decades. However, electrical stimulation generally affects neighboring neurons and makes the classification of single-cell mechanisms difficult. The development of optogenetics has complemented the shortcomings of this electrical stimulation. As stimuli were stimulated by light, stimuli became selectively possible, and neural recording and stimulation

became possible at the same time. However, the commonly used Channelrhodopsin-2 (ChR2) is stimulated by blue light, which makes it difficult to stimulate neurons in deep areas with low penetration depth. To overcome this, the near-infrared (NIR) region, which has deep penetration depth features, can facilitate neural stimulation in deeper areas.

For electrical neural stimulators, the properties of the electrodes are of great importance, especially the impedance of the electrodes and charge injection density are important factors in evaluating the electrodes. Among various electrode materials, the study on the poly(3,4-ethylenedioxythiophene) polystyrene sulfonate (PEDOT:PSS) is ongoing because it is biocompatible and has a low impedance.

This dissertation deals largely with the development of optical and electrical neural stimulators for advanced neural engineering applications. The study of PEDOT:PSS as electrode material in electrical neural stimulation has low impedance and high charge storage capacity (CSC) values. This dissertation paper shows that the mixture of PEDOT:PSS solution and ethanol has lower impedance and higher CSC value compared with the pristine PEDOT:PSS material. This result is due to the acetic acid and increased doping of PEDOT due to ionization due

to increasing pH value.

The addition of ethanol also shows an improved crosslinking efficiency of the crosslinking agent (3-glycidyloxypropyl) trimethoxysilane (GOPS). Due to the addition of ethanol, the increased mechanical properties and stability of PEDOT: PSS-GOPS, even at small amounts of GOPS, can be more easily used as neural stimulators. Fluorescent changes through stimulation experiments of mammalian cells (HEK 293 cells) expressing the fluorescent voltage indicator (Bongwoori-R3) confirmed the feasibility of PEDOT: PSS electrodes.

Finally, this dissertation deals with the development of a technique that combines NIR-operated photovoltaic cells with blue LEDs to stimulate neurons in deep regions using optogenetics. In the previous study, the simple combination of NIR photovoltaic cells and blue LEDs made it difficult to stimulate the neurons deeper because the direction of the NIR coincided with the direction of blue light emission. However, in this study, through-hole vias are applied to NIR photovoltaic cells using various semiconductor processes and solution processes, the NIR direction and the blue light direction of LEDs can be changed to enable a deeper neural stimulation. In addition, it was confirmed that the stimulator combined with the photovoltaic cell and the LED stimulated

ChR2-expressed mammalian cells (HEK 293 cells) and neurons.

Keywords: Neural Stimulator, Optogenetics, Photovoltaic cell, light-emitting diode, PEDOT:PSS, GOPS

Student Number: 2009-22457

Contents

ABSTRACT	I
LIST OF FIGURES	X
LIST OF TABLE.....	XVIII
CHAPTER 1. INTRODUCTION.....	1
1.1 Neural stimulation using electrical methods.....	1
1.2 Optogenetics.....	9
CHAPTER 2. ENHANCED THE ELECTROCHEMICAL PROPERTIES OF PEDOT:PSS ELECTRODE BY ETHANOL FOR NEURAL ELECTRODE INTERFACE.....	12
2.1 Introduction	12
2.2 Materials and methods	15
2.2.1 Sample preparation	15
2.2.2 Electrical characterization.....	16

2.2.3 Characterization of PEDOT:PSS.....	16
2.2.4 Micro pattern of PEDOT:PSS.....	17
2.2.5 Electrochemical analysis.....	21
2.2.6 Cell culture and transfection	21
2.2.7 Stimulation and imaging.....	22
2.3 Results	24
2.3.1 Electrical characteristics.....	24
2.3.2 FTIR analysis.....	26
2.3.3 XPS analysis.....	31
2.3.4 Raman spectrum analysis.....	36
2.3.5 Impedance & CSC measurement.....	39
2.3.6 Fluorescent voltage imaging of cultured mammalian cells stimulated by the PEDOT:PSS electrode	45
2.4 Discussion.....	49
 CHAPTER 3. ENHANCED THE STABILITY AND ELECTROCHEMICAL PROPERTIES OF PEDOT:PSS-GOPS ELECTRODE BY ETHANOL FOR NEURAL ELECTRODE INTERFACE.....	 51

3.1 Introduction	51
3.2 Materials and methods	54
3.2.1 Sample preparation	54
3.2.2 Electrical characterization.....	54
3.2.3 Characterization of PEDOT:PSS.....	55
3.2.4 Mechanical properties measurement.....	56
3.2.5 Micro pattern of PEDOT:PSS film	59
3.2.6 Electrochemical analysis.....	60
3.2.7 Cell culture and transfection	60
3.2.8 Stimulation and imaging.....	61
3.3 Results	63
3.3.1 Electrical characteristics of PEDOT:PSS-GOPS	63
3.3.2 FTIR analysis of PEDOT:PSS-GOPS	67
3.3.3 Contact angle of PEDOT:PSS-GOPS	71
3.3.4 UV spectrum of PEDOT:PSS-GOPS	73
3.3.5 Raman spectrum of PEDOT:PSS-GOPS	76
3.3.6 Surface roughness of PEDOT:PSS film	78
3.3.7 Mechanical properties of PEDOT:PSS-GOPS.....	80
3.3.8 Impedance & CSC measurement of PEDOT:PSS-GOPS.....	84

3.3.9 Fluorescent voltage imaging of cultured mammalian cells stimulated by the PEDOT:PSS electrode.....	88
3.4 Discussion.....	94

**CHAPTER 4. DEVELOPMENT OF AN OPTOELECTRONIC
NEURAL STIMULATOR COMBINED WITH A
PHOTOVOLTAIC CELL AND A LIGHT EMITTING DIODE
FOR OPTOGENETIC APPLICATION..... 97**

4.1 Introduction	97
4.2 Materials and methods.....	102
4.2.1 Light-emitting diode (LED) and photovoltaic cell (PV)	102
4.2.2 Fabrication process of PV with through-hole via	106
4.2.2.1 Making and passivation of the deep hole of PV.....	106
4.2.2.2 Ink-jet printing to fill the hole with metal	118
4.2.2.3 Lamination & Lapping.....	128
4.2.2.4 Back-side process & Dicing	131
4.2.3 LED fabrication process	134
4.2.4 Integration PV and LED	137
4.2.5 Light source and measurement	137

4.2.6 HEK cell culture and ChR2 expression for in vitro	
electrophysiology experiment.....	140
4.2.7 Neuron cell culture and ChR2 Expression for in vitro	
electrophysiology experiment.....	141
4.2.8 Whole-cell patch-clamp.....	142
4.3 Results	145
4.3.1 The characterization of PV	145
4.3.2 The characterization of LED	148
4.3.3 Optoelectronic neural stimulator	150
4.3.4 In-vitro experiment	157
4.3.4.1 HEK cell	157
4.3.4.2 Neuron.....	162
4.4 Discussion	167
REFERENCES	168
국문 초록.....	188

List of figures

Figure 1. 1 Simplified Randles models.	5
Figure 1. 2 Structure of ChR2 by ref. [28].	11
Figure 2. 1 Fabrication process flow of PEDOT:PSS electrode.....	20
Figure 2. 2 (a) Thickness, surface resistance and (b) conductivity of the PEDOT:PSS film according to ethanol concentration ratio.	25
Figure 2. 3 FTIR spectra from 2000 cm^{-1} to 3000 cm^{-1} of PEDOT:PSS depending on ethanol concentration ratio.	28
Figure 2. 4 FTIR spectra from 400 cm^{-1} to 2000 cm^{-1} of PEDOT:PSS depending on ethanol concentration ratio.	29
Figure 2. 5 Oxidation of ethanol.	30
Figure 2. 6 XPS spectra of (a) S (2p), (b) C (1s), and (c) O (1s) and (d) XPS survey level S (2p), C (1s), and O (1s) spectra of pristine PH1000 and PEDOT:PSS with ethanol.	33
Figure 2. 7 The pH concentration according to the ethanol mixing ratio in the PH1000 solution.....	34
Figure 2. 8 Schematic of ethanol solvent doping.	35
Figure 2. 9 Raman spectra of PEDOT:PSS thin films with and without ethanol.....	38
Figure 2. 10 PEDOT:PSS electrode with a diameter 40 μm	42
Figure 2. 11 (a) Impedance from frequency 10^0 Hz to 10^5 Hz and (b) the electrochemical impedance spectroscopy according to the number of coatings	

under the conditions of 50 wt % ratio of ethanol and pristine PH1000 without ethanol after post-treatment of DMSO.....	43
Figure 2. 12 (a) Plotted CV graph and (b) thickness and CSC of PEDOT:PSS according to the number of coatings under the conditions of 50 wt % ratio of ethanol and pristine PH1000 without ethanol after post-treatment of DMSO.	44
Figure 2. 13 An epifluorescence image showing HEK 293 cells expressing a fluorescent voltage indicator (Bongwoori-R3) (a) before and (b) after electrical stimulation to current of 10 μ A. The dotted circle in (a) indicates the PEDOT:PSS electrode. Each dotted circle in (b) represents a HEK 293 cell. 47	47
Figure 2. 14 Voltage-dependent fluorescence changes with varying current amplitudes from cells depicted in figure 2.13 (b).	48
Figure 3. 1 A schematic diagram of adhesion of AFM tip with radius, R, for modulus measurement of PEDOT:PSS thin film.	58
Figure 3. 2 (a) Thickness, surface resistance and (b) conductivity of the PEDOT:PSS film according to ethanol concentration.	65
Figure 3. 3 (a) Thickness, (b) surface resistance and (c) conductivity of the PEDOT:PSS film according to GOPS concentration.	66
Figure 3. 4 FTIR spectra from 400 cm^{-1} to 4000 cm^{-1} of PEDOT:PSS with 1 wt% of GOPS depending on ethanol concentration ratio.....	69
Figure 3. 5 (a) The pH concentration according to the ethanol mixing ratio in the PH1000 solution, (b) hydrolysis and condensation of trimethoxysilane of GOPS.....	70

Figure 3. 6 Contact angle for water on a glass substrate coated with PEDOT: PSS according to ethanol concentration ratio at 1 wt % of GOPS.....	72
Figure 3. 7 Normalized absorbance at wavelengths from 200 nm to 1000 nm, depending on the ethanol concentration ratio.....	75
Figure 3. 8 Raman spectra of PEDOT:PSS thin films with and without ethanol at 1 wt% of GOPS.	77
Figure 3. 9 Atomic force microscopy images of the topography PEDOT:PSS thin films mixed with (a) 0 wt%, (b) 30 wt% and (c) 50 wt% of ethanol concentration at 1 wt% of GOPS. The measured size of the topography is 1 $\mu\text{m} \times 1 \mu\text{m}$	79
Figure 3. 10 The modulus of PEDOT:PSS film measured by AFM indentation for the DMT models according to (a) the ethanol concentration ratio at 1 wt % of GOPS. (b) The modulus of PEDOT:PSS film and GOPS molar ratio of PSS according to GOPS concentration ratio at 30 wt % of ethanol.	82
Figure 3. 11 Surface image of PEDOT:PSS with GOPS 0.1 wt % (a) with and (b) without ethanol after sonication for 5 min.....	83
Figure 3. 12 Impedance of PEDOT:PSS film from frequency 10^0 Hz to 10^5 Hz the conditions of 0.1 wt% & 1 wt% ratio of GOPS with 30 wt % of ethanol concentration, 1 wt% ratio of GOPS without ethanol and gold.	86
Figure 3. 13 (a) Cyclic voltammetry (CV) curve for PEDOT:PSS with ethanol at 0.1 wt % and 1 wt % of GOPS and without ethanol at 1 wt % of GOPS. (b) charge storage capacity for cathodic and anodic calculated by CV.....	87
Figure 3. 14 Fluorescent voltage imaging of HEK 293 cells expressing a	

fluorescent voltage indicator (Bongwoori-R3) responding to current stimuli of (a) 3 μ A, (b) 5 μ A, (c) 7 μ A, (d) 10 μ A, (e) 15 μ A, and (f) 20 μ A from PEDOT:PSS-Ethanol electrode.....	90
Figure 3. 15 (a-d) Voltage-dependent fluorescence changes with varying current amplitudes from cells depicted in figure 3.14 (f). Inset in (a) shows the current input waveform used for the experiment.	91
Figure 3. 16 Fluorescent voltage imaging of HEK 293 cells expressing a fluorescent voltage indicator (Bongwoori-R3) over time after stimulation with current stimuli of 20 μ A.....	92
Figure 3. 17 Fluorescence traces acquired from area 1-4 with a current amplitude of (a) 5 μ A, (b) 7 μ A, (c) 10 μ A and (d) 20 μ A.....	93
Figure 4. 1 Comparison of previously studied PV-LED Stimulator with Stimulator combined PV with through-hole via and LED (ref. [123]).	101
Figure 4. 2 Structure of (a) PV and (b) LED.....	104
Figure 4. 3 Schematic design of the bonding of the LED to the PV cell and the light pathway through the optoelectronic neural stimulator. Incident NIR light is transmitted through the stimulator and converted to blue light.....	105
Figure 4. 4 (a,b) Etched thickness of photoresist and GaAs and (c,d) etching rate of photoresist and GaAs and selectivity in 30 μ m and 50 μ m hole sizes after ICP dry etching for 4 min according to different gas combinations.	111
Figure 4. 5 (a,b) Etched thickness of photoresist and GaAs and (c,d) etching rate of photoresist and GaAs and selectivity in 30 μ m and 50 μ m hole sizes after ICP dry etching for 4 min according to the gas ratio of Cl ₂ and BCl ₃ . .	113

Figure 4. 6 Cross-section image of SEM after ICP dry etching for 30 minutes under different process conditions using BCl_3 and Cl_2 gas.	114
Figure 4. 7 Cross-section image of SEM after ICP dry etching for 30 minutes according to RF power when the BCl_3 and Cl_2 gas ratio is 1 to 1.	115
Figure 4. 8 Cross-section image of SEM of the etched and passivated hole of GaAs after ICP dry etching for 50 min and PECVD process for deposition of Si_3N_4	116
Figure 4. 9 Surface image of (a) photoresist patterned for patterning SiN after PECVD process using photolithography and (b) Si_3N_4 patterned after wet-etching SiN and removing photoresist.	117
Figure 4. 10 Surface image according to the number of silver ink drops in the etched deep hole.	121
Figure 4. 11 Contact image for water on a glass substrate before and after FC film coating.	122
Figure 4. 12 Surface optical image of (a) photoresist patterned PV substrate around the deep hole and the inside of hole before FC film coating and (b) photoresist removed PV substrate after FC film coating.	123
Figure 4. 13 SEM (a) surface and (b) cross-section image when filling up 300 drops of silver inks in the deep hole by multi-drop method using inkjet printing and sintered in a convection oven at a temperature of $150\text{ }^\circ\text{C}$	124
Figure 4. 14 SEM (a) surface and (b) cross-section image when filling up 350 drops of silver inks in the deep hole by multi-drop method using inkjet printing and sintered in vacuum hot plate oven at a temperature of $150\text{ }^\circ\text{C}$ and	

a vacuum of 25 mTorr.	125
Figure 4. 15 SEM surface image according to drop count when silver ink is filled in the deep hole by single drop method.	126
Figure 4. 16 SEM (a) surface and (b) cross-section image when filling up 300 drops of silver inks in the deep hole by a single-drop method using inkjet printing and sintered in a convection oven at a temperature of 150 °C.	127
Figure 4. 17 Surface image of PV cell laminated using (a) elastomer and (b) hard material after the lapping process.	130
Figure 4. 18 Schematic illustration of the fabrication process of PV.	133
Figure 4. 19 Schematic illustration of the fabrication process of LED.	136
Figure 4. 20 (a) Schematic illustration and (b) actual image of the optical setup.	139
Figure 4. 21 Schematic illustration of the optogenetics stimulation setup.	144
Figure 4. 22 Optical images of (a) back-side of the PV cell. (b) Relative efficiency according to wavelength 600 1000 nm; the largest efficiency between 830~850 nm. (c) Voltage-Current characteristics and (d) Fill factor and Efficiency of PV cell; the PV cell has a fill factor of 0.85 and an efficiency of 34.6% under 850 nm illumination at 6 mW.	147
Figure 4. 23 (a) Optical image of LED after dicing. (b) Spectrum of light emitted from the LED, the peak wavelength is 449.2 nm. (b) Current-voltage-power characteristics of LED. The turn-on-voltage of the LED is 2.4 V.	149
Figure 4. 24 Operating image of optoelectronic neural stimulator combined with PV cell and micro-LED by the NIR from the optical fiber.	152

Figure 4. 25 Size of the light spot according to distance from the PV-LED stimulator at the same exposure time of the CCD.....	153
Figure 4. 26 Size of the light spot according to distance from the PV-LED stimulator at the automatic exposure time of the CCD.	154
Figure 4. 27 Intensity line profile of emission of PV-LED stimulator obtained by the CCD image at 2mW of NIR power.	155
Figure 4. 28 Characteristics of the PV-LED device. (a) LED output power, Efficiency and (b) LED intensity according to NIR power.....	156
Figure 4. 29 Fluorescence image of a ChR2-EYFP expressed HEK293 cell.	159
Figure 4. 30 (a) Whole-cell voltage-clamp recording from ChR2-EYFP expressed HEK293 cell at different NIR power during 300 ms illumination at -80 mV holding potential. (b) Photocurrents of ChR2 with 850 nm laser power according to NIR power at -80 mV holding potential.....	160
Figure 4. 31 Current-voltage characteristics of ChR2 on emission of PV-LED stimulator according to holding potential at 16 mW of NIR power.....	161
Figure 4. 32 Fluorescence image of a ChR2-EYFP expressed Neuron. The scale is 10 μ m.....	164
Figure 4. 33 Whole-cell current-clamp recordings from ChR2-EYFP expressed neurons at different NIR power. (a) 10 ms and (b) 15 ms of LED exposure time. N : NIR Power, B : LED intensity.	165
Figure 4. 34 Emission intensity of PV-LED stimulator according to distance from the PV-LED stimulator at different NIR powers. Neural stimulation	

using the PV-LED stimulator is possible in the region above the red dashed
line..... 166

List of Table

Table 1. 1 Charge/phase and charge density threshold requirements for neural prostheses by ref. [4].	6
Table 1. 2 Properties of electrodes – 1.	7
Table 1. 3 Properties of electrodes – 2.	8
Table 4. 1 Conditions of ICP dry etching process according to different gas combinations.	110
Table 4. 2 Conditions of ICP dry etching process according to the gas ratio of Cl ₂ and BCl ₃	112

Chapter 1. Introduction

1.1 Neural stimulation using electrical methods

Neural stimulation technology intentionally regulates the activity of the nervous system to improve the quality of life of people suffering from severe paralysis or severe loss of various sensory organs. The cochlear implant system allows the patient to hear no sound because of the disease of the cochlea[1-3]. Deep brain stimulation (DBS) delivers periodic stimulation waves, which can successfully treat diseases that are characterized by uncontrollable, usually painful muscle spasms, such as Parkinson's disease, tremors, and stress disorders.

Neural stimulation is achieved by depolarizing the membrane of excitatory cells by electrodes. Depolarization is caused by the flow of ionic current between the reference and stimulation electrodes. As also shown in table 1.1, electrical thresholds are required to elicit useful functional responses in animals and humans [4]. That is, charge injection capacity is one of the important factors in the electrode performance. There are two ways to measure this: Charge Injection Capacity (CIS) and Charge Storage Capacity (CSC). CIC is the area divided by the value for the injected charge at the maximum voltage the electrode can drive. CSC

represents the area value of the value measured in a cyclic voltammetry (CV).

There are two major methods of charge injection: capacitive charge injection and faradaic charge injection. The capacitive mechanism does not transfer electrons between the electrode and the electrolyte, while the Faraday mechanism transfers electrons between the electrode and the electrolyte, causing reduction or oxidation. Capacitive charge injection results in charge redistribution when the electrode combines with the electrolyte. It creates a charged plane on the metal surface in the electrolyte as opposed to the charge on the metal electrode surface. Or because polar molecules such as water are oriented at the interface and the forward direction of the polar molecules separates the charge. The negative excess charge at the electrode surface and the positive charge in the electrolyte near the interface become the same, which is dielectric. Capacitive charge has the advantage of chemical stability, but it has a limited area, so it is possible to use a porous electrode [5, 6].

On the other hand, in the case of faradaic charge injection, redox reaction has high charge density but chemical instability. In the case of the commonly used iridium oxide, stimulation at excessive charge densities causes problems of peeling or decomposition[7]. Therefore,

each material has a limitation on charge injection, and it stimulates by balancing the charge in the stimulus manner like biphasic.

The Randles model represents a simple electrical equivalent of an electrode/electrolyte interface consisting of two elements, capacitive and Faraday[8]. Figure 1.1 shows the simplified Randles model circuit. Where C_{dl} , R_{ct} , and R_s represent double layer capacity, charge transfer resistance, and electrolyte resistance, respectively. Reducing the impedance is most important to reduce the power of the stimulus system. According to Randles model, to reduce the impedance, the electrode area must be increased or the electron transfer resistance must be decreased. Reducing the electrode impedance reduces power consumption and is a big advantage in implant systems. For this reason, many studies on electrodes focus on lowering impedance and increasing charge injection capacity. Tables 1.2 and 1.3 show information on impedance or charge injection capacity (or charge storage capacity) for various electrode materials.

Among many electrode materials, Poly(3,4-ethylenedioxythiophene):poly(styrenesulfonate) (PEDOT: PSS) is a conductive polymer that has the advantages of biocompatibility and low impedance. Unlike metal materials, PEDOT:PSS is a polymer, so electrical double layer effects are

affected by volume, not area[9]. As a result, the double-layer capacitance increases and the impedance decreases.

In chapter 2, the electrochemical properties of PEDOT:PSS by ethanol will be discussed. PEDOT:PSS also exhibits poor stability in aqueous environments. To solve this problem, (3-glycidyloxypropyl) trimethoxysilane (GOPS) crosslinking agents are mixed. In chapter 3, the efficiency assessment of GOPS cross-linker with ethanol will be discussed.

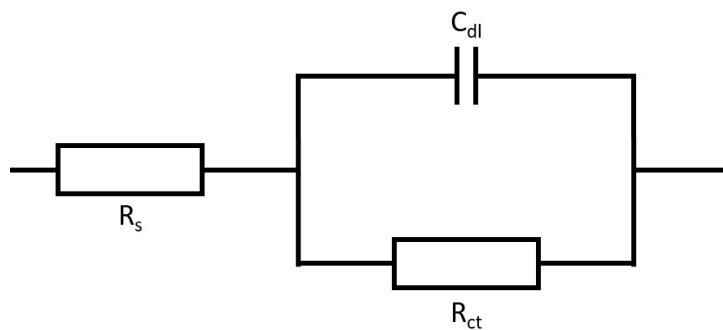


Figure 1. 1 Simplified Randles models.

Where C_{dl} , R_{ct} , R_s represent double layer capacity, charge transfer resistance, and electrolyte resistance, respectively.

Application	Placement	Species	Type	Threshold charge/phase (nC ph⁻¹)	Threshold charge density ($\mu\text{C cm}^{-2}$)	Pulse Width (μs)
Vision	Epi-retinal	Human	Surface	6-1120	5-570	1000
Vision	Epi-retinal	Human	Surface	24-100	80-306	2000
Vision	Optic nerve	Human	Surface	7-124	4-62	25-400
Vision	Intracortical	Human	Penetrating	0.4-4.6	190-2300	200
Vision	Cortical	Human	Surface	200000	11	200
Hearing	VCN	Cat	Penetrating	0.75-1.5	60-90	40-150
Hearing	AB	Human	Surface	10-200	2.6-52	300
Micturition	Intraspinal	Cat	Penetrating	9	4000	100
DBS	STN	Human	Penetrating	135-400	2.3-6.7	60-200
Motor	Intrafascicular	Cat	Penetrating	4	0.5	50
Motor	Sciatic nerve	Cat	Penetrating	5	96	200
Motor	Sciatic nerve	Cat	Surface	46	0.35	200

Table 1. 1 Charge/phase and charge density threshold requirements for neural prostheses by ref. [4].

	Area or Diameter	Impedance (kΩ, at 1 khz)	CIC (mC/cm²)	CSC (mC/cm²)	Ref.
Ti₃C₂	25 $\mu\text{m/d}$	219 \pm 60			[10]
	2500 μm^2	52 \pm 25			
Au	25 $\mu\text{m/d}$	865 \pm 125			[11]
	2500 μm^2	206 \pm 31			
	80 μm^2	2900	3.7	5.7	[12]
	300 $\mu\text{m/d}$	26.65 \pm 6.93		0.32 \pm 0.05	[13]
	20-150		0.3		[14]
	250 μm^2	7958 \pm 112			[15]
	30 $\mu\text{m/d}$	329 \pm 33			[16]
Pt	615 μm^2	1300	0.11		[17]
	0.03 cm ²		0.05-0.15		[18]
	0.05 cm ²		0.3		[4]
	1.4 cm ²			0.55	[13]
	20-150 $\mu\text{m/d}$		0.83		[19]
2000 $\mu\text{m/d}$		0.15			
PtIr	4500 μm^2		0.13		[20]
Ir	703 μm^2	980 \pm 80			[12]
EIROF	300 $\mu\text{m/d}$	1.41 \pm 1.1		24.19 \pm 6.21	[19]
	4500 μm^2		0.19		[20]
AIROF	2000 μm^2		3.3		[4]
	1.4 cm ²			23	[21]
TIROF			1		[18]
SIROF	0.05 cm ²		0.37		[4]
	0.05 cm ²		0.75		
	1.4 cm ²			2.8	
Stainless steel	0.81 mm ²	805.65 \pm 90.41			[22]
EGaln on SS	0.81 mm ²	718.34 \pm 59.58			

Table 1. 2 Properties of electrodes – 1.

	Area or Diameter	Impedance ($k\Omega$, at 1 khz)	CIC (mC/cm^2)	CSC (mC/cm^2)	Ref.
PEDOT:PSS/ SWCNT	30 $\mu m/d$	13-25	10.9 \pm 1.9		[23]
	30 $\mu m/d$	15.5 \pm 1.19		1.21 \pm 0.02	[15]
	30 $\mu m/d$	90.3 \pm 8.1			[14]
PEDOT/MW CNT	615 μm^2	12	7.74		[16]
PEDOT	615 μm^2		2.58		
PEDOT:PSS on Au	30 $\mu m/d$	20.0 \pm 2.13		0.81 \pm 0.05	[15]
	20-150		1.9		[13]
	2000		0.9		
	250 μm^2	97.1 \pm 1.1			[14]
PEDOT:PSS on PtIr	4500 μm^2		2.92		[19]
PEDOT/DC DPGYIGSR	703 μm^2	130 \pm 60			[20]
PEDOT:PSS on Pt	20-150		2.71		[13]
	100 $\mu m/d$		2.3 \pm 0.6		[24]
	200 $\mu m/d$		1.36 \pm 0.1		
PEDOT:pTS	200 $\mu m/d$		2.09 \pm 0.2		[25]
PEDOT:ClO ₄	200 $\mu m/d$		2.39 \pm 0.4		
Ppy/PSS/NG	1250 μm^2	15			[26]
Ppy/SLPF	1250 μm^2	360			
TiN	4000 μm^2		0.87	2.35	[27]
	4000 μm^2		0.9	2.35	
	30 $\mu m/d$	52.3 \pm 4.6		0.45 \pm 0.12	[15]
	1.4 cm^2			0.25	[4]
	80 μm^2	150	23	42	[11]
	30 $\mu m/d$		3.7 \pm 1.2		[23]

Table 1. 3 Properties of electrodes – 2.

1.2 Optogenetics

Optogenetics refers to the use of light to stimulate cells by genetically modifying light-sensitive ion channels in living cells. The general cell stimulation method is electrical stimulation, which causes depolarization by the electrode in proximity to the cell, thereby stimulating. However, the electrical stimulation method causes extensive stimulation of the cells around the electrode. In addition, since cell potentials are recorded, recording and stimulation cannot be performed at the same time. The use of optogenetics allows the simultaneous recording and stimulation of different types of recordings and stimuli, allowing the selective stimulation of only genetically modified cells.

Channelrhodopsin-2 (ChR2), the most commonly used in optogenetics, absorbs blue light at its maximum absorption and working spectrum at 480 nm as shown in figure 1.2 [28-31]. ChR2 was first used as an optogenetic tool in 2005 and has been widely used in the field.

Volvox-channelrhodopsin-1 (VChR1) [32] is also a red-shifted ChR variant, capable of generating action potentials at 589 nm. The neuronal expression of VChR1 is about three times lower than that of ChR2, but it contributes to the diversity of the optoelectronic toolbox due to its ability to be activated under yellow light illumination.

The neural stimulator using optogenetics has a relatively more complicated structure than an electrical electrode. In the case of the electrical method, a lot of research is being conducted on improving the performance of electrode materials. In the case of optogenetics, research is being conducted on how to transmit light efficiently and in what manner. Basically, the light source is generated by a laser or micro-LED and transmitted by an optical fiber or waveguide [33-36]. Alternatively, a micro-LED can be inserted directly. The combination of light stimulation and neuronal potential recording can provide a variety of alternatives to neural stimulation and recording [37-41].

In chapter 4, the development of devices for neuronal stimulation in deeper regions using optogenetics will be discussed. The applicable blue wavelength of ChR2 does not penetrate deep into the brain. To overcome this, NIR photovoltaic with deep brain penetration and LEDs were combined. In particular, photovoltaic cells have been applied through-hole via to enable stimulation in deeper regions.

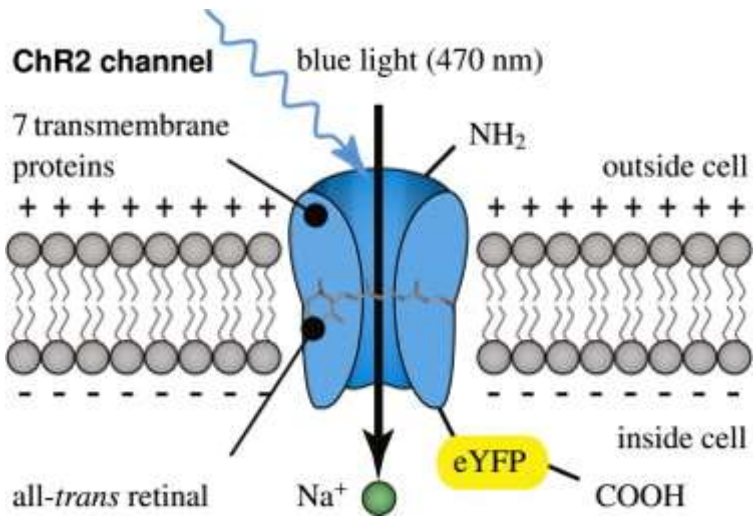


Figure 1. 2 Structure of ChR2 by ref. [28].

Chapter 2. Enhanced the Electrochemical Properties of PEDOT:PSS Electrode by Ethanol for Neural Electrode Interface

2.1 Introduction

Bioelectronic interfaces, which use a variety of conductive materials to electrically interface with organs and tissues, are being used to record or stimulate various bioelectrical signals. At present, most neural electrodes are mainly made of fairly stable metals such as platinum, gold, iridium, titanium, and stainless steel. These exposed metal electrodes often have poor long-term stimulation and recording performance due to poor contact with tissue or scar formation. One of the most commonly used neural stimulators, Iridium oxide [12, 18] has very low impedance and high charge injection capacity, however, it has poor adhesion and can decompose upon stimulation [7].

Poly(3,4-ethylenedioxythiophene):polystyrene sulfonate (PEDOT:PSS) as a neural electrode material has a low impedance and a high charge injection capacity. In general, PEDOT:PSS uses dimethyl sulfoxide (DMSO) and ethylene glycol (EG) as co-solvents to modify

the form and structure. By mixing polar solvents such as DMSO and EG, PEDOT has high conductivity due to the change of benzoid structure to quinoid structure [42-45]. It also converts the coiled-shape of PEDOT: PSS into a linear structure thereby has high conductivity.

PEDOT: PSS as a neural electrode has been continuously studied for low impedance and high charge storage capacity (CSC) or charge injection capacity (CIC) value. Reduction of impedance has the advantage of low power consumption in neural stimulation systems. The mixing of materials such as PEDOT: PSS and CNT [14-16, 23] or graphene [46, 47] has been applied to the study of increasing charge storage capacity or lowering impedance. The use of conductive alginate on PEDOT: PSS has a similar impedance compared to PEDOT: PSS, but has a high CSC value [48].

In this chapter, we evaluated the properties of PEDOT:PSS as a neural electrode by adding ethanol. Co-solvents of ethanol and water have increased interaction and specificity at certain mixing ratios [49, 50]. As a result, the use of co-solvents may increase efficiency at certain ratios, such as cellulose hydrolysis [51]. In the case of post-treatment of PEDOT: PSS, the conductivity increased at 80% of the ethanol mixing ratio [52]. Excess ethanol solvent doping lowers the thickness of PEDOT: PSS,

which can lead to a decrease in impedance. Also, PEDOT: PSS coating solution is water-based shows a high surface tension value, but by adding the excess ethanol the surface tension can be lowered. High surface tension results in poor coating uniformity during repetitive coating. However, low surface tension lets uniform coating quality. PEDOT:PSS coating solution with reduced surface tension allows by ethanol for repeated coatings. The electrical conductivity of PEDOT:PSS film was calculated by measuring sheet resistance and thickness. A chemical and structural information of ethanol mixed PEDOT: PSS film was measured using Fourier-transform infrared spectroscopy (FTIR) and Raman spectroscopy. To use for neural stimulation electrodes: the impedance and CSC measurements of the electrodes are important for the performance evaluation of the electrodes. Impedance and cyclic voltammetry (CV) were measured with a three-electrode system and the CSC was calculated by the measured CV. The impedance and CSC values of PEDOT:PSS were also measured according to the number of coatings with PEDOT: PSS coating solution mixed with ethanol. Mammalian cells expressing a genetically-encoded fluorescent voltage indicator (Bongwoori-R3) was used to evaluate the feasibility of PEDOT: PSS electrodes.

2.2 Materials and methods

2.2.1 Sample preparation

PEDOT:PSS used in the experiment is Clevios™ PH1000 (Heraeus Celvios), which is characterized by high conductivity. The solid content of PH1000 is about 1.0-1.3% and the weight ratio of PEDOT and PSS is 1: 2.5. In order to evaluate the properties of the PEDOT: PSS film by ethanol, a coating solution was prepared by mixing PEDOT: PSS solution and ethanol from 0 wt % to 60 wt % in 10 wt % intervals. PEDOT:PSS coating solution was stirred at room temperature for 30 minutes. The glass substrates with 2.5 cm × 2.5 cm of size were surface treated by Oxygen plasma after washing and spin-coated with a PEDOT: PSS solution mixed with ethanol. Spin coating conditions were coated at 300 rpm for 5 seconds and then at 3000 rpm for 30 seconds. PEDOT:PSS coated on glass was annealed on a hotplate for 30 minutes at 120 °C after coating immediately. Post-treatment was performed in DMSO for 30 minutes after annealing to easily measure conductivity. It was then annealed on a hotplate for 30 minutes at 120 °C again. In the repeated coating experiment, PEDOT: PSS was spin-coated on a glass substrate, and then annealed at 120 °C for 15 minutes, and then PEDOT: PSS was spin-coated again on a PEDOT: PSS-coated glass substrate. After

annealing at 15-minute intervals, the coating was carried out again. In the final step, the annealing was performed at 120 °C for 30 minutes. Likewise, post-treatment was performed in DMSO for 30 minutes after annealing and then annealed on a hot plate for 30 minutes at 120 °C.

2.2.2 Electrical characterization

Conductivity was calculated by sheet resistance and thickness measurement. Sheet resistance was measured using the four-point probe (DASOL ENG, FPP=40K) after the coating and annealing of the PEDOT:PSS. The electrical conductivity was calculated using the measured thickness using stylus profiler and sheet resistance.

$$\rho = R_s \times d$$

$$\sigma = \frac{1}{\rho}$$

Where ρ , R_s , d and σ are the resistivity, the sheet resistance, the thickness of PEDOT:PSS film and electrical conductivity respectively.

2.2.3 Characterization of PEDOT:PSS

The functional group analysis of PEDOT:PSS was performed by Fourier transformed infrared spectroscopy (FTIR) (Bruker, Alpha) in the range from 400 cm^{-1} to 4000 cm^{-1} . The chemical and structural

information of the PEDOT:PSS film measured by Raman spectroscopy (Thermo scientific, DXR2xi). Raman spectroscopy can usually measure symmetric vibrations in the vibration mode of a molecule with good sensitivity. FTIR, on the other hand, measures to identify functional groups of molecules. X-ray photoelectron spectroscopy(XPS) (ThermoFisher Scientific, FC-XP10) was analyzed in the S2p, (b) C(1s), and (c) C(1s) level.

2.2.4 Micro pattern of PEDOT:PSS

There are various methods to pattern the PEDOT:PSS such as direct laser method [53-55], lift-off [56, 57], ink-jet printing [58, 59], screen printing [60-62] and patterning using hydrofluoroethers (HFEs) solvents and fluorinated photoresist [60, 63, 64]. The easiest way is to use a pattern by patterning photoresist on top of the PEDOT:PSS film and then dry etching. However, when PEDOT: PSS is exposed to the developer, its conductivity becomes worse. Of course, the PEDOT:PSS exposed by 300 MIF developer is be removed through dry etching, but during the process of removing the photoresist, the photoresist is not completely removed from the PEDOT:PSS or the PEDOT:PSS is removed with photoresist. The use of an adhesion promoter such as

Hexamethylsilazane (HMDS) is used to improve the adhesion of the PEDOT:PSS and photoresist. But the use of HMDS makes the conductivity of the PEDOT:PSS bad. The use of HMDS may not be necessary for large patterns, but for micropatterns it will be necessary to improve the adhesion of the PEDOT:PSS and photoresist.

The pattern of the PEDOT:PSS using shadow masks can solve the problem of using photoresist, but micro patterns are difficult and have limitations on pattern shapes.

The coating of silver on the top of the PEDOT:PSS can solve the problem by using photoresist. A silver-coated on the top of the PEDOT:PSS protects it from exposure to the developer and HMDS. Also, photoresist remains when it is removed, or the PEDOT:PSS is not removed with photoresist.

To evaluate the electrochemical characteristics, Ti / Au was first deposited on the glass substrate using an E-beam evaporator (ULTECH) and patterned in a lift-off method. PEDOT:PSS solution mixed with ethanol was spin-coated on a glass substrate with a Ti / Au pattern. Subsequently, silver was deposited 50 nm to protect the PEDOT:PSS using an E-beam evaporator. In order to pattern silver on PEDOT:PSS, HMDS was first coated and then AZ4330 photoresist was patterned

using the photolithography method. Exposed silver was wet-etched using silver etchant. Silver etchant consists of nitric acid (65%), phosphoric acid (85%), acetic acid (99.5%) and DI water in a 1:16:16:2 volume ratio. The exposed PEDOT:PSS by silver etching was removed using oxygen RIE dry etching using O₂ gas (20 sccm) at 100 W power. Then, the photoresist was removed sequentially using acetone and silver was removed by using silver etchant. In order to protect the PEDOT:PSS against electrolyte when measuring the electrochemical properties, SU 8 2005 was patterned. Figure 2.1 show the fabrication process flow of PEDOT:PSS electrode.

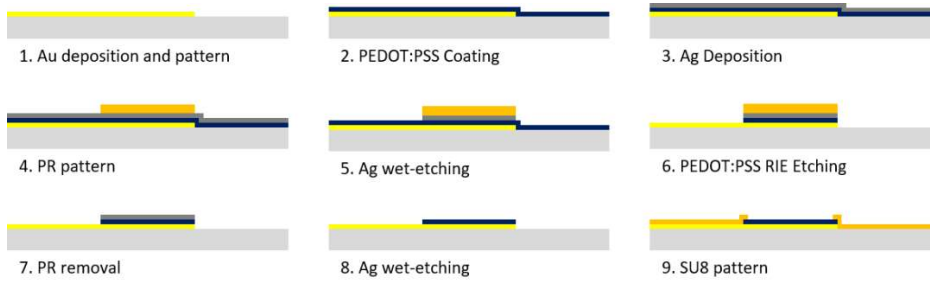


Figure 2. 1 Fabrication process flow of PEDOT:PSS electrode

2.2.5 Electrochemical analysis

To evaluate the electrochemical properties of PEDOT:PSS, electrochemical impedance spectrometry (EIS) was performed. A three-cell electrochemical system was used with impedance analyzers (1786 and 1287A, Solartron Analytical from Farnborough, UK), and Ag / AgCl reference electrodes and platinum counter electrodes. The electrolytes used phosphate-buffered saline (PBS) solutions that were made by dissolving one PBS tablet (Sigma) in 200 ml of deionized water. A cyclic voltammetry (CV) curve was obtained to calculate the charge storage capacity (CSC) using the Potencio Start (1287A, Solartron Analytical, Farnborough, UK) and a three-cell electrochemical system. In order to obtain CV, the electrochemical potential of the electrode was measured and plotted during sweep between -0.6 V and 0.8 V for the Ag/AgCl reference electrode at a sweep speed of 50 mV/s. The CSC for cathodic and anodic value was calculated by integrating the negative area and the positive area of cyclic voltammetry.

2.2.6 Cell culture and transfection

Human Embryonic Kidney 293 (HEK 293) cells were cultured by using an incubator that was kept at 5% CO₂ level and 37 °C in Dulbecco's Modified Eagle Medium (DMEM; Gibco, USA)

supplemented with 10 % v/v Fetal Bovine Serum (Gibco, USA). On the day of transient transfection, the HEK 293 cells were first dissociated and seeded onto a poly-D-lysine (Sigma-Aldrich, USA) coated coverslip at high density to ensure efficient stimulation by the thin film electrode (to be modified). Transfection of the HEK 293 cells was conducted with a lipofection reagent (Lipofectamine 2000; Thermo Fisher Scientific, USA). One microliter of the reagent was mixed with 200 ng of a genetically-encoded voltage indicator (pcDNA3.1(+)-Bongwoori-R3) [65] plasmid DNA incubated in serum-free DMEM at room temperature for 30 min. The transfection mixture was then gently added to the seeded cells and incubated for about 40 hours in the CO₂ incubator.

2.2.7 Stimulation and imaging

The thin-film electrode was attached to the bottom of a patch-clamp chamber (RC-26G, Warner Instruments, USA) via a high vacuum grease (Dow Corning, USA). Then the chamber was filled with normal patch-clamp bath solution containing 150 mM NaCl, 4 mM KCl, 1 mM MgCl₂, 2 mM CaCl₂, 5 mM D-glucose and 5 mM HEPES (pH = 7.4). The coverslip with the transfected HEK 293 cells was placed onto the thin film electrode with the side of the cells facing the electrodes directly.

For simultaneous electrical stimulation and optical imaging of the

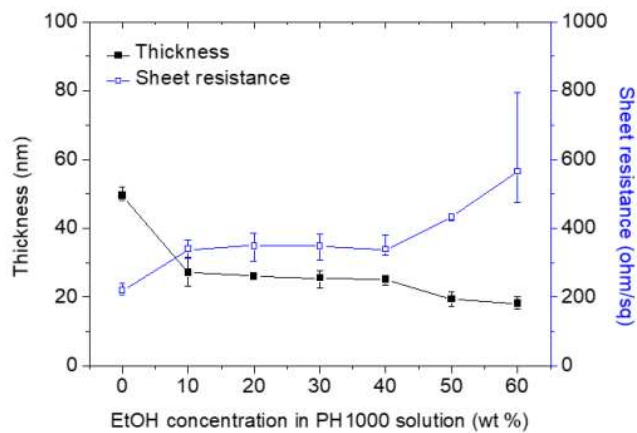
transfected HEK 293 cells, an upright fluorescence microscope system (Slicescope, Scientifica, UK) that is equipped with a 460 nm LED (UHP-Mic-LED-460, Prizmatix, Israel), a GFP filter set (GFP-3035D-OMF, Semrock, USA) and the DaVinci-2K low noise CMOS camera system (SciMeasure analytical systems, USA) was used. The optical images for HEK 293 cells were acquired at 100 Hz frame rate unless otherwise noted.

To inject current pulses onto the sample, an isolated current stimulator (DS3; Digitimer, UK) was connected to the thin film electrode. A patch-clamp amplifier (Multiclamp 700B) together with a digitizer (Digidata 1550B; both by Molecular devices, USA) controlled the stimulus waveform and sent a signal to the current stimulator to initiate each stimulation step.

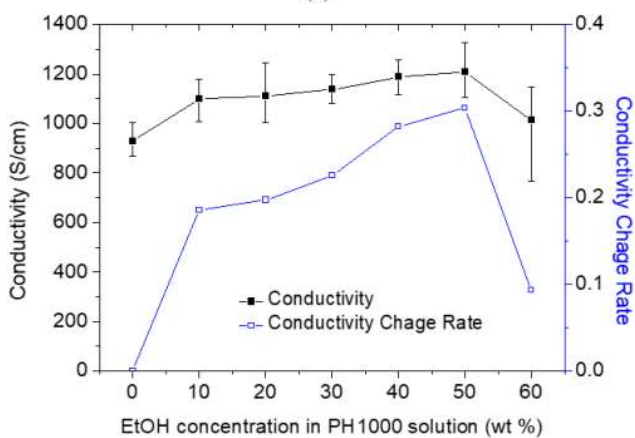
2.3 Results

2.3.1 Electrical characteristics

Sheet resistance was not measured with 4-probe measurement equipment used prior to post-treatment of DMSO, regardless of the ethanol mixture. Figure 2.2 shows the thickness, surface resistance and conductivity of conductivity measurement after post-treatment of DMSO according to the ethanol concentration ratio. The conductivity value of the PEDOT:PSS film without ethanol was measured at about 900 S/cm. The higher the ethanol content, the higher the measured conductivity was, and the ratio of ethanol to 50 wt % was measured at about 1200 S/cm. This value is about 30% higher than the conductivity of PEDOT:PSS film without ethanol. However, if the ratio of ethanol mixed with 60 wt %, the conductivity of the PEDOT:PSS film was reduced and the value was measured at about 950 S/cm.



(a)



(b)

Figure 2. 2 (a) Thickness, surface resistance and (b) conductivity of the PEDOT:PSS film according to ethanol concentration ratio.

2.3.2 FTIR analysis

FTIR measurements were made to view information on the chemical bonding and molecular structures of the PEDOT:PSS [66-68]. Figure 2.3 and figure 2.4 show the FTIR spectra from 400 cm^{-1} to 3000 cm^{-1} of PEDOT:PSS depending on the ethanol concentration ratio before post-treatment of DMSO. 1541 cm^{-1} and 1203 cm^{-1} peak are related to the definition of phenyl rings attached to the sulfonate groups of PSS. -SO_3 symmetric stretching vibrations are shown in 1038 cm^{-1} and 1010 cm^{-1} . In addition, the peaks of 1268 cm^{-1} , 1180 cm^{-1} and 1101 cm^{-1} are for the vibrations of thiophene, ethylenedioxy and the C–O–C groups in the PEDOT. As the ethanol mixing ratio increased, the change in 2360 cm^{-1} peak was observed. The 2360 cm^{-1} peak is associated with O–H stretch of carboxylic acids [69, 70]. When ethanol is oxidized, two hydrogens were removed to become ethanal and ethanal gets oxygen to acetic acid as shown in figure 2.5 [71]. O–H stretch of acetic acid resulted in 2360 cm^{-1} peaks and the strongest strength at the ethanol mixing ratio of 50 wt%. The 2360 cm^{-1} peak of which the ethanol concentration ratio increased to 50 wt% decreased from 60 wt% of the ethanol concentration ratio. The change of FTIR peak with ethanol concentration ratio was also shown at 2960 cm^{-1} peak that resulted from asymmetric CH_3 [72, 73].

Like the 2360 cm^{-1} peak, the intensity of 2960 cm^{-1} peak was high at 50 wt% of ethanol concentration ratio. The peak change with the ethanol concentration ratio was also shown at 1542 cm^{-1} and 1560 cm^{-1} peaks. 1542 cm^{-1} and 1560 cm^{-1} peak are related to the deformation of phenyl rings with attached sulfonate groups and aromatic ring deformation vibrations [74]. In the case of PEDOT: PSS without ethanol mixing, the 1542 cm^{-1} peak had a higher intensity than 1560 cm^{-1} , but the inversion occurred as the ethanol mixing ratio increased. The intensity reversal of the two peaks was greatest at 50 wt % of ethanol and decreased again at 60 wt % of ethanol. The intensity of the 1560 cm^{-1} peak is highly dependent on the substituents attached to the ring, which means that the PSS substituents are changed by ethanol.

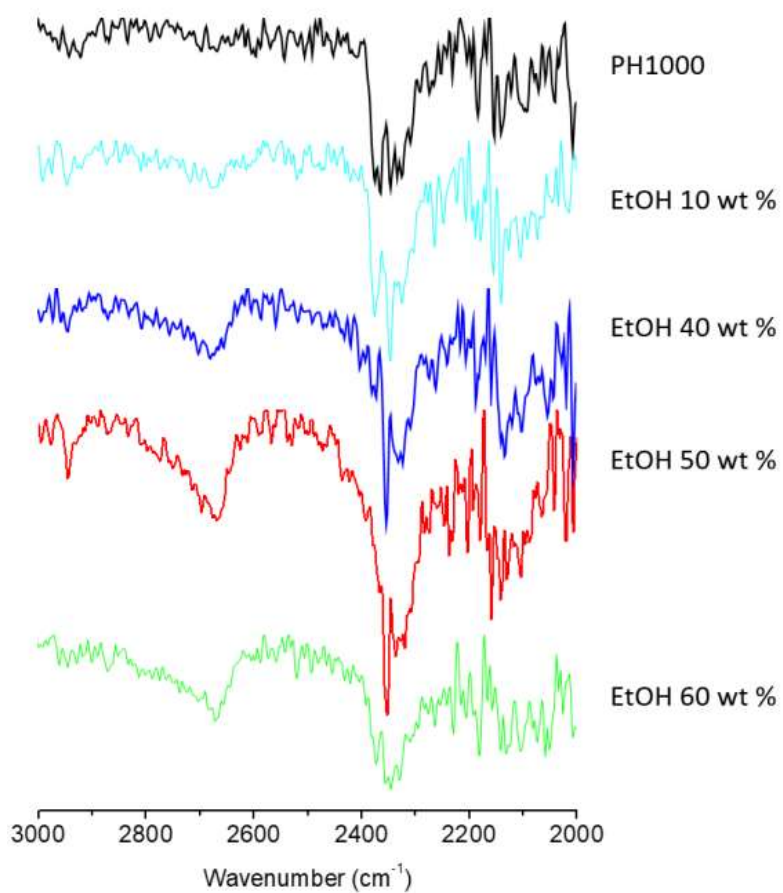


Figure 2. 3 FTIR spectra from 2000 cm⁻¹ to 3000 cm⁻¹ of PEDOT:PSS depending on ethanol concentration ratio.

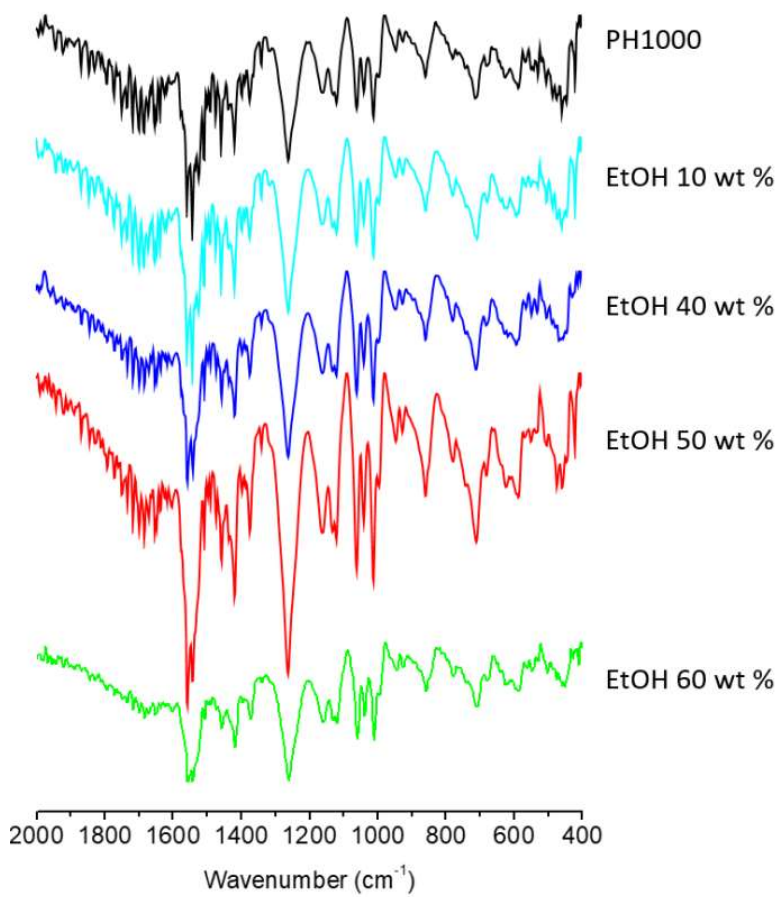


Figure 2. 4 FTIR spectra from 400 cm⁻¹ to 2000 cm⁻¹ of PEDOT:PSS depending on ethanol concentration ratio.

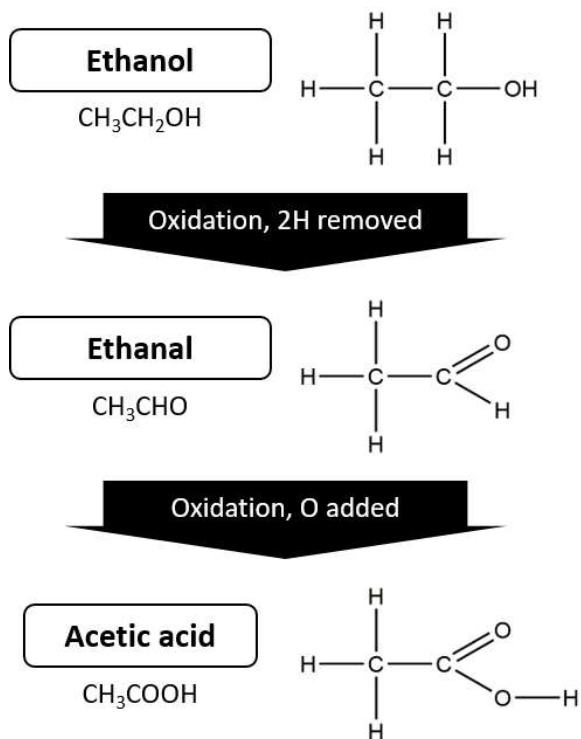


Figure 2. 5 Oxidation of ethanol.

2.3.3 XPS analysis

The figure 2.6 (a-c) show XPS data in the S (2p), C (1s) and O (1s) positions of PEDOT: PSS with 50 wt % of ethanol and pristine PEDOT: PSS. The C (1s) peak did not show any difference regardless of ethanol mixing. In the S (2p) pick, the shift occurred with lower energy from 168.2eV pick to 168 eV. 169 eV is related to the sulfur atoms of PSS. Shifting to a lower energy of PSS pick means PSS-H becomes PSS-. Changes in PSS-H to PSS-H also appear in O (1s) picks. 532 eV pick is associated with oxygen atoms in the sulfonic acid groups of PSS-H. The O (1s) pick after ethanol mixing weakened the energy bond from 532.2 eV to 521.9 eV, indicating a change from PSS-H to PSS- [75]. Increasing the PSS- may increase the doping of the PEDOT. The ionization of PSS is related to pH change by ethanol mixing. Figure 2.7 shows the pH concentration of the PH1000 solution according to the ethanol mixing ratio. Ionization occurs better with increasing pH value. Increased pH value by ethanol causes PSS-H to change more to PSS-. Increasing the pH value may also promote the ionization of acetic acid produced by the oxidation of ethanol, which may also be a dopant for PEDOT [76].

The acid dissociation constant (pKa) constant of acetic acid produced by ethanol oxidation is 4.8. The ionization of acetic acid is affected by

the pH concentration of the solvent [77, 78]. Higher pH values result in better ionization of acetic acid and increased doping of PEDOT. The acetic acid produced by ethanol oxidation not only acts as a dopant for PEDOT, it also decreases the Coulomb interaction between the charge carriers carried on the PEDOT chain and the PSS counter ion by the screening effect [79-81], leading to an increase in conductivity as shown in figure 2.8. The presence of acetic acid also showed differences in the atomic contents of S (2p), C (1s) and O (1s) after adding ethanol. The content of S (2p), C (1s), O (1s) was 9.53 %, 66 %, 24.47 % for pristine PH1000, and 9.42 %, 68.43 %, and 22.14 % for PEDOT: PSS with 50 wt % ethanol due to the increase in C (1s) by acetic acid as shown in figure 2.6 (d).

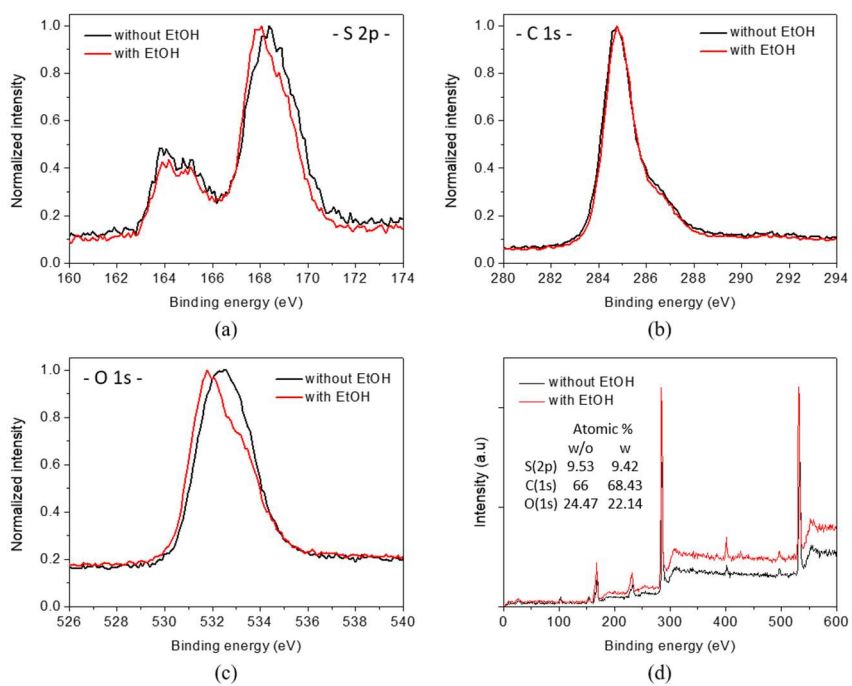


Figure 2. 6 XPS spectra of (a) S (2p), (b) C (1s), and (c) O (1s) and (d) XPS survey level S (2p), C (1s), and O (1s) spectra of pristine PH1000 and PEDOT:PSS with ethanol.

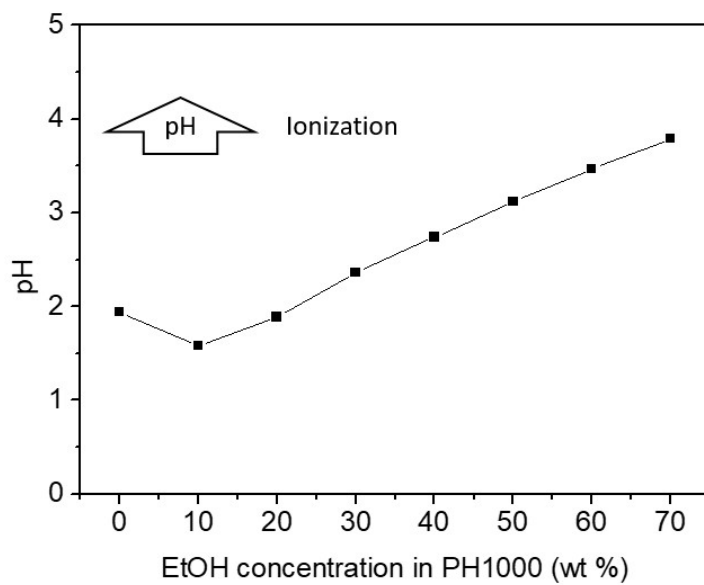


Figure 2. 7 The pH concentration according to the ethanol mixing ratio in the PH1000 solution.

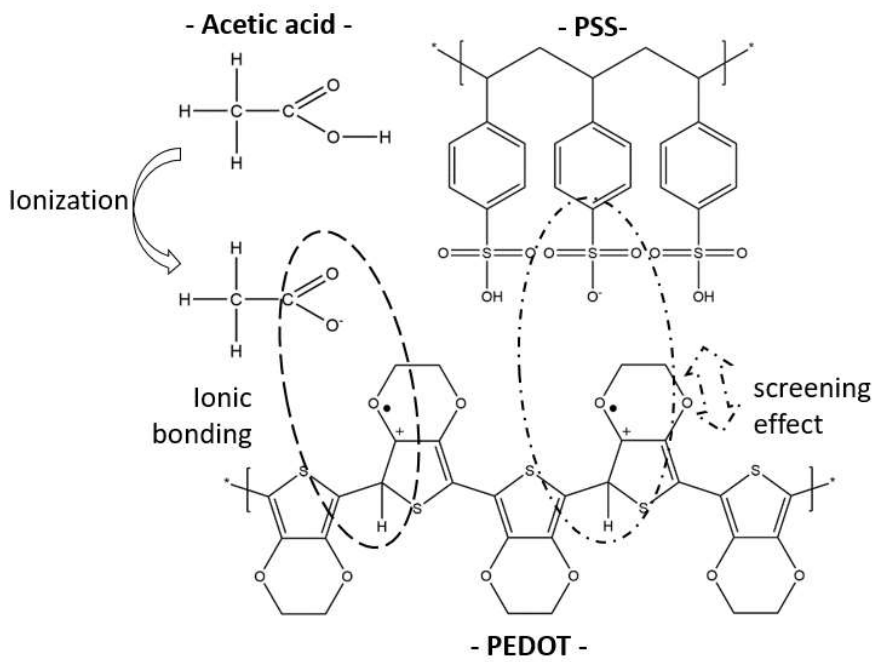


Figure 2. 8 Schematic of ethanol solvent doping.

2.3.4 Raman spectrum analysis

Raman spectrums were made to view information on the chemical and structural information of the PEDOT:PSS film [82-85]. The main Raman peaks of PEDOT are found at 1436 cm^{-1} , 1361 cm^{-1} and 1252 cm^{-1} assigned to the $C_{\alpha} = C_{\beta}$ asymmetrical, $C_{\beta} - C_{\beta}$ stretching and $C_{\alpha} - C_{\alpha'}$ interring stretching vibration, respectively. 1537 cm^{-1} and 1570 cm^{-1} are related to $C_{\alpha} = C_{\beta}$ asymmetrical stretching thiophene rings at the middle and the end of PEDOT chains, respectively. The main peaks of the PSS appear at 1110 cm^{-1} and 1000 cm^{-1} . Figure 2.9 shows the normalized intensity of PEDOT: PSS with and without ethanol before post-treatment of DMSO normalized to the 1436 cm^{-1} Raman peak.

Regardless of whether ethanol was mixed or not, benzoid-to-quinoid shift of PEDOT:PSS was observed at near 1436 cm^{-1} . In addition, the peak change of PSS was not observed, but the intensity of 1361 cm^{-1} , 1537 cm^{-1} , and 1570 cm^{-1} assigned to $C_{\beta} - C_{\beta}$ stretching and $C_{\alpha} = C_{\beta}$ asymmetrical stretching was decreased in the case of PEDOT: PSS mixed with ethanol. Also, the 700 cm^{-1} peak is related to C-S ring deformation of PEDOT and its intensity decreases after ethanol mixing [86, 87]. This decrease in peaks associated with PEDOT occurs after solvent doping with a solvent such as DMSO, EG or methanol. For

ethanol, however, structural changes of quinoids in benzoid, such as DMSO and EG, could not be confirmed by the Raman spectrum [42-45]. The increased doping of PEDOT can be inferred from the decrease of PEDOT associated peaks.

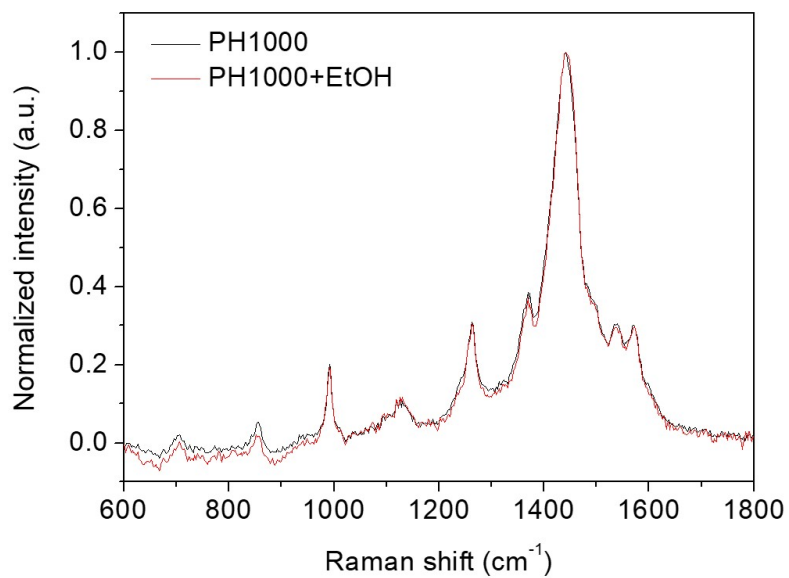


Figure 2. 9 Raman spectra of PEDOT:PSS thin films with and without ethanol.

2.3.5 Impedance & CSC measurement

In order to measure electrochemical properties of PEDOT:PSS film, exposed patterns of the PEDOT:PSS with 40 μm of diameter was made shown in figure 2.10. The figure 2.11 shows the impedance and the electrochemical impedance spectroscopy (EIS) from frequency 10^0 Hz to 10^5 Hz according to the number of coatings under the conditions of 50 wt % ratio of ethanol and pristine PH1000 without ethanol after post-treatment of DMSO. The area of the PEDOT:PSS film for measuring the impedance is about $1,200 \mu\text{m}^2$ and PEDOT:PSS film was coated and patterned on gold. In the case of PEDOT:PSS film with ethanol, it had a lower impedance in all frequency range than pristine PH1000. In particular, the impedance of the pristine PH1000 was 10 times higher than PEDOT:PSS with ethanol at 1kHz of frequency. In the case of PEDOT:PSS film with ethanol, the coating number was increased, resulting in an unusual change in impedance. In the low-frequency region below 10 Hz, the impedance of PEDOT:PSS was maintained regardless of the number of coatings. However, as the number of coatings increased, the impedance of PEDOT:PSS increased at higher frequencies. In particular, when the number of coating is three times, the impedance increased slightly above pristine PH1000 in some frequency ranges. The

difference in the number of coatings is also evident in the EIS. The equivalent circuit of the Randles model [8] consists of double-layer capacitance, electron transfer resistance, and uncompensated (or electrolyte) resistance. In the high-frequency region, the effect of uncompensated (or electrolyte) resistance is large but the lower the frequency, the higher the electron transfer resistance. As the number of coatings increased, the electron transfer resistance increased, which is shown by increasing the thickness of PEDOT: PSS.

Figure 2.12 (a) shows the plotted CV image during sweep between -0.6 V and 0.8 V at 50 mV/s of sweep speed. Figure 2.12 (b) shows the thickness of PEDOT:PSS film and CSC calculated using the CV data obtained. The CSC value of PEDOT: PSS mixed with 50 wt% of ethanol was shown to be higher than pristine PH1000. Despite the lower thickness of PEDOT:PSS film with ethanol than pristine PH1000, having a higher CSC value means more doping of PEDOT by ethanol. The improvement in doping is also seen in EIS as shown in figure 2.11 (b), the thickness of PEDOT:PSS with ethanol under the two coating conditions was thicker than the thickness of the pristine PH1000, but with lower electron transfer resistance. As the number of coatings increased, the thickness and CSC value of PEDOT:PSS film with ethanol

increased, and the CSC value of three coatings was about 30 mC/cm², which was about three times higher than that of one coating and about 15 times than that of pristine PH1000.

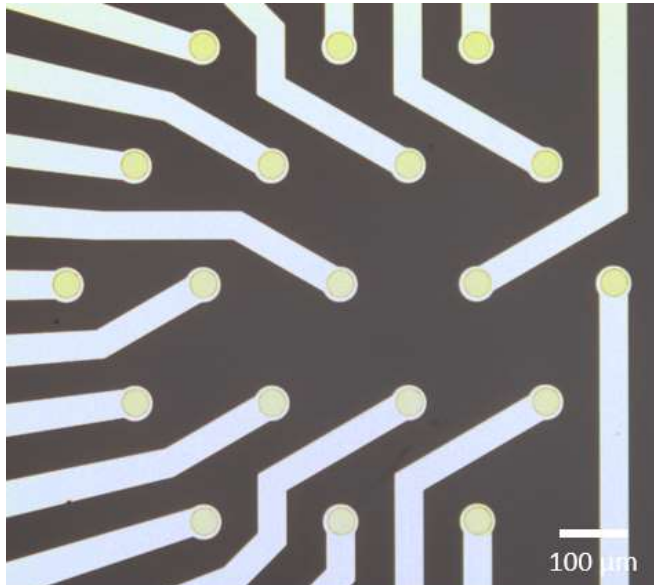
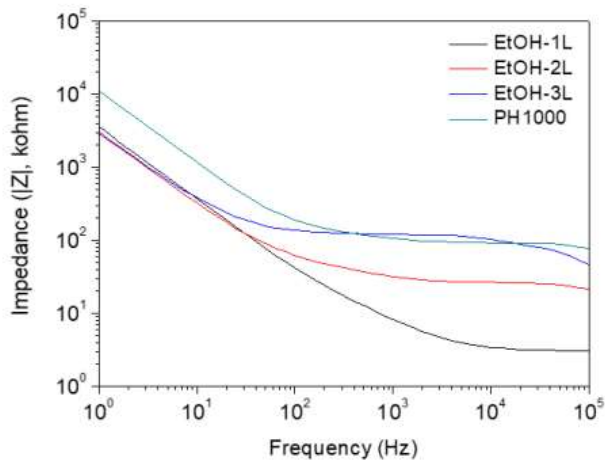
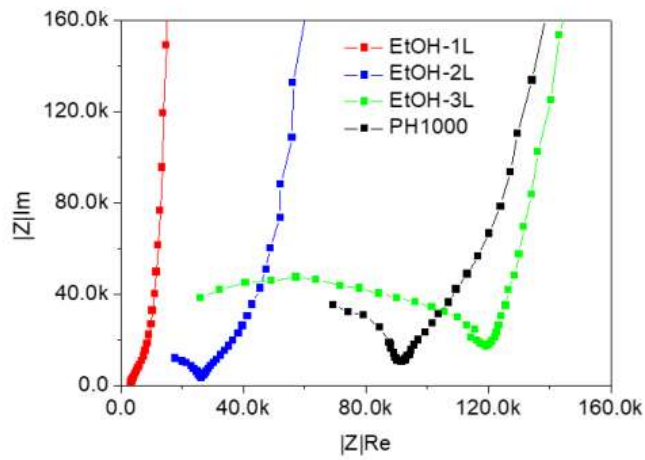


Figure 2. 10 PEDOT:PSS electrode with a diameter 40 μm.



(a)



(b)

Figure 2. 11 (a) Impedance from frequency 10^0 Hz to 10^5 Hz and (b) the electrochemical impedance spectroscopy according to the number of coatings under the conditions of 50 wt % ratio of ethanol and pristine PH1000 without ethanol after post-treatment of DMSO.

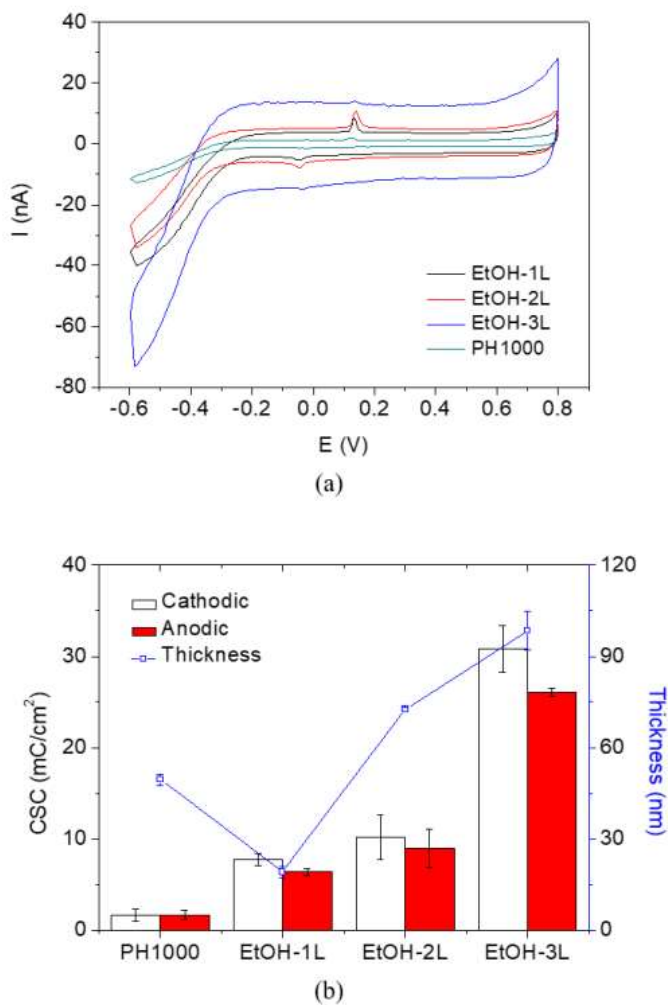
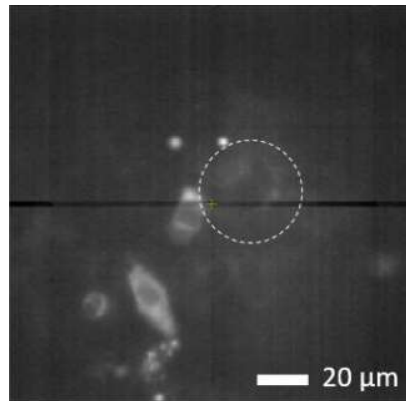


Figure 2. 12 (a) Plotted CV graph and (b) thickness and CSC of PEDOT:PSS according to the number of coatings under the conditions of 50 wt % ratio of ethanol and pristine PH1000 without ethanol after post-treatment of DMSO.

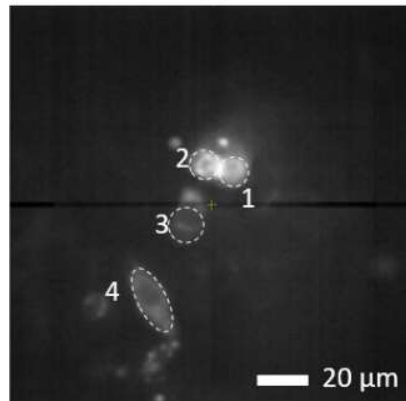
2.3.6 Fluorescent voltage imaging of cultured mammalian cells stimulated by the PEDOT:PSS electrode

In order to evaluate PEDOT:PSS-EtOH electrode with a diameter of 40 μm , a voltage-dependent fluorescence image was used using genetically-encoded voltage indicators (Bongwoori-R3). Figure 2.13 shows the fluorescent voltage imaging of cultured mammalian cells stimulated by the PEDOT:PSS electrode. The position of the electrode is shown in the dotted circle in figure 2.13 (a) and the current waveform used for the experiment is shown in the inset in figure 2.14 (a). Stimulation of cathodic pulses causes the HEK 293 cell to become hyperpolarization, resulting in fluorescence imaging of the fluorescent voltage indicator. Figure 2.14 (a-d) show the voltage-dependent fluorescence changes with varying current amplitudes from cells depicted in figure 2.13 (b). The Bongwoori-R3 expressed cells located in areas 1 and 2 close to the electrode showed high fluorescence changes, but as the distance between the electrode and the cell increased, the change in fluorescence was less and less visible as shown figure 2.14 (c, d). In addition, as the current intensity increased, the change in fluorescence was large, and the change was observed in cells located in areas 1,2,3. At a stimulus duration of 10 ms, the minimum stimulus

current of HEK 293 cell was above about 3 μA and the charge density was about 2.39 mC/cm^2 .



(a)



(b)

Figure 2. 13 An epifluorescence image showing HEK 293 cells expressing a fluorescent voltage indicator (Bongwoori-R3) (a) before and (b) after electrical stimulation to current of 10 μ A. The dotted circle in (a) indicates the PEDOT:PSS electrode. Each dotted circle in (b) represents a HEK 293 cell.

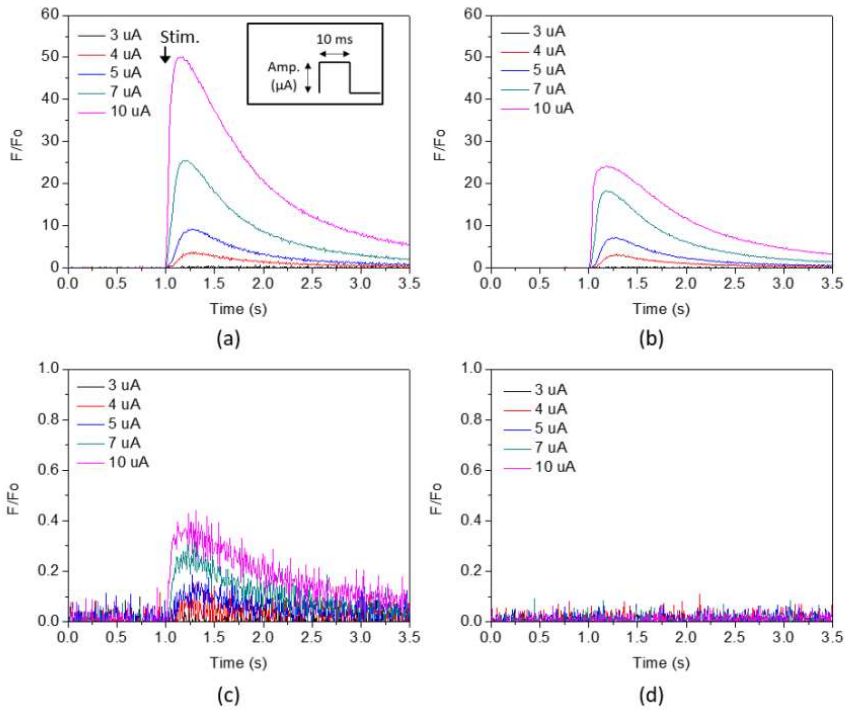


Figure 2. 14 Voltage-dependent fluorescence changes with varying current amplitudes from cells depicted in figure 2.13 (b).

Inset in (c) shows the current input waveform used for the experiment. $\Delta F/F_0$ represents fractional fluorescence change of the traces (ΔF value) divided by the average of 10 prestimulus frames (F_0 value).

2.4 Discussion

In this chapter, the electrical and electrochemical properties of PEDOT:PSS by ethanol were improved. In the case of PEDOT: PSS film with ethanol, the electrical conductivity was increased by about 30% compared with pristine PH1000 after post-treatment of DMSO. The change of quinoid structure from benzoid structure known as the effect of solvent doping was not observed by ethanol solvent doping. However, the mixing of ethanol increased the pH value of PEDOT: PSS solution, which promoted the ionization of PSS. In addition, acetic acid produced by the oxidation of ethanol was also ionized by increasing the pH value, acting as a dopant of PEDOT. As a result, the impedance of PEDOT:PSS mixed with ethanol was lower in all frequency ranges compared to pristine PH1000. In particular, the impedance of PEDOT:PSS with ethanol was 100 times lower than without ethanol at 1 kHz. Excess ethanol mixing lowers the surface tension value of the PEDOT: PSS coating solution, which leads to good coating uniformity. According to the number of PEDOT: PSS coatings mixed with ethanol, the impedance had a similar impedance in the low-frequency region, but the impedance increased at the high frequency as the number of coatings increases due to increasing of electron transfer resistance by increasing of thickness.

Increasing doping by ethanol resulted in an increase in CSC values as well as a decrease in impedance. The CSC value of PEDOT:PSS mixed with ethanol had a higher value than without ethanol. Although the thickness of PEDOT:PSS with ethanol is lower than without ethanol, having a higher CSC value means increased doping of the PEDOT by ethanol. As the number of coatings of PEDOT:PSS with ethanol increased, the CSC value also increased. In particular, CSC values of PEDOT:PSS with ethanol coated 3 times approximately 10 times higher than pristine PH1000. Low impedance and high CSC have great advantages as a neural electrode interface. Excess mixing of ethanol allowed PEDOT: PSS to have lower impedance and higher CSC values, which could be used as a useful electrode material as a neural electrode interface. The feasibility as neural electrode was evaluated using mammalian cell. HEK-293 cells expressing a genetically-encoded fluorescent voltage indicator were stimulated using PEDOT:PSS-Ethanol electrode with diameter of 40 μm at a current of 2 μA . When the current was increased to 10 μA , the change in fluorescence of Bongwoori-R3 expressed cells also shown to increase. This shows that the stimulus is sufficiently generated by the PEDOT: PSS electrode.

Chapter 3. Enhanced the Stability and Electrochemical Properties of PEDOT:PSS-GOPS Electrode by Ethanol for Neural Electrode Interface

3.1 Introduction

In the field of bioelectronics, traditional metal electrodes record electrophysiological signals or stimulate organs and tissues. Research on implant electrodes such as cochlear implants [1-3] and DBS [88, 89] that require long-term stability, is ongoing. At present, most neural electrodes are mainly made of fairly stable metals such as platinum [90-92], gold [93], iridium, titanium [94] and stainless steel [22]. Iridium oxide [18, 21] also has very low impedance and high charge injection capacity but has poor adhesion.

More recently, the use of Poly(3,4-ethylenedioxythiophene):poly(styrenesulfonate) (PEDOT: PSS), a conductive polymer, is widely used to design biodevices as biocompatible materials [13-16, 19, 23]. To develop the material, PEDOT is doped with PSS, which is easily dispersed in aqueous solution and has excellent conductivity and

chemical stability. In particular, the low impedance and high charge injection capacity values of PEDOT:PSS have proven to be advantageous in the development of electrodes for neural stimulation. However, PEDOT:PSS has a very poor film peel and performance when exposed in an aqueous environment. Crosslinking is necessary to ensure the stability of PEDOT:PSS and to prevent film peeling and dispersion in an aqueous environment. To enhance the stability of PEDOT: PSS, cross-linking agents such as (3-glycidyloxypropyl) trimethoxysilane (GOPS) and divinyl sulfone (DVS) are mixed [95-98].

Among them, GOPS is a crosslinking agent most commonly used, with the methoxy silane groups of GOPS crosslink with the sulfonate groups of PSS. The combination of GOPS and substrate also protects PEDOT: PSS from peeling foil. However, due to the combination of PSS and GOPS, the dopant of PEDOT, the electrical conductivity decreases with increasing GOPS. That is, the addition of GOPS is a trade-off between water stability or mechanical stability and conductivity.

In this chapter, the stability and electrochemical properties of PEDOT: PSS-GOPS film by ethanol are evaluated for neural electrode interfaces. Co-solvent of water-ethanol is used to improve efficiency in various fields such as cellulose hydrolysis and cellulose liquefaction [51, 99,

100]. The electrical conductivity of PEDOT: PSS film was calculated by measuring sheet resistance and thickness. Ethanol mixed PEDOT: PSS-GOPS film was measured for chemical and structural information using Fourier-transform infrared spectroscopy (FTIR) and Raman spectrum measurements. Absorbance measurements using UV/vis spectrum were used to determine the conformation of PSS and the formation of freely moving soliton, polaron and bipolaron of PEDOT in PEDOT:PSS-GOPS film. The AFM indentation method was also used to measure the modulus of PEDOT:PSS-GOPS thin film [101, 102]. For neural stimulation electrodes, the impedance and charge storage capacity (CSC) measurements of the electrodes are important for the performance evaluation of the electrodes. Impedance and cyclic voltammetry (CV) of PEDOT:PSS-GOPS film was measured with a three-electrode system and the CSC was calculated by the measured CV. Mammalian cells expressing a genetically-encoded fluorescent voltage indicator (Bongwoori-R3) was used to evaluate the feasibility of PEDOT: PSS electrodes.

3.2 Materials and methods

3.2.1 Sample preparation

Added 1 wt % GOPS for the solution mixed with PEDOT:PSS (Clevios PH-1000 from Heraeus Holding GmbH) and EG (5 wt %). Ethanol was mixed from 10 wt % to 60 wt % for the solution containing PEDOT:PSS, EG, and GOPS. PEDOT:PSS coating solution was stirred at room temperature for 30 minutes. The washed glass substrate (2.5 cm X 2.5 cm) for coating was surface-treatment with 100 W power for 1 min with oxygen plasma. All coating conditions were carried out for 500 rpm 5 s and 3000 rpm 30 s and then annealed on a hot plate for 30 minutes at 120 °C.

3.2.2 Electrical characterization

Conductivity was calculated by sheet resistance and thickness measurement. Sheet resistance was measured using the four-point probe (DASOL ENG, FPP=40K) after the coating and annealing of the PEDOT:PSS. The electrical conductivity was calculated using the measured thickness using stylus profiler and sheet resistance.

$$\rho = R_s \times d$$

$$\sigma = \frac{1}{\rho}$$

Where ρ , R_s , d and σ are the resistivity, the sheet resistance, the thickness of PEDOT:PSS film and electrical conductivity respectively.

3.2.3 Characterization of PEDOT:PSS

The functional group analysis of PEDOT:PSS was performed by Fourier transformed infrared spectroscopy (FTIR) (Bruker, Alpha) in the range from 400 cm^{-1} to 4000 cm^{-1} . The chemical and structural information of the PEDOT:PSS film measured by Raman spectroscopy (Thermo scientific, DXR2xi). Raman spectroscopy can usually measure symmetric vibrations in the vibration mode of a molecule with good sensitivity. FTIR analysis, on the other hand, measures to identify functional groups of molecules. The UV-vis absorbance spectra from 200 nm to 1100 nm of PEDOT:PSS film were obtained UV-vis spectrometer (PerkinElmer, Lambda 35). The surface roughness of PEDOT:PSS film on glass substrate were carried out with an atomic force microscope (AFM) (ParkSystems, NX10). The AFM tip used is CONTSCR from Nanosensors. Topography images of AFM of PEDOT:PSS film were measured in $1 \mu\text{m} \times 1 \mu\text{m}$ size. Contact angle measurements (Surface Electro Optics, Phoenix-150) of PEDOT:PSS film were carried by the

static drop method. For contact angle data, 2 μL droplet of water was deposited onto PEDOT:PSS film on glass substrate. All contact angle data were averaged over at least three measurements on different areas of the sample.

3.2.4 Mechanical properties measurement

In order to measure the mechanical properties of PEDOT: PSS-GOPS film according to the ethanol concentration ratio, Atomic Force Microscopes (Park Systems, NX10) indentation method was used. The AFM tip used is SD-R30-NCH from Nanosensors. In order to measure the modulus of PEDOT: PSS-GOPS film, two models of Derjaguin-Muller-Toporov (DMT) were used [103, 104].

Typical modulus measurement models are the DMT and Johnson-Kendall-Roberts (JKR) [105] models. The biggest difference between the DMT model and JKR model is due to the contact area and applied force. The contact area is zero when the maximum adhesive force and the cantilever restoring force are balanced. This happens when contact begins when the tip approaches the sample. In the JKR model, the contact area is not zero when the applied force and the maximum adhesive force are equal.

The JKR model is valid for soft elastic materials with large tip radii and high surface energy, while the DMT model is applied to rigid solids with small tip radii and low surface energy.

The DMT model is given by

$$\delta = \frac{a^2}{R},$$

$$p = \frac{K}{R} a^3 - 2\pi w R.$$

Where w , a , δ , K , R , and p are adhesive energy, the radius of the contact line, the maximum deformation at the z-axis, the elastic coefficient, radius of the spherical probe and the force.

the JKR model is given by

$$\delta = \frac{a^2}{R} - \left(\frac{8\pi w a}{3K} \right)^{1/2},$$

$$P = \frac{K}{R} a^3 - (6\pi w K a^3)^{1/2}.$$

The elastic coefficient obtained by each model can be obtained by Young's modulus by the following equation.

$$K = \frac{4}{3} \frac{E}{1 - \nu^2}$$

Where E and ν are Young's modulus and Poisson's ratio. Figure 3.1 shows the A schematic diagram of the adhesion of AFM tip with radius, R , for modulus measurement of PEDOT:PSS thin film.

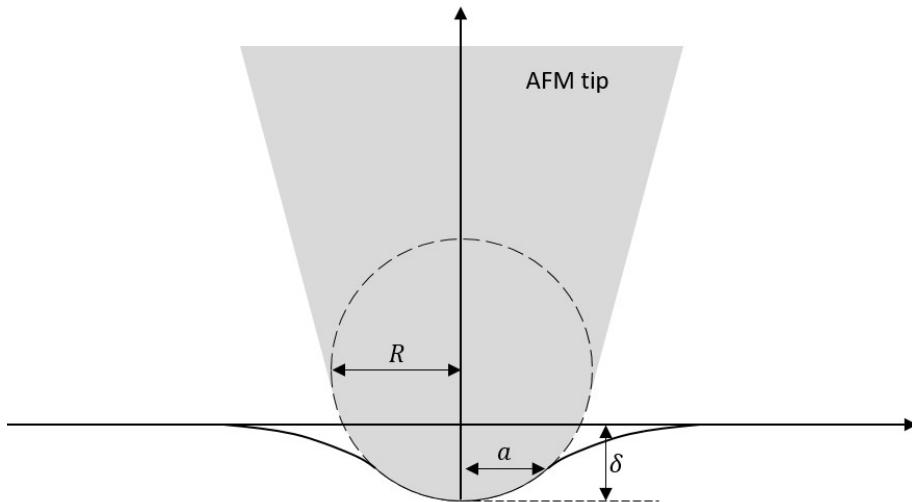


Figure 3. 1 A schematic diagram of adhesion of AFM tip with radius, R , for modulus measurement of PEDOT:PSS thin film.

After contacting thin film and AFM tip, the PEDOT:PSS thin film is deformed by AFM tip. Where a and δ represent the radius of the contact line and the maximum deformation at the z-axis respectively.

3.2.5 Micro pattern of PEDOT:PSS film

To evaluate the electrochemical characteristics, Ti/Au was first deposited on the glass substrate using an E-beam evaporator (ULTECH) and patterned in a lift-off method. PEDOT:PSS solution mixed with ethanol was spin-coated on a glass substrate with a Ti / Au pattern. Subsequently, silver was deposited 50 nm to protect the PEDOT:PSS using an E-beam evaporator. In order to pattern silver on PEDOT:PSS, HMDS was first coated and then AZ4330 photoresist was patterned using the photolithography method. Exposed silver was wet-etched using silver etchant. Silver etchant consists of nitric acid (65%), phosphoric acid (85%), acetic acid (99.5%) and DI water in a 1:16:16:2 volume ratio. The exposed PEDOT:PSS by silver etching was removed using oxygen RIE dry etching using O₂ gas (20 sccm) at 100 W power. Then, the photoresist was removed sequentially using acetone and silver was removed by using a silver etchant. In order to protect the PEDOT:PSS against electrolyte when measuring the electrochemical properties, SU 8 2005 was patterned.

3.2.6 Electrochemical analysis

To evaluate the electrochemical properties of PEDOT:PSS, electrochemical impedance spectrometry (EIS) was performed. A three-cell electrochemical system was used with impedance analyzers (1786 and 1287A, Solartron Analytical from Farnborough, UK), and Ag / AgCl reference electrodes and platinum counter electrodes. The electrolytes used phosphate-buffered saline (PBS) solutions that were made by dissolving one PBS tablet (Sigma) in 200 ml of deionized water. A cyclic voltammetry (CV) curve was obtained to calculate the charge storage capacity (CSC) using the Potencio Start (1287A, Solartron Analytical, Farnborough, UK) and a three-cell electrochemical system. In order to obtain CV, the electrochemical potential of the electrode was measured and fluted during sweep between -0.6 V and 0.8 V for the Ag / AgCl reference electrode at a sweep speed of 50 mV/s. The CSC for cathodic and anodic value was calculated by integrating the negative area and the positive area of cyclic voltammetry.

3.2.7 Cell culture and transfection

Human Embryonic Kidney 293 (HEK 293) cells were cultured by using an incubator that was kept at 5% CO₂ level and 37 °C in

Dulbecco's Modified Eagle Medium (DMEM; Gibco, USA) supplemented with 10 % v/v Fetal Bovine Serum (Gibco, USA). On the day of transient transfection, the HEK 293 cells were first dissociated and seeded onto a poly-D-lysine (Sigma-Aldrich, USA) coated coverslip at high density to ensure efficient stimulation by the thin film electrode (to be modified). Transfection of the HEK 293 cells was conducted with a lipofection reagent (Lipofectamine 2000; Thermo Fisher Scientific, USA). One microliter of the reagent was mixed with 200 ng of a genetically-encoded voltage indicator (pcDNA3.1(+)-Bongwoori-R3) [65] plasmid DNA incubated in serum-free DMEM at room temperature for 30 min. The transfection mixture was then gently added to the seeded cells and incubated for about 40 hours in the CO₂ incubator.

3.2.8 Stimulation and imaging

The thin-film electrode was attached to the bottom of a patch-clamp chamber (RC-26G, Warner Instruments, USA) via a high vacuum grease (Dow Corning, USA). Then the chamber was filled with normal patch-clamp bath solution containing 150 mM NaCl, 4 mM KCl, 1 mM MgCl₂, 2 mM CaCl₂, 5 mM D-glucose and 5 mM HEPES (pH = 7.4). The coverslip with the transfected HEK 293 cells was placed onto the thin

film electrode with the side of the cells facing the electrodes directly.

For simultaneous electrical stimulation and optical imaging of the transfected HEK 293 cells, an upright fluorescence microscope system (Slicescope, Scientifica, UK) that is equipped with a 460 nm LED (UHP-Mic-LED-460, Prizmatix, Israel), a GFP filter set (GFP-3035D-OMF, Semrock, USA) and the DaVinci-2K low noise CMOS camera system (SciMeasure analytical systems, USA) was used. The optical images for HEK 293 cells were acquired at 100 Hz frame rate unless otherwise noted.

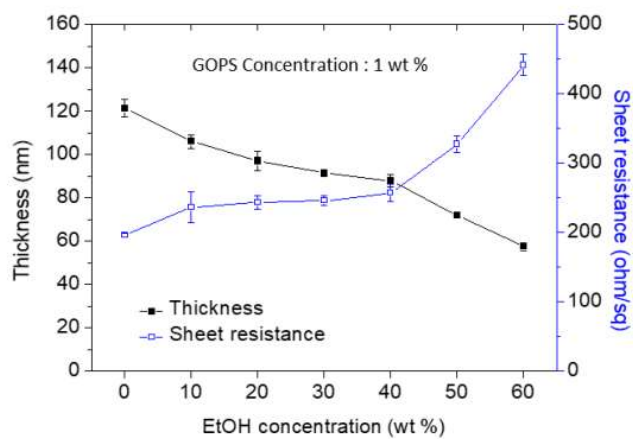
To inject current pulses onto the sample, an isolated current stimulator (DS3; Digitimer, UK) was connected to the thin film electrode. A patch-clamp amplifier (Multiclamp 700B) together with a digitizer (Digidata 1550B; both by Molecular devices, USA) controlled the stimulus waveform and sent a signal to the current stimulator to initiate each stimulation step.

3.3 Results

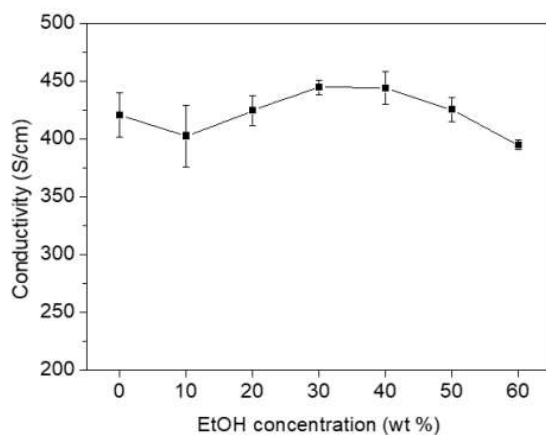
3.3.1 Electrical characteristics of PEDOT:PSS-GOPS

Sheet resistance and thickness were measured to evaluate the electrical characteristics of the PEDOT:PSS, which was cross-linked by (3-lycidyloxysilane (GOPS) according to the ethanol concentration ratio. Figure 3.2 (a) shows the thickness and surface resistance values according to the ethanol ratio at 1 wt % of GOPS. In the case of cross-linked PEDOT: PSS by 1 wt % of GOPS without ethanol, the thickness was about 120 nm. As the ethanol concentration ratio increased, the thickness decreased with decreasing PEDOT:PSS content. Similarly, sheet resistance was measured to be about 195 ohm/sq without ethanol and appeared to increase gradually with increasing ethanol concentration ratio. The calculated conductivity values using thickness and sheet resistance values are shown in figure 3.2 (b). If ethanol is not included, approximately 420 S/cm. If ethanol is increased by 10 wt %, conductivity is reduced to about 400 S/cm. As the ratio of ethanol concentration increased, the conductivity increased and the conductivity value at the ratio of 30 wt % and 40 wt % increased by about 5% compared to when ethanol was not mixed. It was found that the conductivity decreased again from 50 wt% of the ethanol concentration ratio, and the

conductivity of about 395 S/cm was observed at the 60 wt% of the ethanol concentration ratio. Figure 3.3 (a) shows the thickness and sheet resistance according to the GOPS content when the ethanol concentration ratio is 30 wt %. As the GOPS content increased, the thickness and sheet resistance increased and the conductivity decreased as illustrated. Figure 3.3 (b) shows the conductivity calculated by the thickness and sheet resistance according to the GOPS content when the ethanol concentration ratio is 30 wt %. Without GOPS, conductivity at the ethanol concentration ratio of 30 wt % is about 800 S/cm, and if conductivity at 3 wt % of GOPS is about 140 S/cm at the ethanol concentration ratio of 30 wt %.



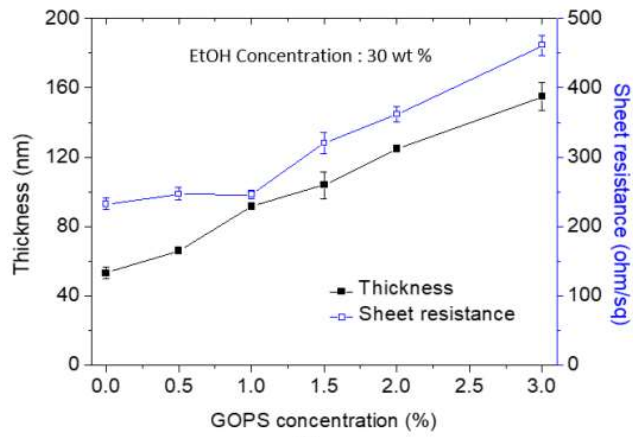
(a)



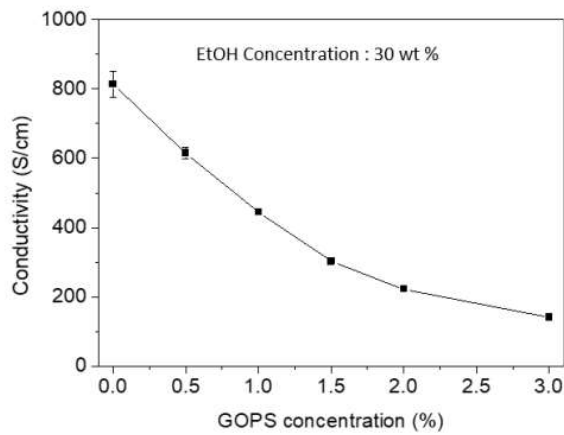
(b)

Figure 3. 2 (a) Thickness, surface resistance and (b) conductivity of the PEDOT:PSS film according to ethanol concentration.

The coating solution consists of GOPS 1 wt % for PH1000 mixed with EG 5 %. PH1000 solution with EG and GOPS was mixed with ethanol from 0 wt % to 60 wt %.



(a)



(b)

Figure 3. 3 (a) Thickness, (b) surface resistance and (c) conductivity of the PEDOT:PSS film according to GOPS concentration.

The coating solution consists of GOPS from 0 wt % to 3 wt % for PH1000 mixed with EG 5 %. PH1000 solution with EG and GOPS was mixed with 30 wt % of ethanol.

3.3.2 FTIR analysis of PEDOT:PSS-GOPS

FTIR measurements were made to view information on the chemical bonding and molecular structures of the PEDOT:PSS and GOPS according to ethanol. Figure 3.4 shows the FTIR spectra from 400 cm^{-1} to 4000 cm^{-1} of PEDOT:PSS with 1 wt% of GOPS depending on the ethanol concentration ratio. 1541 cm^{-1} and 1203 cm^{-1} peak are related to the definition of phenyl rings attached to the sulfonate groups of PSS [67, 106]. -SO_3 symmetric stretching vibrations are shown in 1038 and 1010 cm^{-1} . The intensity of the 1541 cm^{-1} peak associated with PSS increased with increasing ethanol. In addition, at more than 30 wt % of ethanol concentration, a new peak was found at 3750 cm^{-1} . The peak of 3750 cm^{-1} and 3650 cm^{-1} are related to the formation of isolated surface silanols and silanols closed enough to hydrogen bond [107]. The process of hydrolysis and condensation depends on the pH concentration [108]. In acidic media, hydrolysis is very fast and condensation is very slow. Both are generally slow in neutral media, slow in hydrolysis and fast condensation in basic media. Generally, known pH concentrations of PH1000 are about 2 acidic. Figure 3.5 (a) shows the pH concentration according to the ethanol mixing ratio in the PH1000 solution. When the ethanol was not mixed, the pH concentration of the PH1000 solution was

2, and when the ethanol was mixed 10 wt %, the concentration dropped to about 1.6 because the addition of ethanol, a protic solvent, also makes hydronium more hydrophilic, making the reaction medium more acidic [109]. When the ethanol mixture ratio was 20 wt %, the pH was about 2 again. As the ethanol was gradually increased, the pH was increased. To crosslink between GOPSs, trimethoxysilane groups are converted to hydroxyl groups by hydrolysis and condensation occurs as shown in figure 3.5 (b) [110]. At pH levels below 2, GOPS hydrolysis occurs rapidly and condensation occurs slowly. As a result, 3750 cm^{-1} peak associated with isolated silanols did not appear as geminal silanols were increased. On the other hand, when the ethanol mixing ratio is more than 30 wt%, the crosslinking occurs well as the condensation increases with the increase of the pH concentration. As a result, the presence of isolated silanols increases instead of geminal silanols, resulting in a large intensity at the 3750 cm^{-1} peak.

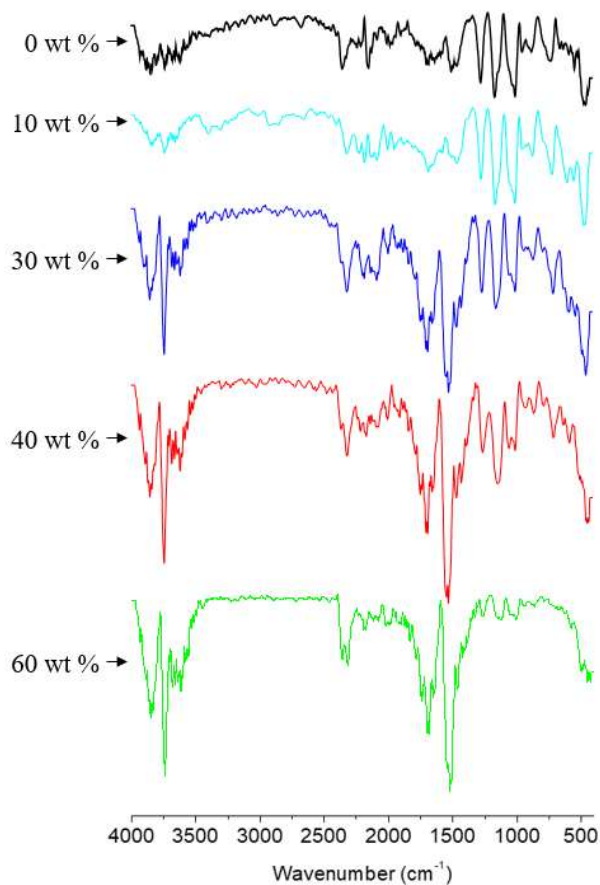
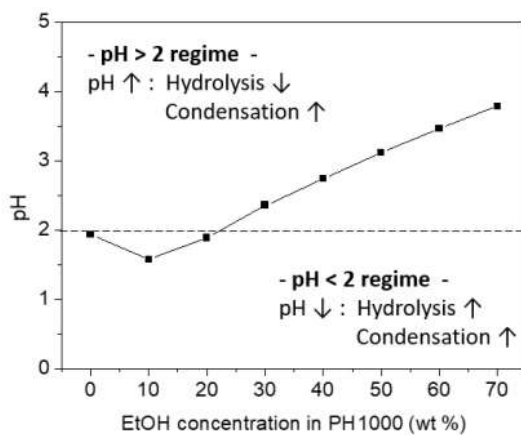
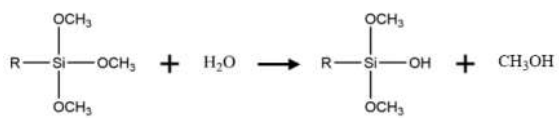


Figure 3. 4 FTIR spectra from 400 cm^{-1} to 4000 cm^{-1} of PEDOT:PSS with 1 wt% of GOPS depending on ethanol concentration ratio.

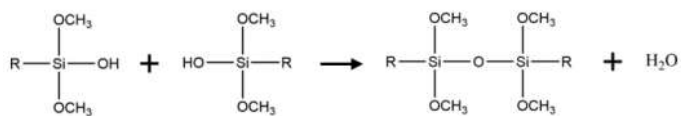


(a)

1. Hydrolysis



2. Condensation



(b)

Figure 3. 5 (a) The pH concentration according to the ethanol mixing ratio in the PH1000 solution, (b) hydrolysis and condensation of trimethoxysilane of GOPS.

3.3.3 Contact angle of PEDOT:PSS-GOPS

The hydrolysis effect of GOPS in the PEDOT:PSS film also showed differences in contact angle data. Figure 3.6 shows the contact angle value according to the ethanol concentration ratio for water. It had a value of about 58 degrees from the ethanol concentration ratio of 10 wt % to the ethanol ratio of 40 wt %. The ethanol concentration ratio of 40 wt % showed a value of about 50 degrees and increased again at an ethanol concentration ratio of 50 wt % or higher. More silanols in GOPS result in more hydrophilic surface conditions, which appear to have the most silanols at an ethanol concentration ratio of 30 wt % or 40 wt %. In other words, it acts as a hydrolysis catalyst for GOPS by ethanol, showing the most effect at ethanol mixing ratio 30 or 40 wt % in particular.

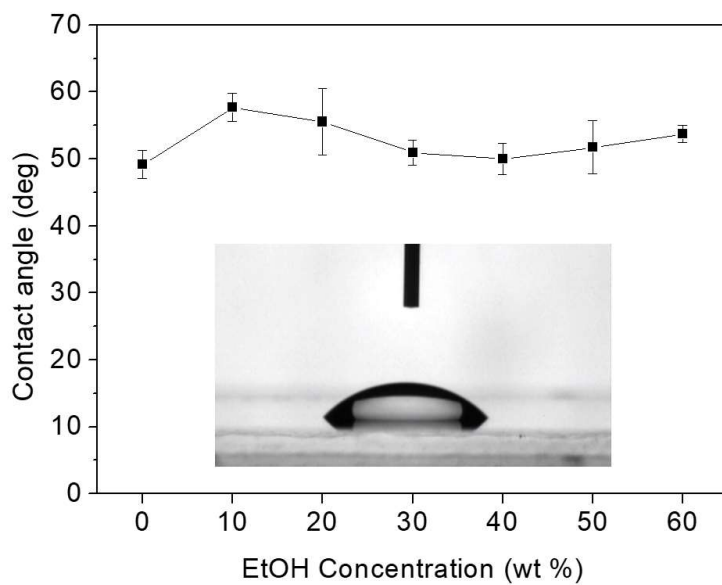


Figure 3. 6 Contact angle for water on a glass substrate coated with PEDOT: PSS according to ethanol concentration ratio at 1 wt % of GOPS.

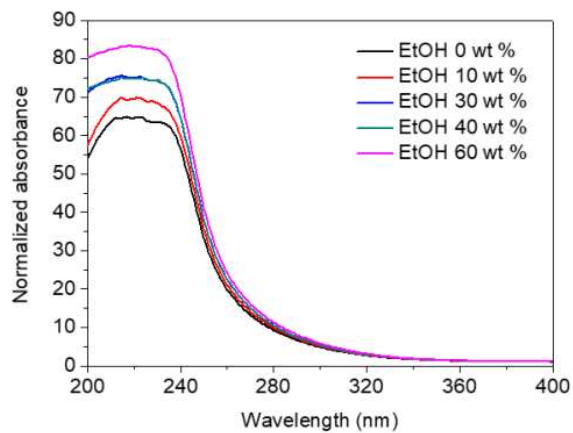
3.3.4 UV spectrum of PEDOT:PSS-GOPS

Figure 3.7 shows the normalized absorbance at wavelengths from 200 nm to 1000 nm, depending on the ethanol concentration ratio. Each absorbance was normalized to the wavelength with the lowest value. PSS of PEDOT:PSS has a phenyl group that affects the absorption wavelength at 225 nm [111]. Post-treatment of pristine PEDOT: PSS increases the conductivity of the PEDOT: PSS film surface by removing the hygroscopic and insulating PSS. As the PSS ratio is lowered, the absorption in the 225 nm band is reduced. But the results of PEDOT:PSS with ethanol were the opposite as shown in figure 3.7 (a). As the ethanol mixing ratio increased, the absorbance at 225 nm increased, which increased the number of phenyl groups in PSS. This means that many PSSs are cross-linked by GOPS.

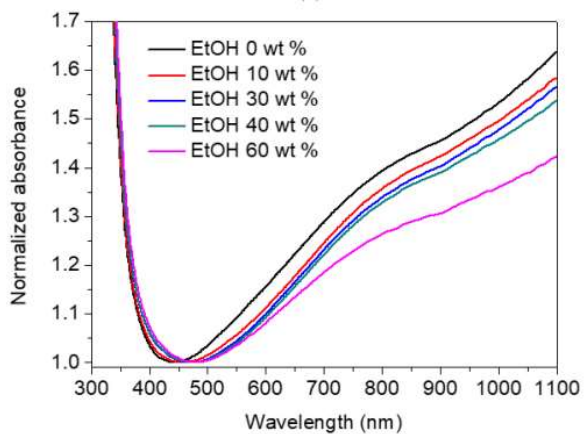
The increase in conductivity obtained by doping PEDOT:PSS is due to the formation of freely moving soliton, polaron, and bipolaron. Changes in absorbance in the near-infrared region began to occur when the ethanol concentration ratio was above 40 wt% as shown in figure 3.7 (b). In particular, when the ethanol mixing ratio of 60 wt% it was confirmed that the absorption is lower than other conditions. This lower absorption is due to the inhibition of the formation of soliton, polaron,

and bipolaron, which contributes to the decrease in conductivity [112].

It was also confirmed that the UV spectrum was red-shifted or bathochromic shifted as the ethanol concentration ratio increased by the solvent effect.



(a)



(b)

Figure 3. 7 Normalized absorbance at wavelengths from 200 nm to 1000 nm, depending on the ethanol concentration ratio.

3.3.5 Raman spectrum of PEDOT:PSS-GOPS

Raman spectrums were made to view information on the chemical and structural information of the PEDOT:PSS film. The main Raman peaks of PEDOT are found at 1524 cm^{-1} , 1452 cm^{-1} , 1383 cm^{-1} , and 1272 cm^{-1} assigned to the $C_{\alpha} = C_{\beta}$ asymmetrical, $C_{\alpha} = C_{\beta}$ symmetrical, $C_{\beta} - C_{\beta}$ stretching and $C_{\alpha} - C_{\alpha'}$ interring stretching vibration, respectively [85]. The main peaks of the PSS appear at 1110 cm^{-1} and 1000 cm^{-1} . Figure 3.8 shows the normalized intensity of PEDOT: PSS with and without ethanol at 1 wt % GOPS normalized to the 1452 cm^{-1} Raman peak.

Regardless of whether ethanol was mixed or not, EG was included in PEDOT:PSS and benzoid-to-quinoid shift was observed at near 1452 cm^{-1} peak compared to pristine PH1000 [113]. In addition, the peak change of PSS was not observed, but the intensity of $C_{\alpha} = C_{\beta}$ symmetrical, $C_{\beta} - C_{\beta}$ stretching and $C_{\alpha} - C_{\alpha'}$ interring stretching vibration was decreased in the case of PEDOT: PSS mixed with ethanol.

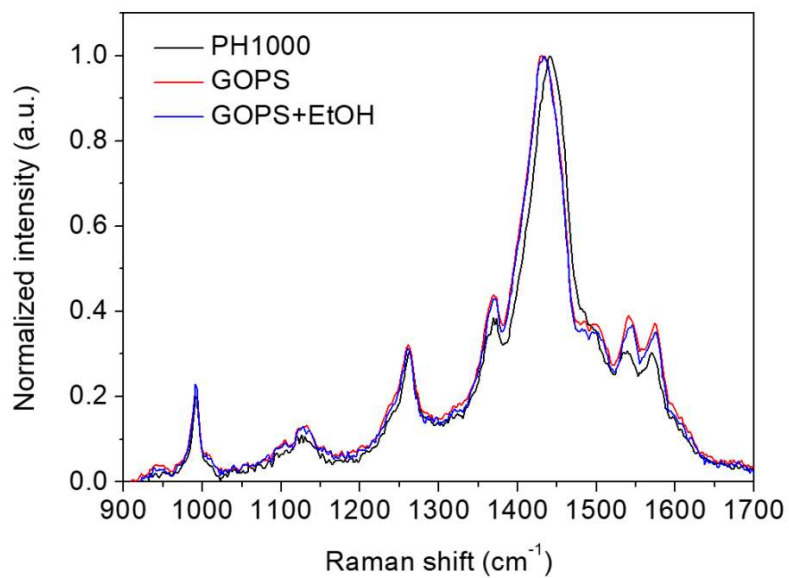


Figure 3. 8 Raman spectra of PEDOT:PSS thin films with and without ethanol at 1 wt% of GOPS.

3.3.6 Surface roughness of PEDOT:PSS film

Figure 3.9 shows the topography image of PEDOT:PSS thin films mixed with 0 wt%, 30 wt% and 50 wt% of ethanol concentration at 1 wt% of GOPS measured by Atomic force microscopy. In the case of PEDOT:PSS with GOPS without ethanol, the average roughness value was 1.428 nm. At 30 wt % and 50 wt % of ethanol concentration ratio, the average roughness value was 1.376 nm and 1.266 nm, respectively. Although the difference is low, average roughness decreases as ethanol is mixed.

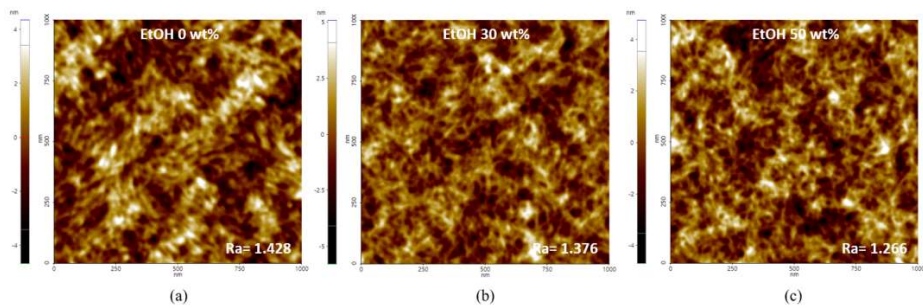


Figure 3. 9 Atomic force microscopy images of the topography PEDOT:PSS thin films mixed with (a) 0 wt%, (b) 30 wt% and (c) 50 wt% of ethanol concentration at 1 wt% of GOPS. The measured size of the topography is $1 \mu\text{m} \times 1 \mu\text{m}$.

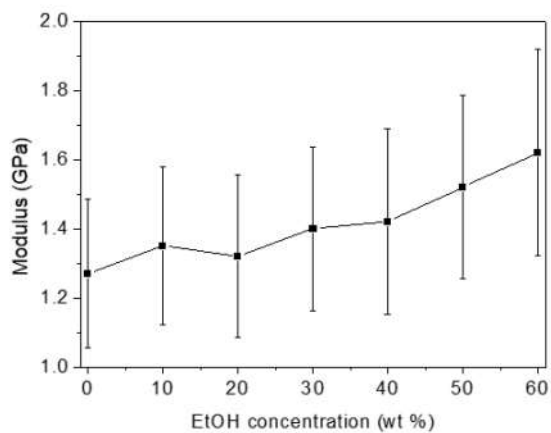
3.3.7 Mechanical properties of PEDOT:PSS-GOPS

The AFM indentation method was used to measure the modulus of PEDOT: PSS thin film. Modulus values of PEDOT:PSS film according to ethanol concentration at 1 wt% of GOPS were measured using DMT models. Figure 3.10 (a) shows The modulus of PEDOT:PSS film measured by AFM indentation for the DMT models according to the ethanol concentration ratio at 1 wt % of GOPS. At 10 wt% ethanol, modulus of PEDOT:PSS film increased and then decreased again at 20 wt %. Above 20 wt% of ethanol, the modulus value increased as the ethanol mixture ratio increased. This result is similar to that of hydrolysis and condensation according to ph.[114] As the pH value approaches 7, the hydrolysis efficiency decreases and condensation increases. However, when the pH value is 2 or less, the condensation efficiency increases again. The pH value of PH1000 is 2, so the condensation efficiency is not the best, and the pH value changed by mixing ethanol increases condensation efficiency. At 10 wt% of ethanol, condensation efficiency increases due to the pH lower than 2, but modulus increases at 20 wt% of ethanol.

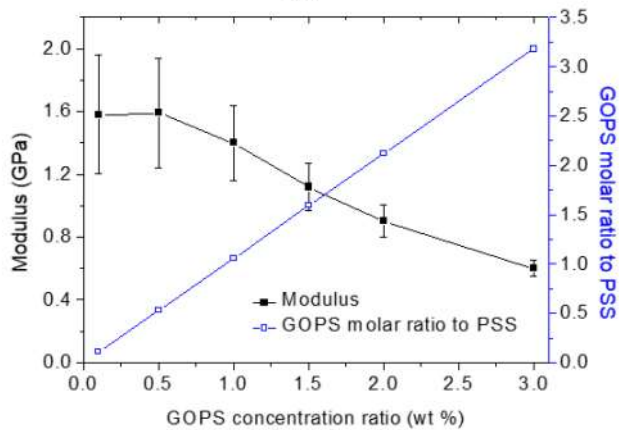
Figure 3.10 (b) shows the modulus according to the GOPS concentration ratio at 30 wt % of the ethanol concentration ratio. The

best modulus value was obtained when the GOPS content was 0.5 wt%, which was about 1.6 GPa. If the GOPS content was more than 0.5 wt%, the modulus value decreased with increasing GOPS content due to the increased content of GOPS compared to PSS as shown in the blue line in figure 3.10 (b). When the GOPS content was 0.1 wt%, the modulus value was slightly lower than that with the GOPS content 0.5 wt%.

In order to confirm the stability of PEDOT: PSS according to ethanol mixing, a glass substrate coated with PEDOT: PSS was placed in water and ultrasonic waves were applied. In the same GOPS content of 0.1 wt%, PEDOT: PSS was not mixed with ethanol, and after 5 minutes of sonication, the PEDOT: PSS film was peeled off as shown in figure 3.11 (a). On the other hand, when 30 wt% of ethanol was mixed, the PEDOT: PSS film did not peel off even after 5 minutes of sonication treatment due to the increased efficiency of hydrolysis and condensation of GOPS by ethanol as shown in figure 3.11 (b).



(a)



(b)

Figure 3. 10 The modulus of PEDOT:PSS film measured by AFM indentation for the DMT models according to (a) the ethanol concentration ratio at 1 wt % of GOPS. (b) The modulus of PEDOT:PSS film and GOPS molar ratio of PSS according to GOPS concentration ratio at 30 wt % of ethanol.



(a)



(b)

Figure 3. 11 Surface image of PEDOT:PSS with GOPS 0.1 wt % (a) with and (b) without ethanol after sonication for 5 min.

3.3.8 Impedance & CSC measurement of PEDOT:PSS-GOPS

The figure 3.12 shows the impedance of PEDOT:PSS film from frequency 10^0 Hz to 10^5 Hz the conditions of 0.1 wt% & 1 wt% ratio of GOPS with 30 wt % of ethanol concentration, 1 wt% ratio of GOPS without ethanol and gold. The area of the PEDOT:PSS film for measuring the impedance is about $1,200 \mu\text{m}^2$ and PEDOT:PSS film was coated and patterned on gold. For the same GOPS content at 1 wt %, the impedance of PEDOT:PSS difference was largely depending on whether ethanol was mixed. Below about 10 Hz, the impedance of PEDOT: PSS mixed with ethanol was measured low, but higher impedance was shown in the region above 10 Hz. The impedance difference of PEDOT:PSS with and without ethanol increased up to about 10^3 Hz, but the impedance difference of them decreased back to 10^5 Hz. This difference is caused by the structural change of PEDOT:PSS film due to the enhanced efficiency of the cross-linking of GOPS. PEDOT:PSS with and without ethanol at 1 wt % of GOPS had higher impedance than gold in some range of the high-frequency.

PEDOT: PSS mixed with ethanol at 0.1 wt % of GOPS had similar impedance values below 10^2 Hz and lower impedance values above 10^2 Hz compared to PEDOT: PSS without ethanol at 1 wt % GOPS. At high

frequency, the difference in impedance between PEDOT: PSS mixed with ethanol at 0.1 wt % of GOPS and PEDOT: PSS without ethanol at 1 wt % GOPS were apparent which may be caused by the thickness difference and the degree of doping of PEDOT: PSS by ethanol. At 1 kHz frequency, the impedance values of gold, PEDOT:PSS with GOPS wt 1 % and without ethanol and PEDOT:PSS with GOPS 0.1 wt % and 1 wt % with ethanol were 987 k Ω , 115 k Ω , 51 k Ω , and 834 k Ω . respectively.

Figure 3.12 shows the plotted CV image during sweep between -0.6 V and 0.8 V at 50 mV/s of sweep speed and CSC calculated using the CV data obtained. At the same GOPS content of 1 wt%, the CSC value of PEDOT:PSS with ethanol was shown to increase about 3 times than that of PEDOT:PSS without ethanol. In general, the cathodic CSC value of PEDOT:PSS was higher than anodic CSC value, but anodic CSC value was higher by GOPS. On the other hand, in the case of between PEDOT: PSS mixed with ethanol at 0.1 wt % of GOPS, the cathodic CSC value was higher than that of the anodic CSC value and was similar to PEDOT: PSS without ethanol at 1 wt % GOPS.

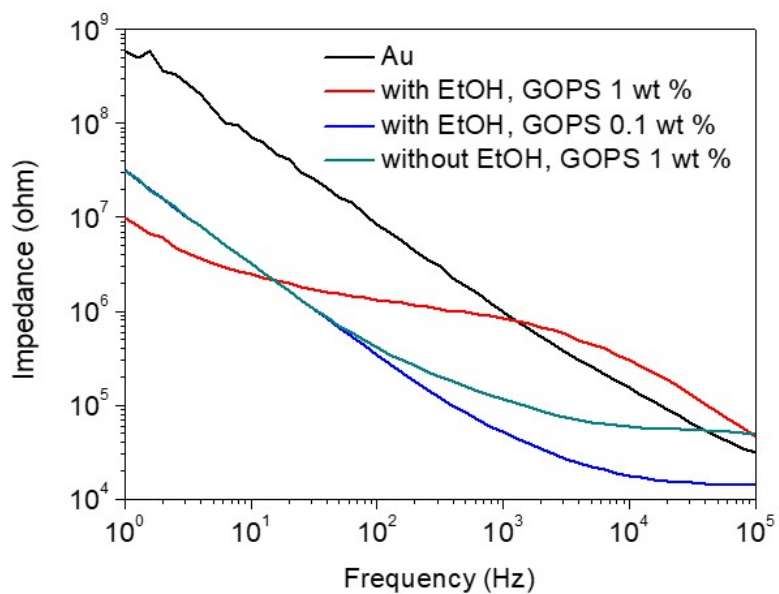


Figure 3. 12 Impedance of PEDOT:PSS film from frequency 10^0 Hz to 10^5 Hz the conditions of 0.1 wt% & 1 wt% ratio of GOPS with 30 wt % of ethanol concentration, 1 wt% ratio of GOPS without ethanol and gold.

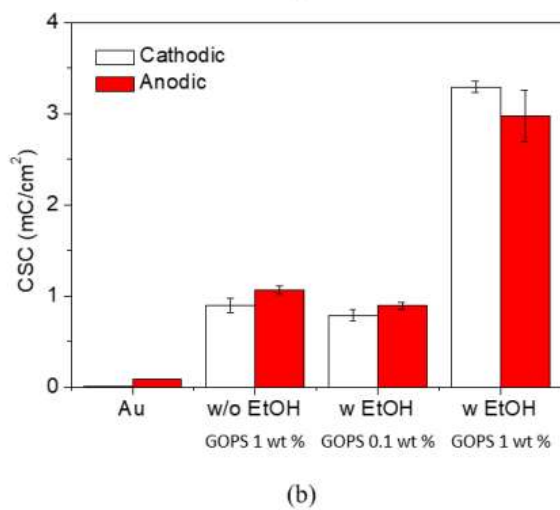
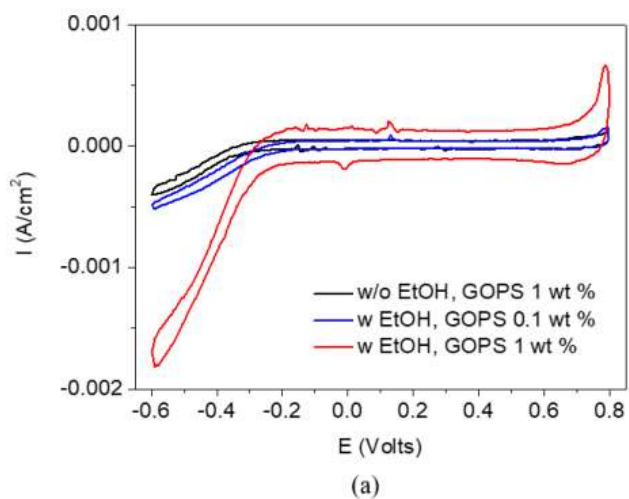


Figure 3. 13 (a) Cyclic voltammetry (CV) curve for PEDOT:PSS with ethanol at 0.1 wt % and 1 wt % of GOPS and without ethanol at 1 wt % of GOPS. (b) charge storage capacity for cathodic and anodic calculated by CV.

3.3.9 Fluorescent voltage imaging of cultured mammalian cells stimulated by the PEDOT:PSS electrode

In order to evaluate PEDOT:PSS-GOPS electrode with ethanol of 30 wt % and GOPS of 0.1 wt %, voltage-dependent fluorescence image was used using genetically-encoded voltage indicators (Bongwoori-R3). Figure 3.14 and 3.15 show the fluorescent voltage imaging and voltage-dependent fluorescence changes from cells depicted in figure 3.14(f) of cultured mammalian cells stimulated by the PEDOT:PSS-GOPS electrode with varying current amplitudes. The position of the electrode is shown in the dotted circle in figure 3.14 (a) and the current waveform used for the experiment is shown in the inset in figure 3.15 (a). Stimulation of cathodic pulses causes the HEK 293 cell to become hyperpolarization, resulting in fluorescence imaging of the fluorescent voltage indicator. As the current amplitude of the electrode increases, the voltage-dependent fluorescence changes also increase in all locations. At a stimulus duration of 10 ms, the minimum stimulus current of HEK 293 cell was above about 3 μA and the charge density was about 2.39 mC/cm^2 .

Figure 3.16 and 3.17 show fluorescent voltage imaging of HEK 293 cells expressing a fluorescent voltage indicator (Bongwoori-R3) over time after stimulation with current stimuli of 20 μA and fluorescence

traces acquired from area 1, 2, 3, and 4 depicted in figure 3.14(f). Fluorescence changes rapidly within the electrode area as shown in figure 3.17 (a-c). However, the change in fluorescence occurred late or not in the cells at the position away from the electrode due to the gap junction of HEK 293 cell as shown in figure 3.16. Gap junction allows for the intercellular delivery of ions, metabolites, and signals transduction molecules required to regulate cellular activity in physiological systems [115]. Cells in area 4 showed fluorescence changes about 1.5 seconds after stimulation by gap junctions as shown in figure 3.17 (d).

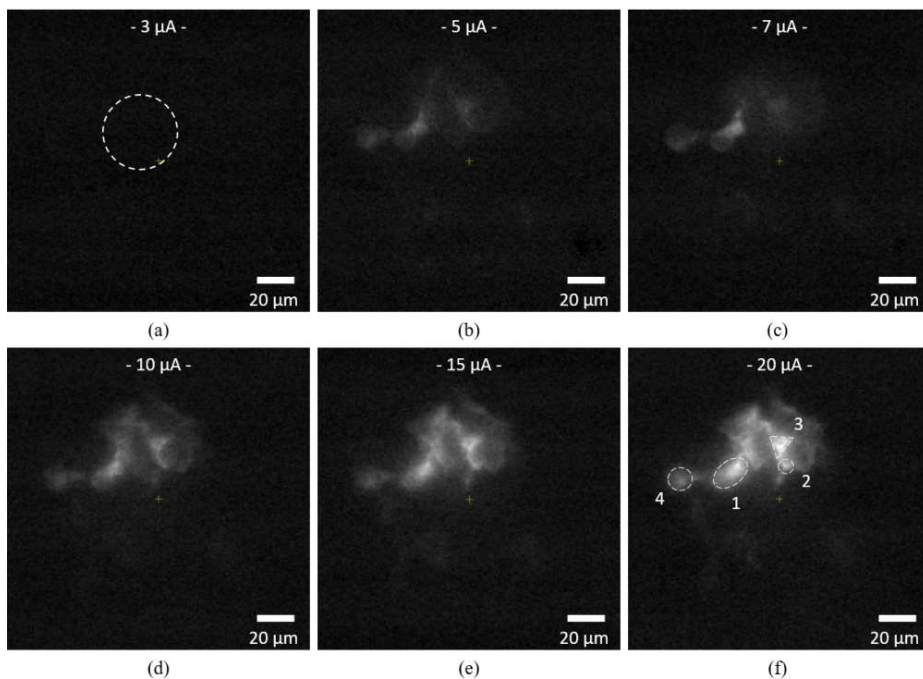


Figure 3. 14 Fluorescent voltage imaging of HEK 293 cells expressing a fluorescent voltage indicator (Bongwoori-R3) responding to current stimuli of (a) 3 μ A, (b) 5 μ A, (c) 7 μ A, (d) 10 μ A, (e) 15 μ A, and (f) 20 μ A from PEDOT:PSS-Ethanol electrode.

The dotted circle in (a) indicates the PEDOT:PSS electrode. Each dotted circle in (f) represents a HEK 293 cell.

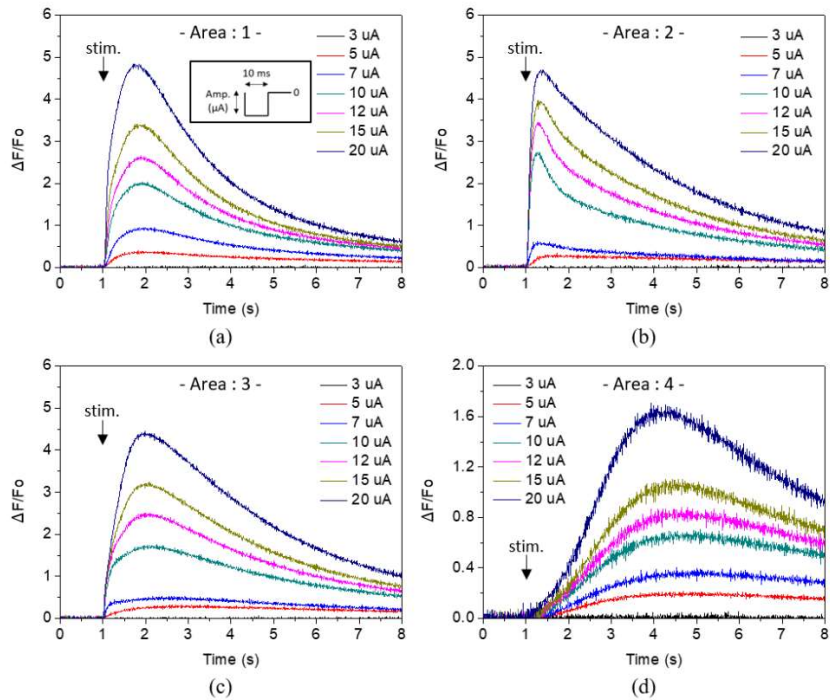


Figure 3.15 (a-d) Voltage-dependent fluorescence changes with varying current amplitudes from cells depicted in figure 3.14 (f). Inset in (a) shows the current input waveform used for the experiment.

$\Delta F/F_0$ represents fractional fluorescence change of the traces (ΔF value) divided by the average of 10 pre-stimulus frames (F_0 value).

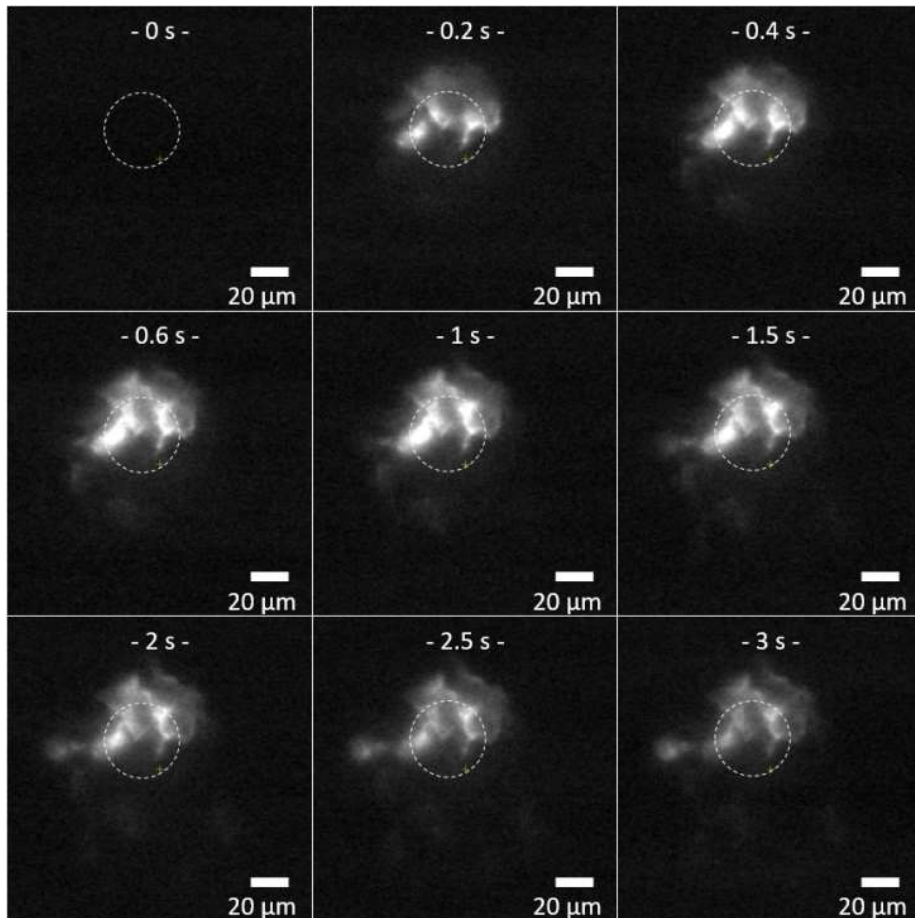


Figure 3. 16 Fluorescent voltage imaging of HEK 293 cells expressing a fluorescent voltage indicator (Bongwoori-R3) over time after stimulation with current stimuli of 20 μ A.

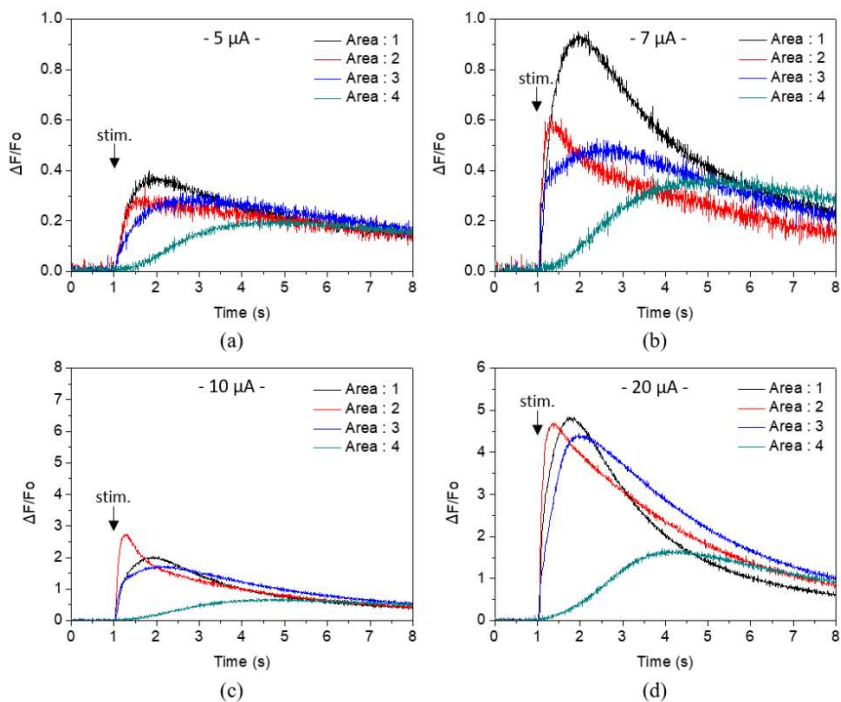


Figure 3.17 Fluorescence traces acquired from area 1-4 with a current amplitude of (a) 5 μA , (b) 7 μA , (c) 10 μA and (d) 20 μA .

$\Delta F/F_0$ represents fractional fluorescence change of the traces (ΔF value) divided by the average of 10 pre-stimulus frames (F_0 value).

3.4 Discussion

In this chapter, ethanol improved the crosslinking between PEDOT:PSS and GOPS, increasing the mechanical properties. When 1 wt% of GOPS was added to PH1000 containing 5% of EG, the conductivity of PEDOT:PSS film increased by about 5% from 30 wt% to 40 wt% of ethanol compared to PEDOT:PSS film without ethanol. The FITR analysis confirmed that the crosslinking efficiency increased as the condensation efficiency of the trimethoxysilane group of GOPS was increased by ethanol. The crosslinking efficiency of GOPS by ethanol was found to be highest at ethanol concentration ratio of 30 wt % by AFM indentation methods. The modulus of PEDOT:PSS film measured by AFM indentation methods increased from 1.3 times when ethanol was mixed than when ethanol was not mixed at 1 wt % of GOPS. In addition, the modulus value of PEDOT:PSS film mixed ethanol at 0.1 wt % of GOPS was higher than that without ethanol at 1 wt % GOPS, despite the low GOPS content. The cross-linking efficiency by ethanol showed high stability even at low GOPS content through sonication experiments. The result is a change in pH concentration due to mixing in ethanol and PH1000 solution. The more acidic the faster hydrolysis but the slower the condensation, the more basic the opposite. When the mixing ratio of

ethanol was 20 wt % or less, the pH concentration had a value below the pH concentration of PH1000, but at 30 wt % or more, the pH concentration increased. As a result, condensation efficiency was increased and cross-linking efficiency was also increased.

The ethanol mixture showed a significant difference in PEDOT: PSS impedance at 1 wt% of GOPS content due to changes in electrical double-layer capacitance and charge transfer resistance due to increased crosslinking efficiency. On the other hand, the CSC value of ethanol-mixed PEDOT: PSS was about three times higher than that of PEDOT: PSS without ethanol. The impedance of the PEDOT: PSS mixed with ethanol at 0.1 wt % of GOPS and without ethanol at 1 wt % of GOPS had similar impedances in the low-frequency region, but the impedance of the PEDOT: PSS mixed with ethanol had lower in the high-frequency region. Although the impedances differed, the CSC values were measured similarly. Increasing the crosslinking efficiency by ethanol resulted in increased modulus and reduced impedance with less impregnation, and increased stability. This result can be used as a useful electrode by increasing the stability and increasing the efficiency with low impedance at the neural electrode interface using PEDOT: PSS.

The feasibility as a neural electrode was evaluated using a mammalian

cell. HEK-293 cells expressing a genetically-encoded fluorescent voltage indicator were stimulated using PEDOT:PSS-GOPS electrode with diameter of 40 μm at a current of 2 μA . When the current was increased to 20 μA , the change in fluorescence of Bongwoori-R3 expressed cells also shown to increase. This shows that the stimulus is sufficiently generated by the PEDOT: PSS electrode.

Chapter 4. Development of an Optoelectronic Neural Stimulator Combined with a Photovoltaic Cell and a Light Emitting Diode for Optogenetic Application

4.1 Introduction

Electrostimulation is the most common neural stimulation technology applied to modern medicine and improved over the decades. However, it generally affects neighboring neurons and makes it difficult to classify single-cell mechanisms. One solution proposed to selectively stimulate cells is optical stimulation through optogenetics. The Channelrhodopsin-2 (ChR2) protein is a blue light-sensitive membrane protein that appears in the membrane region and neurons [29-31]. Blue light is used to stimulate ChR2-expressed cells. However, blue light has a disadvantage of short wavelength and low tissue penetration depth. To solve this problem, various methods of transmitting blue light to target cells have been developed.

In optogenetics research, the method for transmitting light to target cells is a mainly optical fiber or waveguide-based [34, 36, 41] and micro

light-emitting diode (LED) based [33, 116]. A single optical fiber is a simple way to stimulate ChR2-expressed cells in vivo experiments. Optical fiber has been developed in many forms or combined with electrodes (optrode) [37-40]. Tapered optical fiber, patched with concentrated ion beam, enable selective and dynamic lighting of different brain regions along with it [35]. The site can be selected via a simple couple ring strategy at the optical fiber input. An optrode consisting of a tapered coaxial optical waveguide incorporated in multiple electrode recording arrays within the 100 element cortex can simultaneously perform light stimulation and electrical recording [117]. However, the use of optical fiber has a major disadvantage of the spatial limits of the waveguide itself. Hardwired connections to external light sources can also cause behavioral constraints in animal behavior experiments.

Another way to stimulate is to use micro LEDs. Micro LEDs directly attached to the probe can stimulate cells directly near the cell. Instead of inserting micro LEDs directly into the brain, they can be connected to the waveguide to transmit and stimulating light. These micro LEDs can be operated by a wireless power supply. Wireless power supply systems are very helpful in limiting animal behavior in animal experiments.

Many researchers use inductive coils to provide wireless power [118, 119]. Other researchers have also performed power transmission using Photovoltaic(PV) [120] or ultrasound [121] because efficiency decreases dramatically as devices become smaller.

In this chapter, we developed a wireless stimulator combining PV and LEDs for optogenetics research. PV cells convert optical energy into electrical energy, and LEDs convert electrical energy back to optical energy with blue light. PV cells are designed to absorb the near-infrared light (NIR; 830 to 850 nm). NIR wavelengths have a relatively high penetration depth through brain tissue; three times the blue wavelengths [122]. The NIR can penetrate to a depth of approximately 1.5mm or more [123]. This means that the PV cell can transmit power at depths to the brain at least 1.5mm. The PV cell is also a tandem structure that allows the battery to produce high absorption efficiency and voltage to operate the LEDs. LEDs are designed to emit blue light (450 nm) for stimulation of ChR2-expressed cells. PV and LED are made in micro-size through the semiconductor process and are made with one implantable stimulator. In the previous study, the stimulator combined with PV and LED simply has the same as the incident direction of NIR and the emission direction of blue light. If the incident direction of NIR and the emission direction

of blue light of stimulator combined with PV cell and LED, it makes neural stimulation difficult in deeper brain regions as shown in figure 4.1. To solve directional problems, the through-hole via process was applied to PV cells in order to differentiate between the NIR incident direction and the blue emission direction. After the PV cell and LED were bonded, they were encapsulated with biocompatible epoxy. The *in vitro* experiment indicated that the device could be used for deep brain stimulation, with the ChR2-expressed HEK293 cells and PV-LED stimulator devices driven by NIR.

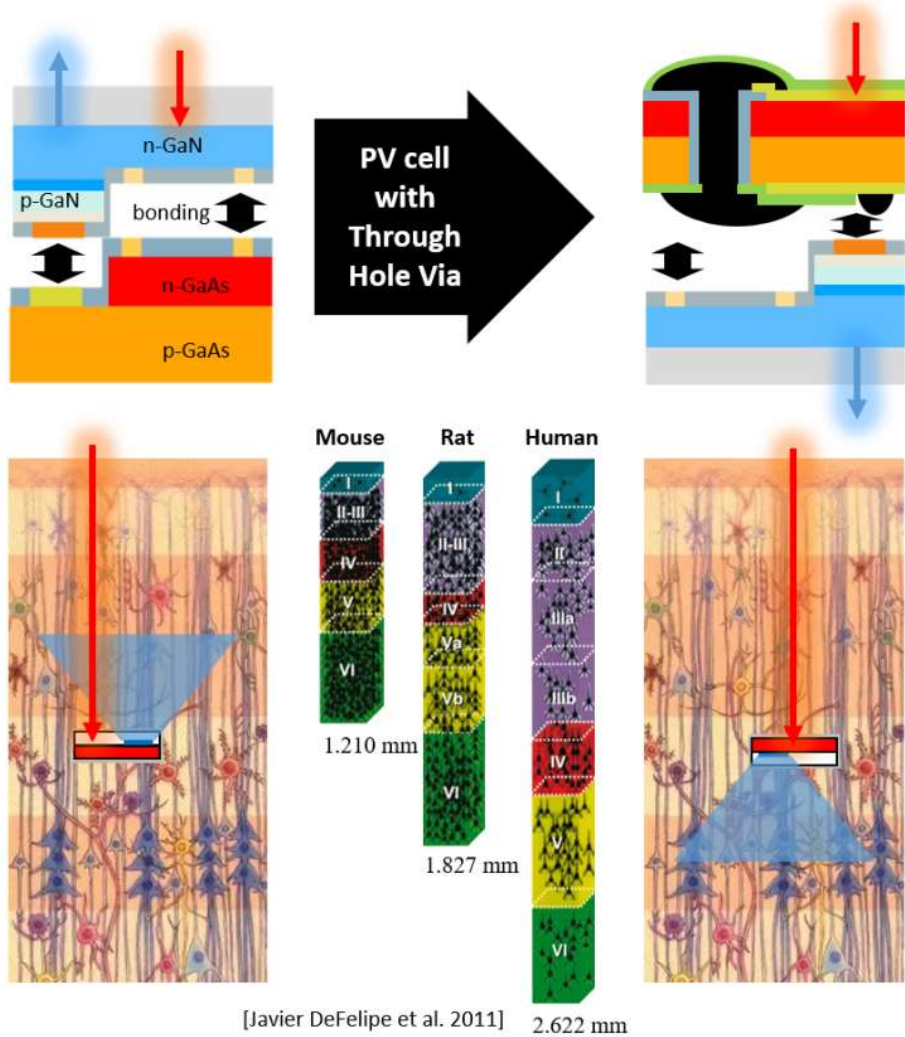


Figure 4. 1 Comparison of previously studied PV-LED Stimulator with Stimulator combined PV with through-hole via and LED (ref. [123]).

The stimulator combined PV with through-hole via and LED can stimulate ChR2 expressing cells in deeper areas.

4.2 Materials and methods

4.2.1 Light-emitting diode (LED) and photovoltaic cell (PV)

LEDs have an epitaxial layer containing InGaN multiple quantum well (MQW) grown in sapphire wafers by metalorganic chemical weather deposition (MOCVD) as shown in figure 4.2 (b). LED substrates were purchased from EpiVally Co., Ltd. PV cells consist of a PN-junction with a heterogeneous structure of gallium-sodium / aluminum-gallium-sodium (GaAs / AlGaAs) as shown in figure 4.2 (a) [124]. The tandem structure has been introduced to improve absorption efficiency to provide the voltage to operate the LED. The tandem structure consists of three p-i-n photovoltaic cells, each having a unique layer thickness that is optimally designed and connected in series by two thin tunnel connections. The top layer absorbs one-third of the incident photons, the middle cell absorbs half of the transmitted light and the last layer absorbs the rest. PV cell windows manufactured to input the fundamental light has an area of approximately $48,000 \mu\text{m}^2$. To change the incident direction of the PV cell and the direction of the emission of LEDs, the penetration hole via process was applied to the PV cell. After the PV cell was bonded to the through-hole via and LED, the bonded device was covered with UV-cured epoxy for encapsulation.

A schematic design of the bonding process and light pathway from incident NIR light to emitting blue light is shown in figure 4.3. The NIR photons are absorbed by three PV cells and the absorbed light can be converted into electrical energy simultaneously. The transferred energy activates LEDs to emit short-wave blue light. Finally, the blue light from the LED stimulates the ChR2-expressed cells.

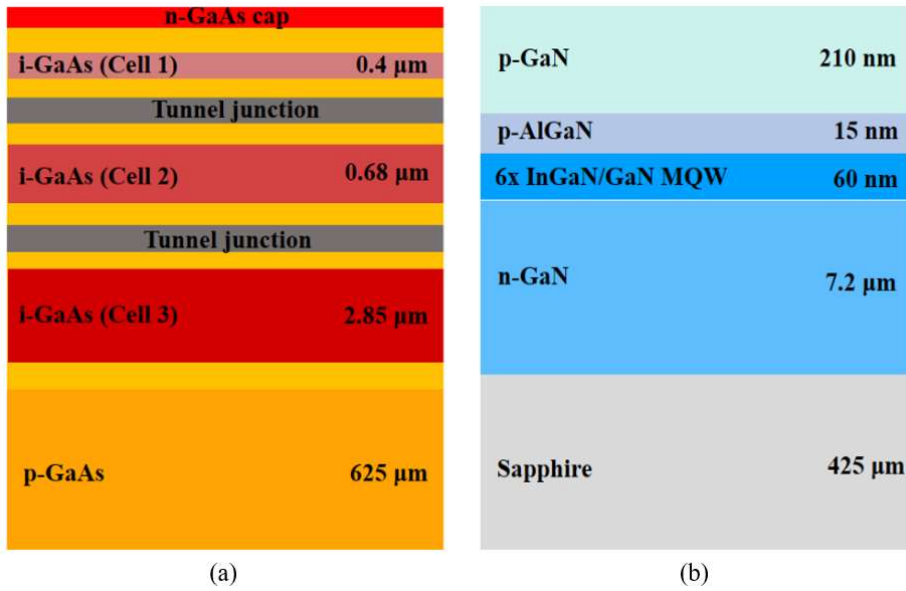


Figure 4. 2 Structure of (a) PV and (b) LED.

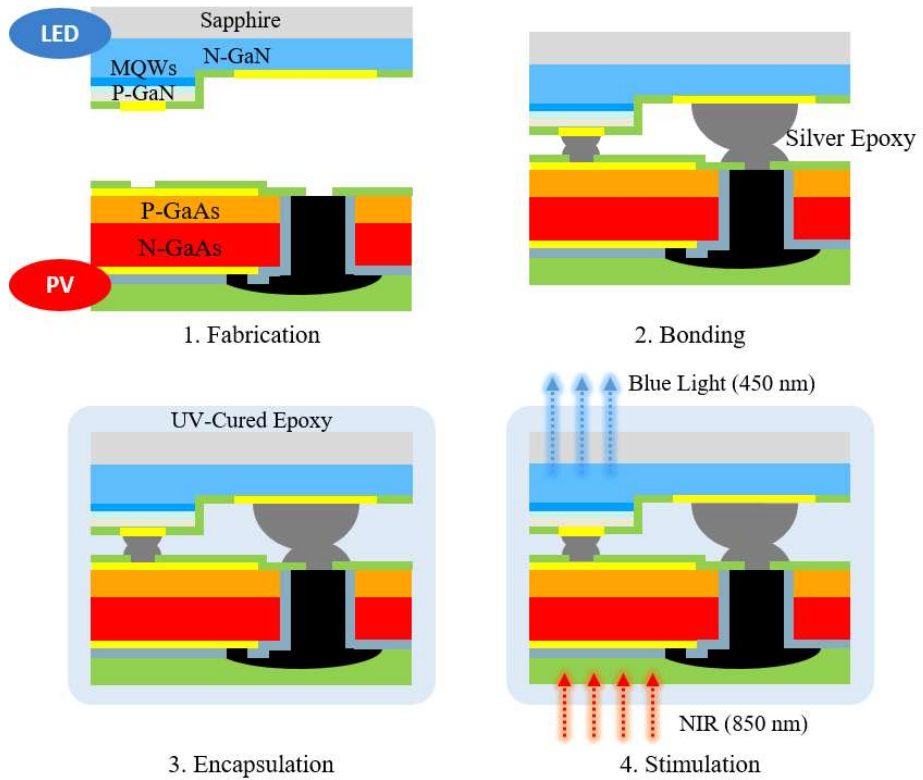


Figure 4. 3 Schematic design of the bonding of the LED to the PV cell and the light pathway through the optoelectronic neural stimulator. Incident NIR light is transmitted through the stimulator and converted to blue light.

4.2.2 Fabrication process of PV with through-hole via

4.2.2.1 Making and passivation of the deep hole of PV

For the deposition of n-contact metal, DNR-L300-30 photoresist was patterned using photolithography. Germanium of 20 nm (Ge), Ni of 50 nm and Au of 100 nm were deposited by e-beam evaporation [125]. For good ohmic contact, PV was annealed for 30 seconds at 400 °C using the rapid thermal annealing (RTA; RTA150H-SVP1, NYM TECH) method after the lift-off process.

AZ 4620 photoresist with a thickness range from 6 µm to 20 µm was used because the thickness of the photoresist must be thick to make a deep hole in GaAs substrate. AZ 4620 was spin-coated at 2000 rpm and soft-baked at 100 °C for 2 minutes. The AZ 4620 PR has a photoinitiator based on DNQ-sulphonates that requires a minimum moisture concentration during exposure for photoreaction. Therefore, it was left at room temperature for 1 hour for rehydration after soft-baking. After UV exposure, it was developed using AZ 400K developer.

After deposition of n-metal, the etched hole depth and the thickness of photoresist were measured for 4 minutes with a combination of BCl₃ and other gases to make deep holes in the GaAs substrate [126, 127]. The conditions for the three experiments are shown in table 4.1. Figure 4.4

shows the thickness of etched GaAs and PR for three conditions for 30 um and 50 um holes.

When the gas of BCl₃ & N₂ or BCL₃ was used, the etching rate of GaAs was lower than 1 μm/min. On the other hand, the presence of BCL₃ and Cl₂ showed a high value of the etching rate of GaAs above about 3 μm. On the other hand, under all conditions, the etching rate of photoresist was measured to be 0.5 μm or less. selectivity was obtained from the equation.

$$\text{Selectivity} = \frac{\text{GaAs etching rate } (\mu\text{m}/\text{min})}{\text{Photoresist etching rate } (\mu\text{m}/\text{min})}$$

When using gas of BCl₃ & N₂ or BCL₃, the selectivity was calculated to be less than 1, and the value of BCL₃ & Cl₂ was about 7.

In order to confirm the etching rates of GaAs and photoresist according to the mixing ratio of BCl₃ and Cl₂ thorns, the ICP dry etching process was performed under the conditions of table 4.2. Figure 4.5 shows the etched thickness, etch rate and selectivity of GaAs and PR according to the ratio of BCl₃ and Cl₂ ratio. As the Cl₂ increased, the etching rates of GaAs and PR increased. In particular, when the ratio of BCl₃ and Cl₂ was 1: 1, the selectivity value of 15 or more was shown in the 30 um hole etching.

Figures 4.6 and 4.7 show SEM cross-sectional images of GaAs etched

for 30 minutes under different ICP dry etching conditions using BCl_3 and Cl_2 gases. The higher the BCl_3 gas ratio, the lower the depth of the etched GaAs holes, as shown in figure 4.6. In addition, when the ratio of BCl_3 and Cl_2 is 1 to 1 when the RF power is 20 W lowered from 100W to 80W, it was confirmed that the depth of the etched hole is lowered. However, the slope of the hole is more inclined than when the RF power is 100 W. The increase in RF power did not necessarily etch the holes deeply. As shown in figure 4.7, when the ratio of BCl_3 to Cl_2 is 1 to 1 when the RF power is larger than 100W, the depth of the etched hole is lower and the hole slope is further increased. In order to etch the hole deeply, ICP dry etching was performed using gas mixed with Cl_2 (24 sccm) and BCl_3 (24 sccm) at 950 W of ICP power and 100 W of RF power for 50 minutes. The exposed holes were protected by Si_3N_4 with a thickness of 2 μm using Plasma-enhanced chemical vapor deposition (PECVD). Figure 4.8 shows SEM images after the ICP and PECVD processes. The etched hole was measured to be about 70 μm deep. The diameter of the upper hole was about 56 μm and the lower hole was about 40 μm . When Si_3N_4 was deposited by a PECVD having a target thickness of 2 μm , its thickness in the bottom and middle of the etched deep hole was approximately 1.5 μm and 1.9 μm as shown figure 4.8 (1-3). AZ 4620-thick photoresist was

patterned to expose n-meal using photolithography and Si_3N_4 was wet etched using BOE 30: 1. Figure 4.9 shows the surface image of Si_3N_4 removed by wet-etching after patterning photoresist around the hole using photolithography.



Case	Gas	Gas Flow Rate (sccm)	RF Power (W)	Source Power (w)	Pressure (mTorr)
1	BCl ₃	35	100	900	10
	N ₂	5			
2	BCl ₃	35	100	900	10
3	Cl ₂	40	75	950	10
	BCl ₃	8			

Table 4. 1 Conditions of ICP dry etching process according to different gas combinations.

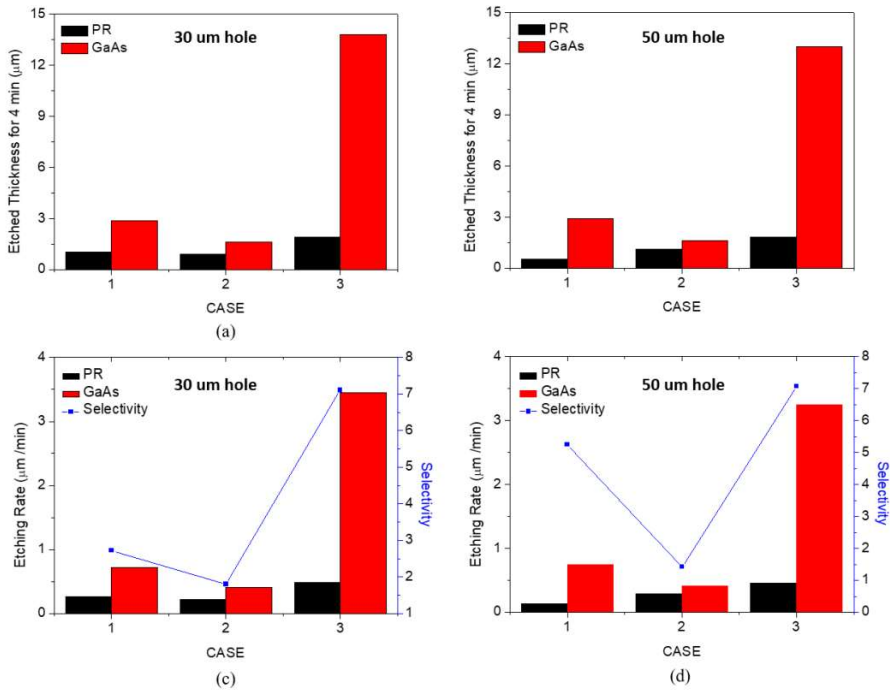


Figure 4.4 (a,b) Etched thickness of photoresist and GaAs and (c,d) etching rate of photoresist and GaAs and selectivity in 30 μm and 50 μm hole sizes after ICP dry etching for 4 min according to different gas combinations.

Case	Gas	Gas Flow Rate (sccm)	RF Power (W)	Source Power (w)	Pressure (mTorr)
1	Cl ₂	40	75	950	10
	BCl ₃	8			
2	Cl ₂	24	75	950	10
	BCl ₃	24			
3	Cl ₂	8	75	950	10
	BCl ₃	40			

Table 4. 2 Conditions of ICP dry etching process according to the gas ratio of Cl₂ and BCl₃.

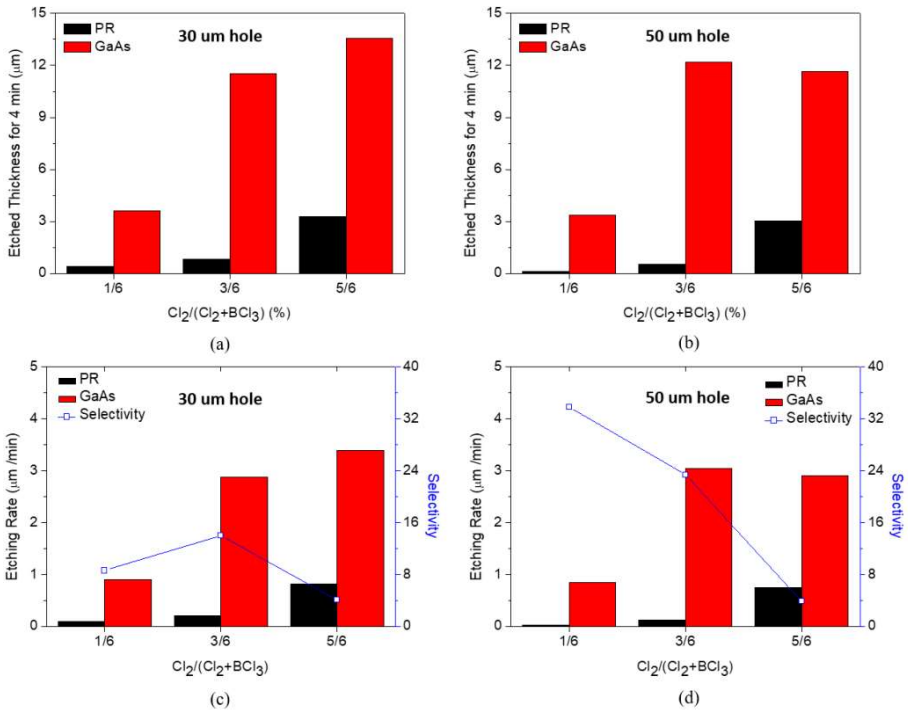


Figure 4.5 (a,b) Etched thickness of photoresist and GaAs and (c,d) etching rate of photoresist and GaAs and selectivity in 30 μm and 50 μm hole sizes after ICP dry etching for 4 min according to the gas ratio of Cl_2 and BCl_3 .

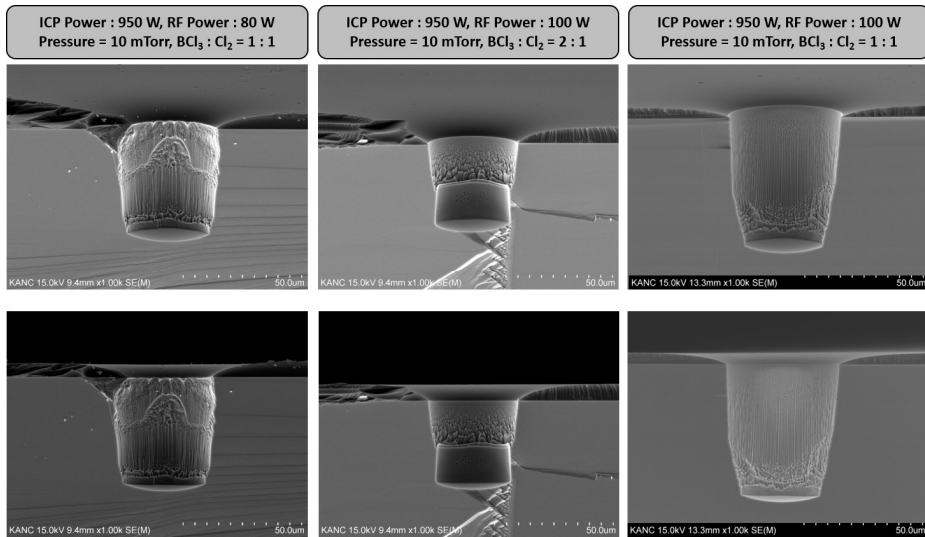


Figure 4. 6 Cross-section image of SEM after ICP dry etching for 30 minutes under different process conditions using BCl_3 and Cl_2 gas.

If the BCl_3 gas ratio is higher than Cl_2 , it shows a lower etching of GaAs than when the BCl_3 and Cl_2 gas ratio is 1 to 1 shown as in the middle and right column figures. In addition, in the case of RF power of 100 W, GaAs was etched more than 80 W, and the slope of the hole was tilted more when the BCl_3 and Cl_2 gas ratio is 1 to 1 shown as in the left and right column figures.

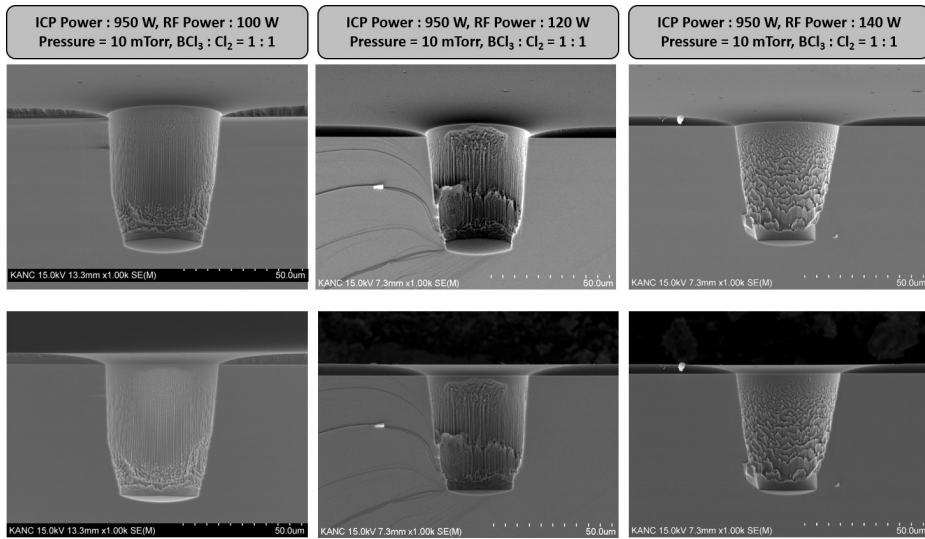


Figure 4. 7 Cross-section image of SEM after ICP dry etching for 30 minutes according to RF power when the BCl₃ and Cl₂ gas ratio is 1 to 1.

The more RF power increased by more than 100W, the less etched GaAs depth was reduced, and the slope of the hole became larger.

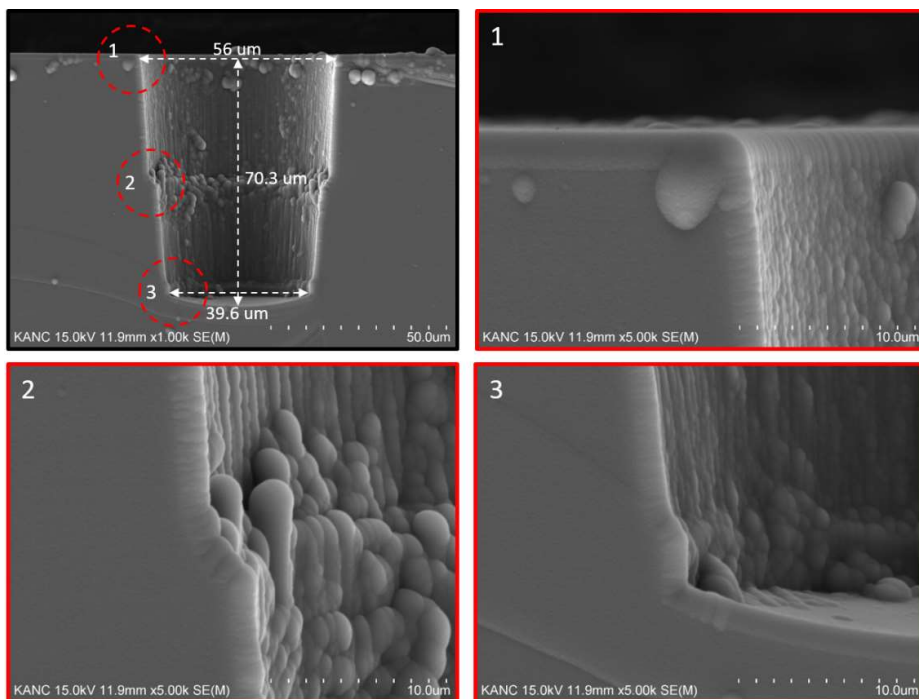


Figure 4. 8 Cross-section image of SEM of the etched and passivated hole of GaAs after ICP dry etching for 50 min and PECVD process for deposition of Si_3N_4 .

After an ICP dry etching for 50 minutes, the depth of the GaAs hole was measured at about 70 μm . The diameter of the etched hole at the top and bottom positions was measured about 56 μm and 40 μm respectively as the shown upper left figure. The figures (top right, bottom left, bottom right) show the image of Si_3N_4 deposited in the position shown in the upper left figure.

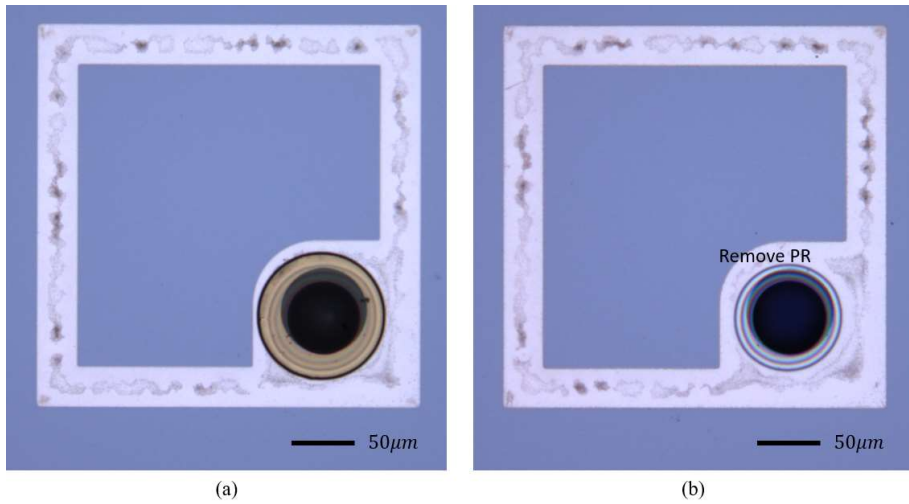


Figure 4. 9 Surface image of (a) photoresist patterned for patterning SiN after PECVD process using photolithography and (b) Si₃N₄ patterned after wet-etching SiN and removing photoresist.

4.2.2.2 Ink-jet printing to fill the hole with metal

Inkjet printing is a method of direct patterning using metal ink [128-132]. The inkjet printing method was used to fill the metal in the etched deep hole. Korea Institute of Industrial Technology (KITECH) used prototype inkjet equipment and used ink is low-temperature sintering ink (ANP, DGP 40LT-15C).

The volume of the etched hole has about 130 picolitres. When printing inkjet, a drop of silver ink is known as about 10 picolitres. The solid content of the cold sintering ink used is about 30% to 35%, and when calculated by volume, it is about 0.4 picolitre. That is, about 325 drops of silver ink must be filled into the hole, but if you drop 20 drops because of the volume of the ink, the ink will spread out of the hole as shown in figure 4.10. To prevent overflow of ink out of the hole, FC film was coated and patterned around the hole. FC film is a 1:4 mix of FC722 and FC40 and the surface energy is low in the coated area to prevent the ink from spreading. The contact angle value for water on the glass substrate was measured at about 77 degrees before the FC film coating, and after the coating, the surface energy was reduced and the surface energy turned into hydrophobic as shown in figure 4.11.

In order to pattern FC film, the holes and around the holes were

patterned using the photolithography method using AZ 4602 photoresist shown as figure 4.12 (a). After the photoresist pattern, the FC film solution was spin-coated to 3000 rpm, annealing at 100 degrees for 10 minutes, and then removing the PR using acetone. Figure 4.12 (b) shows an FC film pattern in areas other than the holes and around the holes.

After the FC film pattern, silver ink filled the hole with silver ink using a single drop and multi-drop method. The single drop method was filled with silver ink every minute and sintered every 30 drops. The multi-drop method filled the hole with silver ink 50 drops at a time. When printing inkjet, the substrate's temperature was fixed at 50 degrees and all sintering conditions were carried out at 150 degrees for 30 minutes. In the case of multi-drops, a total of 350 drops of silver ink, 50 drops, were filled into the hole, leaving the hole empty and bulging out of the hole as shown in figure 4.13. As the number of drops increased after sintering with sintering in the open, the sinter failed to fill the hole and hardened outside. To prevent this problem, the sintering was carried out for 30 minutes at a temperature of 150 degrees at a vacuum of 25 mTorr. As a result, the silvers around the hall were broken, although they were not empty unlike the convection oven as shown in figure 4.14.

When the silver ink is filled into the hole by a single drop, the silver

ink becomes dry for one minute and even if it is filled by a total of 30 drops, it does not overflow out of the hole. Silver ink did not overflow out of the hole and began to overflow out of the hole when 240 drops were filled until 30 drops of silver ink were filled and cleaned and seven more times. A total of 300 drops of silver ink were filled in the hole by single drop and 30 drops were dropped by multi-drop for contact with silver ink and n-metal. Figure 4.15 shows the surface SEM image according to the number of drops. Also, unlike the multi-drop method, the sintered silver was not empty and no crack was found around the hole. Figure 4.16 shows a cross-sectional image after sintering with 300 drops of silver ink in a single drop method.

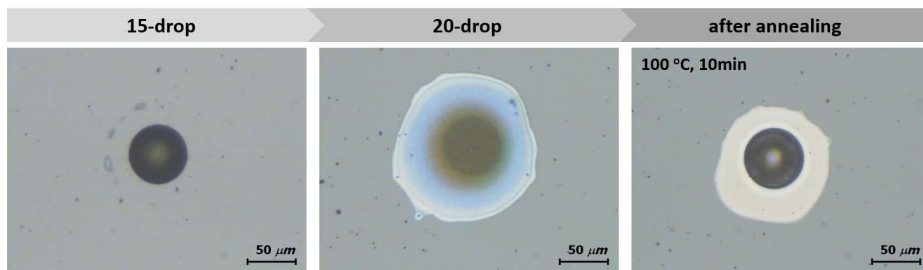


Figure 4. 10 Surface image according to the number of silver ink drops in the etched deep hole.

If 15 drops of silver ink are dropped in the etched deep hole, it will not overflow, but 20 drops of it were dropped, it will start to overflow.

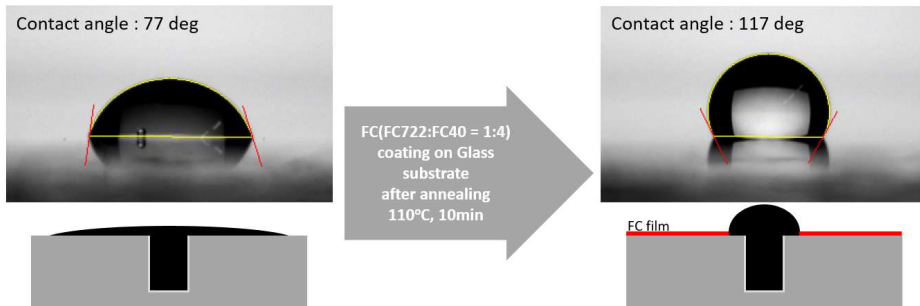


Figure 4. 11 Contact image for water on a glass substrate before and after FC film coating.

The surface energy changes to hydrophobic because the surface edge of the glass substrate becomes low after FC film coating. FC film around the hole prevents silver inks from overflowing around the hole.

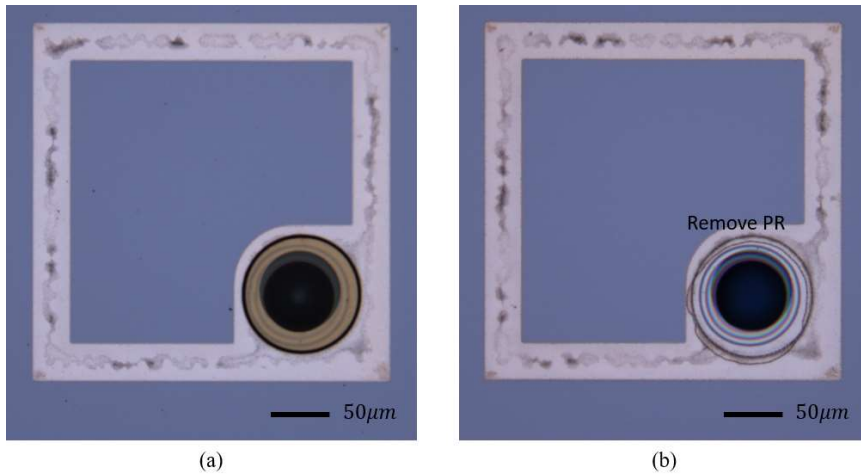
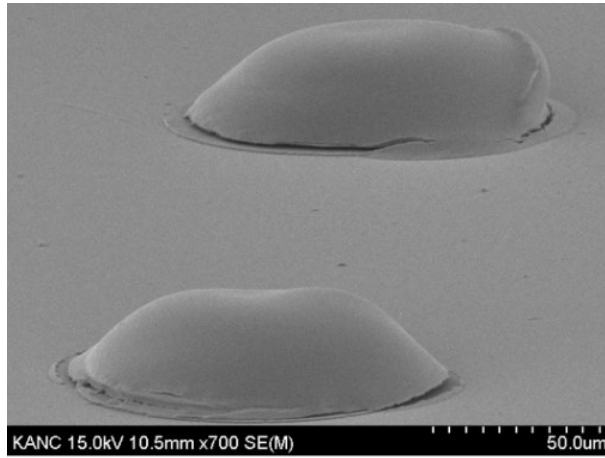
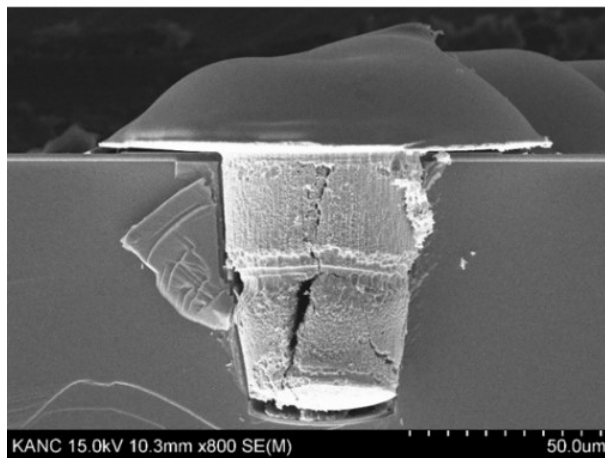


Figure 4. 12 Surface optical image of (a) photoresist patterned PV substrate around the deep hole and the inside of hole before FC film coating and (b) photoresist removed PV substrate after FC film coating.

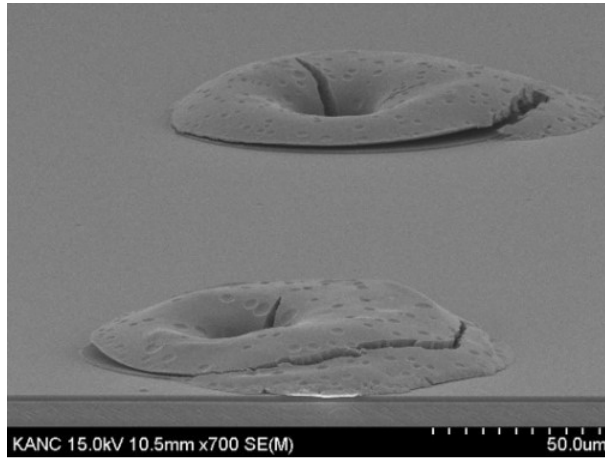


(a)

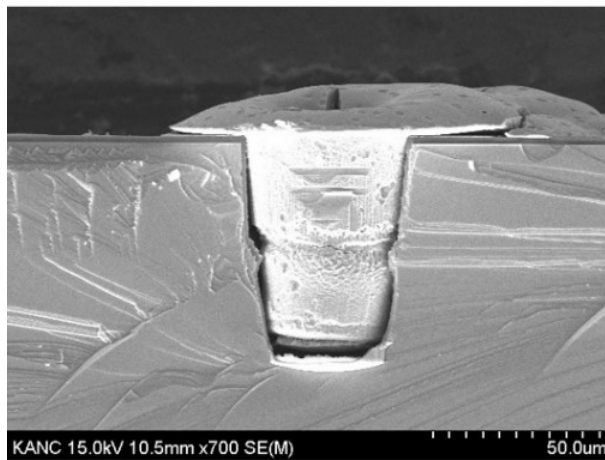


(b)

Figure 4. 13 SEM (a) surface and (b) cross-section image when filling up 300 drops of silver inks in the deep hole by multi-drop method using inkjet printing and sintered in a convection oven at a temperature of 150 °C.



(a)



(b)

Figure 4. 14 SEM (a) surface and (b) cross-section image when filling up 350 drops of silver inks in the deep hole by multi-drop method using inkjet printing and sintered in vacuum hot plate oven at a temperature of 150 °C and a vacuum of 25 mTorr.

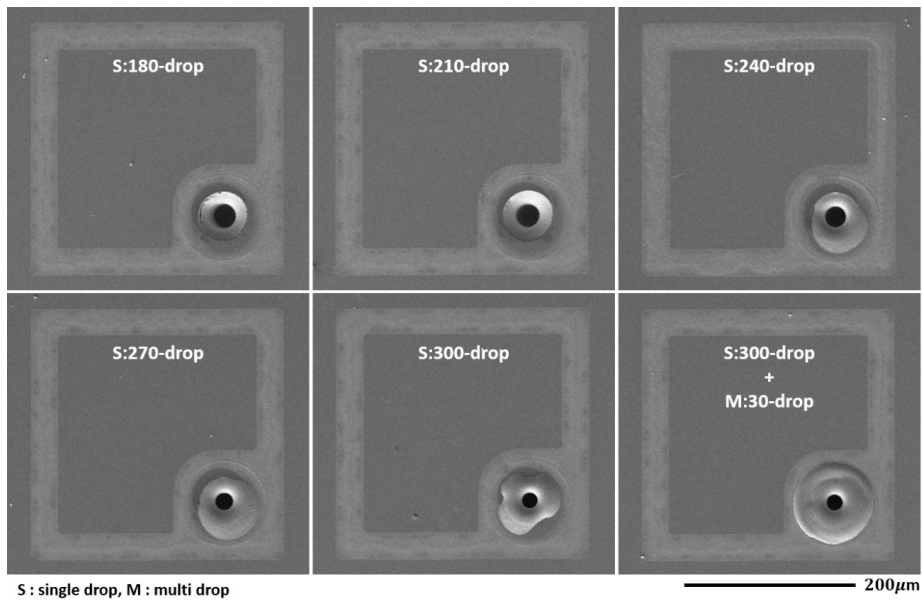
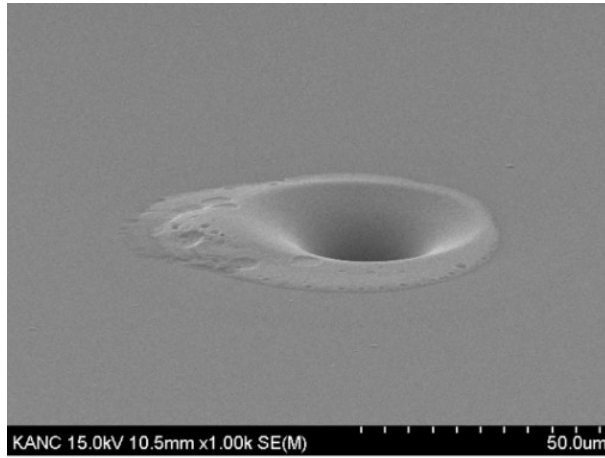
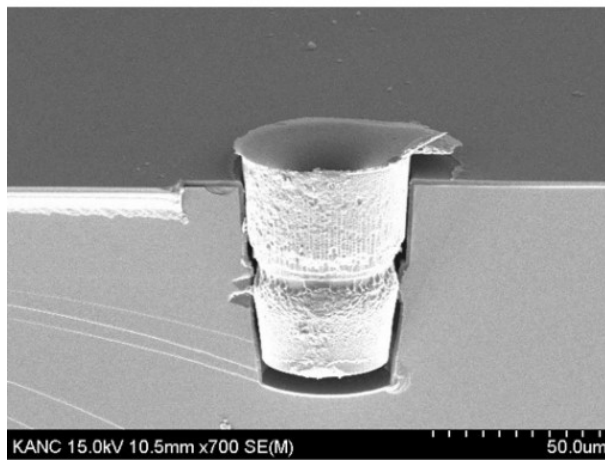


Figure 4. 15 SEM surface image according to drop count when silver ink is filled in the deep hole by single drop method.



(a)



(b)

Figure 4. 16 SEM (a) surface and (b) cross-section image when filling up 300 drops of silver inks in the deep hole by a single-drop method using inkjet printing and sintered in a convection oven at a temperature of 150 °C.

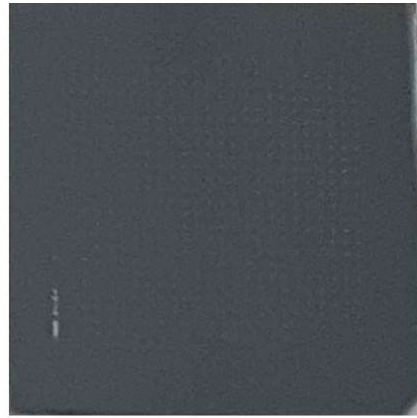
4.2.2.3 Lamination & Lapping

GaAs' hardness is about 6 GPa which is about half the value of Si substrate 12 GPa. Expose the etched deep hole to the backside through the loading. At this time, the GaAs substrate is very thin, with a thickness of about 50 μm , so you need lamination to proceed with the back process. In addition, the lamination material has the following conditions: 1. It must not be dissolved or separated from the solvent used in the back process. 2. It must remain uncoupled at SU8 hard baking temperature above 150 °C. 3. It should be easy to detach the device after dicing. With these conditions, lamination was carried out in various ways using substances used in ordinary laboratories. A simple method was used to laminate the solution using photoresist, which is easily melted in the acetone, and Polydimethylsiloxane (PDMS), which is highly resistant to solvent. First of all, we applied a spin coating of AZ4330 photoresist on the glass substrate and then we applied baking. Then, the photoresist on the edge of the substrate was removed. Mix sylgard 184 base and curing agent with 10:1 on a board coated with photoresist and cover the photoresist with a spin coating. Before curing the PDMS on the glass substrate, the glass substrate and PV substrate on the holesless side were bonded. PV substrate laminated using PDMS and photoresist was lapped

using multiprep polishing system (Allied High Tech). PV substrate with a thickness of about 650 μm was lapped to reduce the thickness to 50 μm , but many cracks were shown as shown in figure 4.17 (a) due to the elasticity of PDMS. To get rid of the crack, hard lamination materials were required. To solve this problem, aluminum was deposited 300 nm on top of the glass substrate and SU8 2015 photoresist was spin-coated on it at 2000 rpm. Then, the PV substrate was bonded with a glass substrate and lapped using multiprep polishing system (Allied High Tech). The glass substrate with PV bonded was waxed and lapped until the hole was exposed using 3 μm diamond lapping film. Then, a silica powder was used to polishing the surface to make it smooth. Figure 4.17 (b) shows the surface image of the PV cell after lapping until the hole is exposed.



(a)



(b)

Figure 4. 17 Surface image of PV cell laminated using (a) elastomer and (b) hard material after the lapping process.

4.2.2.4 Back-side process & Dicing

The DNR-L300-30 photoresist was patterned using a photolithography method for the deposition of p-contact metals. Ti of 10 nm and Au of 100 nm were deposited on the backside of PV substrate laminated on glass using E-beam evaporation (ULTECH) for p-contact. The SU8-2005 was used after the lift-off process to create a layer of protection using photolithography. After the backside fabrication process, the PV substrate was separated into a $300\ \mu\text{m} \times 300\ \mu\text{m}$ size. PV substrate with lamination is very thin and fragile when separated, so dicing was performed while laminated. Also, if the PV is removed using the dicing saw, it is dangerous to break it by physical force, so it was separated through dry etching.

ICP dry etching was used to remove PV for separating elements and RIE dry etching was used to remove SU8 used as lamination material. First, aluminum was deposited 100 nm to protect the passive layer using an E-beam evaporator during RIE dry etching. Then, the pattern was used to separate PV into $300\ \mu\text{m} \times 300\ \mu\text{m}$ size using AZ4620 thick photoresist for ICP. ICP(Oxford instruments, PlasmaPro System100 Cobra) dry etching was performed using gas mixed with Cl_2 (24 sccm) and BCl_3 (24 sccm) at 950 W power for 40 min. After the PV substrate

was separated into $300\ \mu\text{m} \times 300\ \mu\text{m}$, RIE dry etching was used to remove the lamination substance SU8. RIE dry etching (ALL FOR SYSTEM, AFS-R4T RIE SYSTEM) was performed using O_2 gas (20 sccm) at 100 W until SU8 is removed. Finally, in order to separate PV cells from the glass, it was immersed in a 300 MIF developer to dissolve aluminum. Numerous PV cells with through-hole via were separated from the glass and washed sufficiently with DI water. Figure 4.18 shows the process schematic diagram of the PV cell with through-hole via.

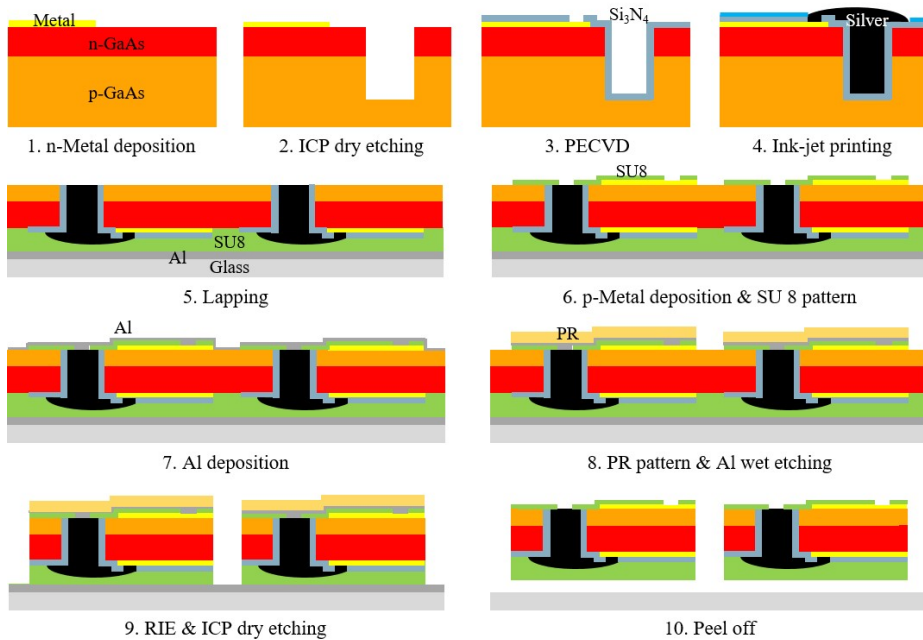


Figure 4.18 Schematic illustration of the fabrication process of PV.

The n-metal of the PV cell is composed of Ge/Ni/Au (20/50/100 nm). ICP dry etching process makes holes about 70 μ m deep. Si₃N₄ passivation layer is deposited on the etched hole surface by PECVD and silver inks are filled into the deep hole using ink-jet printing. The hole is exposed on the backside by a lapping process. Ti/Au (10/100 nm) for p-metal is deposited on the back-side of PV cells and they are protected by the SU8 layer. Al and PR are patterned to protect PV during etching. The PV cells are separated through ICP and RIE processes and peel off.

4.2.3 LED fabrication process

The micro-LED fabrication process is illustrated in figure 4.19. To make ohmic contact, the indium tin oxide (ITO) was deposited on the LED substrate using E-beam evaporation (ULTECH) and then an LED substrate with ITO at 550 °C for 3 minutes using RTA (RTA150H-SVP1, NYM TECH) [133]. The AZ4330 photo registry was patterned using photolithography for ICP dry etching. ICP dry etching was performed using gas mixed with Cl₂ (30 sccm) and BCl₃ (5 sccm) at 800W power (Multiple ICP, STS) [134, 135]. The etching rate of ITO and GaN are about 32 nm/min and about 360 nm/min respectively. After 12 minutes of etching the LED substrate using ICP dry etching, the DNR-L300-30 photoresist was patterned using photolithography for deposition of n-contact metal. Ti / Al / Ni / Au (30 / 100 / 30 / 100 nm) was deposited by e-beam evaporation (ULTECH) and the pattern was formed by the lift-off method [136]. Finally, the SU8-2005 was used to create a layer of protection using photolithography. The lapping process was performed to reduce the thickness of the LED substrate to less than 200 μm because LEDs have 420 μm thick sapphire substrates. The lapping process was used by multi-prep polishing systems (Allied High Tech) with a 3 μm diamond-lapping film. To separate individual elements in a 300 x 300

μm^2 size, the dicing process was performed using the Automatic Dicing Saw machine (DAD3350, Disco) with a diamond blade 200 μm thick.

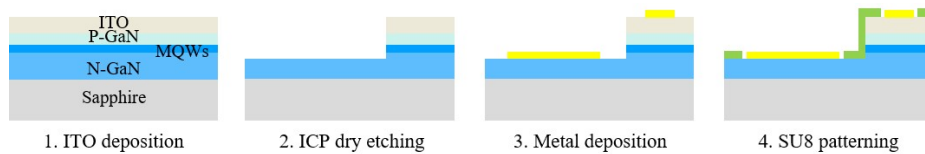


Figure 4. 19 Schematic illustration of the fabrication process of LED.

ITO is deposited on the LED substrate to make an ohmic contact. The LED is etched $2.1 \mu\text{m}$ by ICP dry etching. Ti/Al/Ni/Au (30/100/30/100 nm) for n-metal and p-metal are deposited by e-beam evaporation. All surface area of LED except pad is protected by SU 8.

4.2.4 Integration PV and LED

In order to integrate micro LEDs and PV cell, epoxy (MGchemicals, 8331S) was used to have high electrical conductivity and a suitable viscosity. Silver epoxy was placed on the n- and p- metal pads of the opaque PV cell. Micro LED is designed to be transparent, allowing them to be combined with opaque PV cells in the right place.

After bonding the micro-LED and PV cell, the stimulator combined with them was passivated with a transparent UV-cured epoxy (NOA68, Norland) from NIR and blue light to protect the device and electrolyte. The UV-cured epoxy was exposed for one hour using UV-LED with 365 nm of wavelength for 1 hour to fully cure epoxy.

4.2.5 Light source and measurement

To evaluate the characteristics of PV, a NIR light source is provided using the TO-18 Type 850 nm Laser Diode (LD) (QSI, QL85R6SX). Laser diode controllers (THORLAB, LDC 205 C) and temperature control laser diode mount (THORLAB, TCLDM9) were used to inject current into the laser diode and prevent excessive heat generation. Due to the aspect ratio of light irradiated from LD, two cylindrical lenses with a focal distance of 39mm and 10mm with axes aligned vertically to each

other were used. After passing through the cylindrical lens, the NIR rays were combined to a fiber optic 62.5 μm in diameter using a spherical lens. Field luminous spectra of LD and LEDs were captured using iHR-320 spectrometer (HORIBA). The power of the light output was measured by the Newport 1928 power meter. The electrical properties of PV and LEDs were investigated using the KEITHLEY 2425 source meter and MS Tech probe station. Figure 4.20 shows a schematic diagram and an actual image of the optical settings.

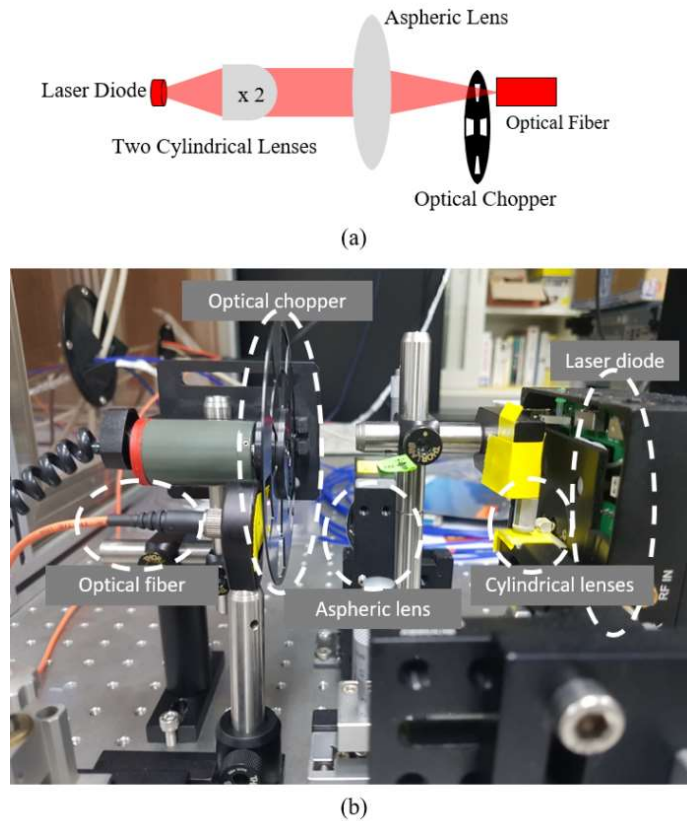


Figure 4. 20 (a) Schematic illustration and (b) actual image of the optical setup.

The NIR light emitted from a laser diode is collimated by two cylindrical lenses. After passing through the cylindrical lens, the NIR light was coupled to an optical fiber with an aspheric lens. The chopper between the aspheric lens and the optical fiber can control the duration of light emission.

4.2.6 HEK cell culture and ChR2 expression for in vitro electrophysiology experiment

HEK293 cells were cultured in T25 tissue culturing flasks (SPL). Dulbecco's Modified Eagle medium 10% FBS (Gibco), 1% penicillin/streptomycin (Invitrogen) was used between 50% and 80% confluence. Adherent cells were transfected with a complex of Lipofectaine2000 (Invitrogen) and pcDNA3.1-hChR2-EYFP (Addgene) plasmids within 12 to 24 hours in the culturing media. Transfection complexes were made by adding 2.7 μg of DNA plasmid. Fluorescence microscopy (Nikon Ti-U) was used to verify the expression of the ChR2-EYFP protein in HEK293 cells. After fixation of hChR2-EYFP expressed HEK 293 cells with 4% paraformaldehyde, fluorescence images were acquired with confocal laser scanning microscope systems (Zeiss LSM700 at GBSA) equipped with 60x water immersion objective lenses. For electrophysiology recording of ChR2-expressed HEK293 cells with the PV-LED stimulator, the cells were plated at about 20-30% confluence on glass coverslips coated with poly-L-lysine (Sigma Aldrich). Whole-cell patch-clamp experiments were conducted within 3 to 12 hours after being seeded on coverslips.

4.2.7 Neuron cell culture and ChR2 Expression for in vitro electrophysiology experiment

Mammalian primary hippocampal neurons were cultured with dissected embryonic hippocampi of prenatal day 18 Sprague-Dawley rats (Koatech: SPF laboratory animal company). The tissues were treated with trypsin in HBSS dissecting medium and triturated with fire-polished pasture pipette in order to dissociate hippocampal tissues into single neurons. About 13,000 neurons were seeded on poly-L-lysine coated coverslips in 12 well plates with DMEM containing 10% FBS (Gibco) and 1% penicillin/streptomycin (Invitrogen) for 3 hours at 37 °C in 5% CO₂ incubator. All of the DMEM media was suctioned out of each well and neurobasal medium including 2% B27 supplement and 0.25% GlutaMax were added for culturing neurons for the next 3-weeks. Lentivirus was packaged in order to express ChR2 opsins in primary cultured neurons. Transfer vector pLenti-Synapsin1-hChR2 (H134R)-EYFP-WPRE (Addgene), envelop vector pMD2.G (Addgene) and packaging vector psPAX2 (Addgene) were triple co-transfected to 293FT cells (Invitrogen) using a transfecting reagent Lipofectamine 2000 (Invitrogen). On the next day, the medium containing DNA-Lipofectamine complexes were aspirated and fresh complete DMEM

medium without antibiotics was added. The transfected cells were incubated for 72 hours back in the incubator. hChR2-EYFP packaged lentiviruses soups were centrifuged for harvesting at 2,000g for 15 minutes at 4°C from the supernatant medium of transfected 293FT cells. For expressing ChR2 opsins Lentivirus containing hChR2-EYFP genes were added to primary cultured neurons and incubated at 37 °C in 5% CO₂ incubator for 7 days. The expression of the ChR2-EYFP protein was verified by fluorescence microscopy (Nikon Ti-U). After fixation of hChR2-EYFP expressed primary cultured neurons with 4% paraformaldehyde, fluorescence images were taken with confocal laser scanning microscope systems (Zeiss LSM700 at GBSA) equipped with 60x water immersion objective lenses. The animal sacrifice for primary neural culturing was approved by the Institutional Animal Care and Use Committee (IACUC) of Seoul National University (SNU-190813-2).

4.2.8 Whole-cell patch-clamp

To test the optical and functional capability of the PV-LED stimulator, a whole-cell patch-clamp experiment was conducted to stimulate ChR2 proteins expressed in HEK293 cells and neurons. HEK293 cells and neurons were bathed in extracellular solution containing 150 mM NaCl,

4 mM KCl, 1 mM MgCl₂, 2 mM CaCl₂, 5 mM glucose, and 5 mM HEPES (pH7.4) at room temperature. Internal solution containing 120 mM K-aspartate, 4 mM NaCl, 4 mM MgCl₂, 1 mM CaCl₂, 10 mM EGTA, 3 mM Na₂ATP, and 5 mM HEPES (pH 7.2) was filled into a patch pipette. Fig. 4 (b) shows the schematic illustration of the optogenetic stimulation setup. The distance between the cell and the device was about 800 μm due to the interference of the patch pipette. Whole-cell patch-clamp recordings were performed using a Multiclamp 700B amplifier, Digidata 1440 digitizer, a PC operating pClamp10 (Molecular Devices). A truncated optical fiber cable coupled to the 850 nm LD was mounted on the XYZ stage holder of a micro-manipulator. Stimulation experiments were performed according to NIR power by fixing PV at the end of optical fiber. The duration of blue light emission was controlled by modulating the 850 nm LD by an optical chopper. Figure 4.21 shows the schematic illustration of the optogenetics stimulation setup using patch-clamp.

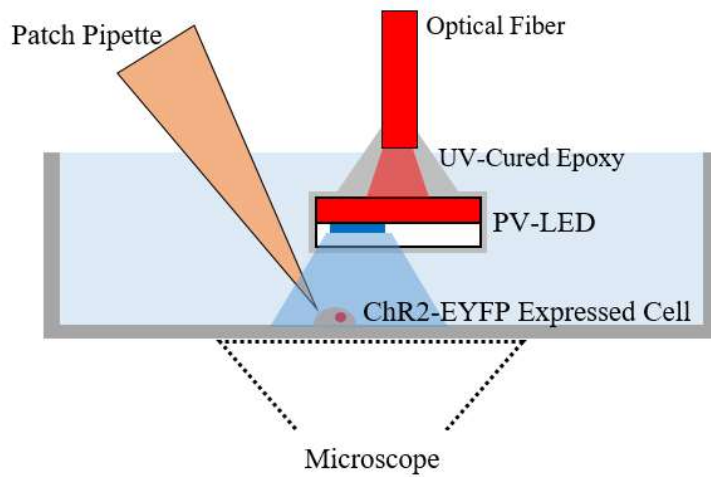


Figure 4. 21 Schematic illustration of the optogenetics stimulation setup.

The PV-LED stimulator and optical fiber were fixed by UV-cured epoxy. The interference between the patch pipette and the PV-LED stimulator causes the distance between the cell and the stimulator to be about 800 μm .

4.3 Results

4.3.1 The characterization of PV

Figure 4.22 (a) shows the back image and the characteristics of the PV cell and the back of the PV cell after the fabrication process. Relative efficiency was characterized by measuring the electrical output power of a PV cell under lighting by various wavelengths of 600 nm to 1000 nm using monochromator. PV cells appear to have a higher absorption for NIR light (840 to 880 nm) compared to other wavelengths, as shown in figure 4.22 (b).

Figure 4.22 (c) shows the current-voltage characteristics of the PV cell under various NIR input power conditions of from 0 mW to 18 mW. The power generated by the PV cell can be easily calculated with an I-V sweep by the $P=IV$ formula. the Short circuit current (I_{SC}) represents the maximum current transmitted through a PV cell corresponding to a short circuit condition when the impedance is low. This condition occurs at the start of the sweep when the voltage is zero. The ideal cell is the total current produced by the photon by the PV. Open circuit voltage (V_{OC}) is the maximum voltage difference across the cell and occurs when there is no current transmitted through the cell. At the I_S and V_{OC} points, the power becomes zero and the maximum value for power occurs between

the two. At the maximum current point, the voltage and current are specified as V_{MP} and I_{MP} respectively. The following equation refers to the expression to find a fill factor.

$$\text{Fill factor} = \frac{P_{MAX}}{P_T} = \frac{I_{MP} \cdot V_{MP}}{I_{SC} \cdot V_{OC}}$$

At 6 mW of NIR power, PV cells had a peak efficiency of 34.6% and the fill factor was approximately 0.85 as shown in figure 4.22 (d). The short circuit current is 795 μ A and open circuit voltage is 3.064 V at 6 mW NIR power.

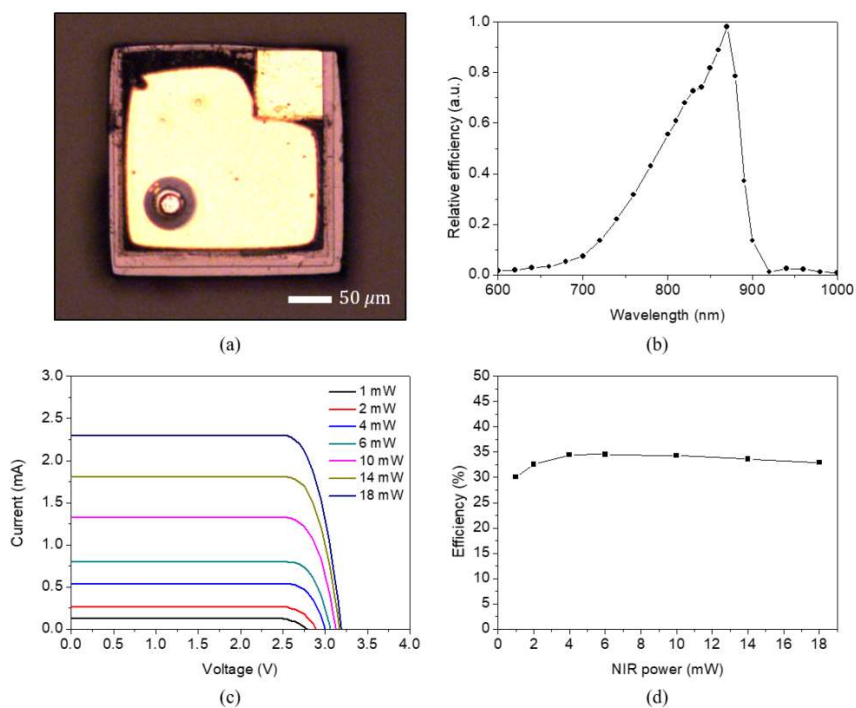


Figure 4. 22 Optical images of (a) back-side of the PV cell. (b) Relative efficiency according to wavelength 600 1000 nm; the largest efficiency between 830~850 nm. (c) Voltage-Current characteristics and (d) Fill factor and Efficiency of PV cell; the PV cell has a fill factor of 0.85 and an efficiency of 34.6% under 850 nm illumination at 6 mW.

4.3.2 The characterization of LED

Figure 4.23 shows the image and characteristics of LEDs with a $60 \times 60 \mu\text{m}^2$ emission area after the fabrication process. The peak wavelength of the spectrum of blue light emitted by micro LEDs was found to be 449.2 nm as shown in figure 4.24(b), which is suitable for the stimulation of CHR2- expression cells. Figure 4.24 (c) shows the current-voltage-power characteristic. The turn-on voltage of the micro-LED was measured to 2.4 volts.

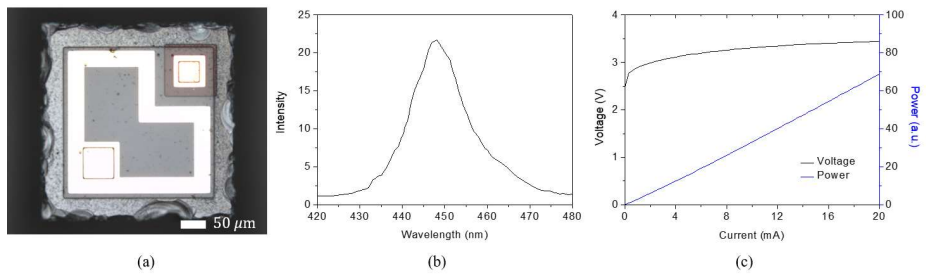


Figure 4. 23 (a) Optical image of LED after dicing. (b) Spectrum of light emitted from the LED, the peak wavelength is 449.2 nm. (c) Current-voltage-power characteristics of LED. The turn-on-voltage of the LED is 2.4 V.

4.3.3 Optoelectronic neural stimulator

The simulator combined with PV cell and micro-LED emits blue light by the NIR from the optical fiber as shown in figure 4.24. Figure 4.25 shows the emission image of blue light measured by CCD at the same exposure time depending on the distance from the PV-LED stimulator. When closest to the stimulator, the diameter of the light was measured at about $100\ \mu\text{m}$. This size is larger than $60\ \mu\text{m} \times 60\ \mu\text{m}$, which is the luminous size of the micro-LED and has become bigger due to the sapphire thickness of the micro-LED. As the distance from the PV-LED stimulator increased, the intensity of light became dramatically weaker and the size of the light gradually increased. Figure 4.26 shows the emission image of blue light measured by CCD at the auto-exposure time depending on the distance from the PV-LED stimulator. Figure 4.27 shows the intensity line profile of the emission of PV-LED stimulator obtained by the CCD image at 2mW of NIR power.

Figure 4.28 (a) shows the output power and efficiency of the PV-LED stimulator depending on NIR power. As NIR power increases, the emission output power of the PV-LED stimulator also increases linearly. The maximum efficiency was measured at around 8% at 1 mW of NIR power and gradually decreased as NIR power was increased. At NIR

power of 10 mW, the efficiency was measured at about 4.4%.

In order to obtain the average intensity of emission light of PV-LED stimulator, the information of the light obtained in figure 4.26 and the emission power of the light obtained in figure 4.28 (a) were used. Image J software was used to match the intensity of light per pixel. Figure 4.28 (b) shows the intensity of the light emitted by the PV-LED stimulator and the line profile of the NIR power at 0 mm distance and 2 mW. The emission intensity of the PV-LED stimulator, when closest to the device, was approximately 2.7 mW/mm^2 at NIR power of 1 mW. This suggests that the required light intensity for the spike is known to be about 1 mW/mm^2 and therefore sufficient to stimulate the ChR2-expressed neuron even below 1 mW of NIR [137-140].

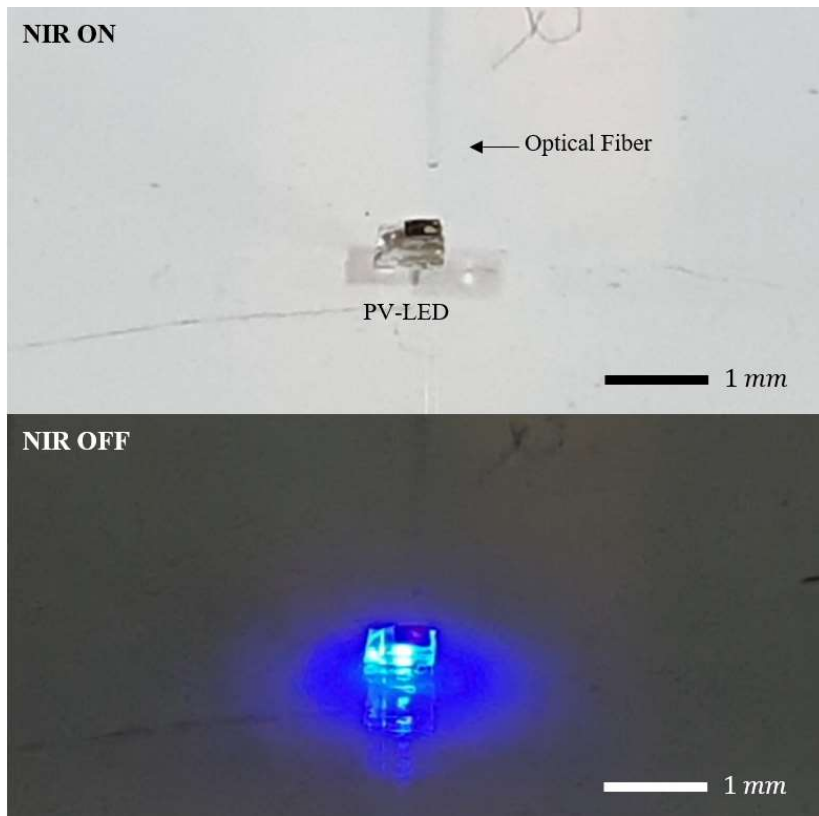


Figure 4. 24 Operating image of optoelectronic neural stimulator combined with PV cell and micro-LED by the NIR from the optical fiber.

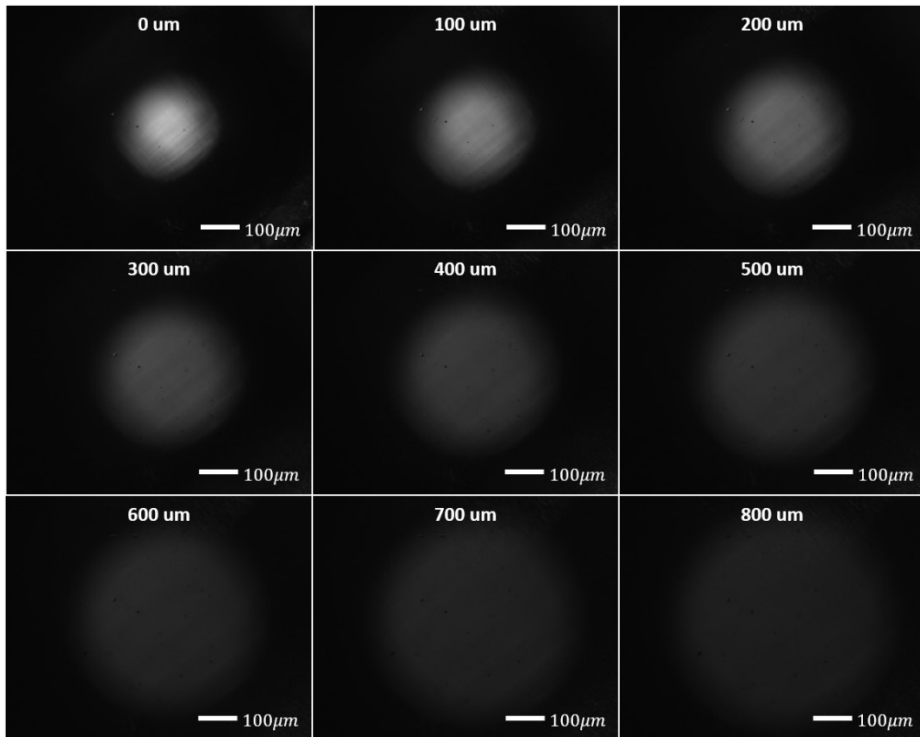


Figure 4. 25 Size of the light spot according to distance from the PV-LED stimulator at the same exposure time of the CCD.

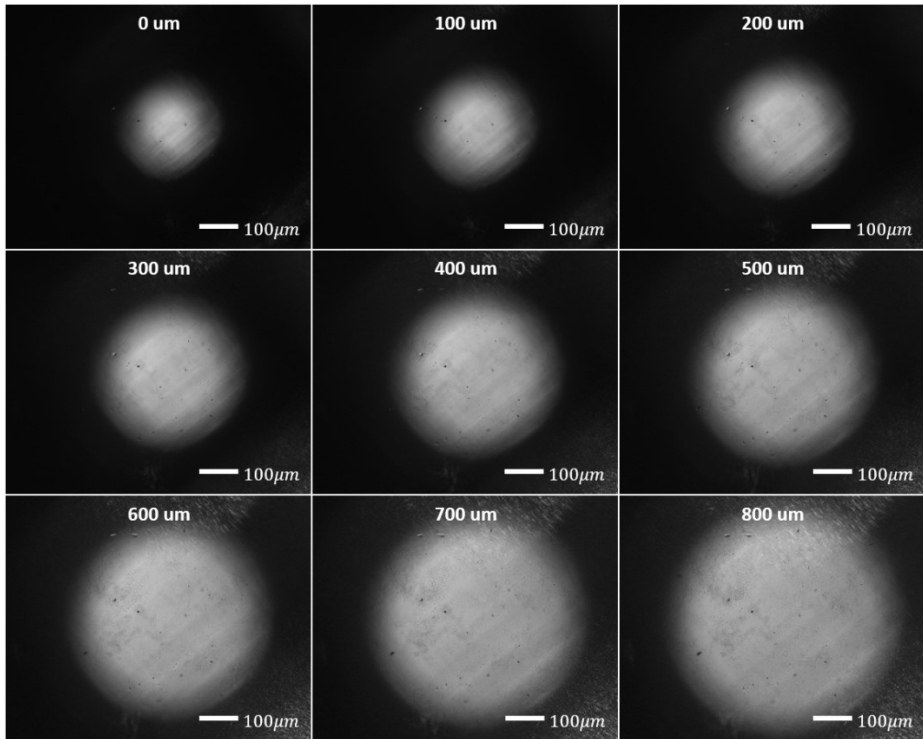


Figure 4. 26 Size of the light spot according to distance from the PV-LED stimulator at the automatic exposure time of the CCD.

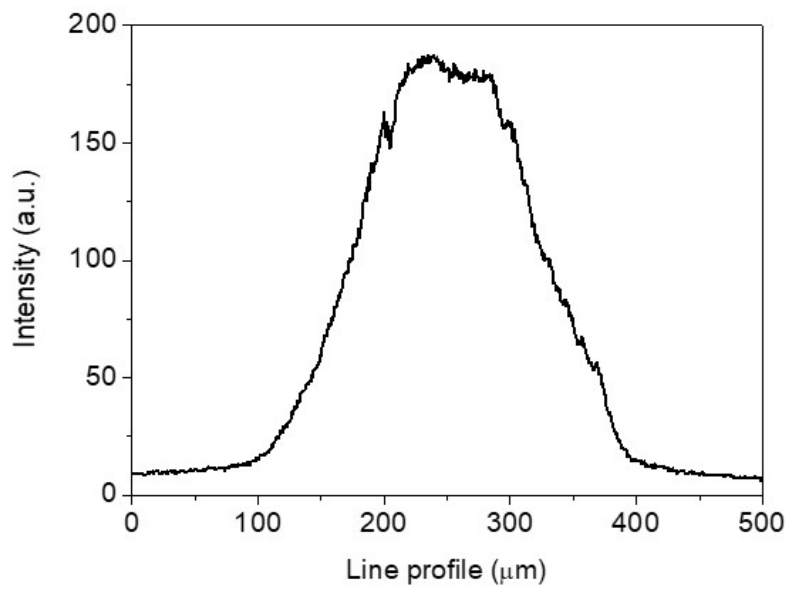
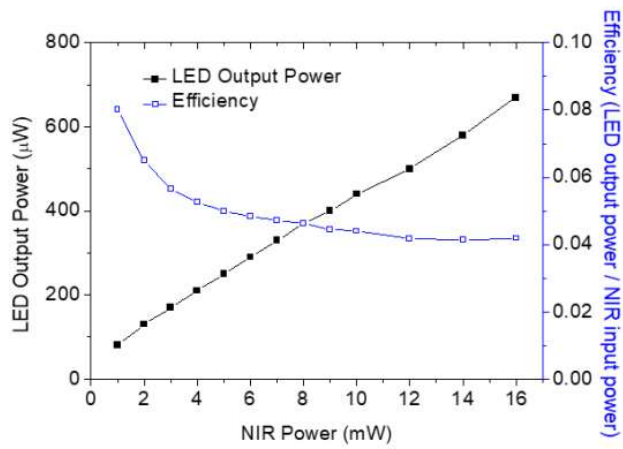
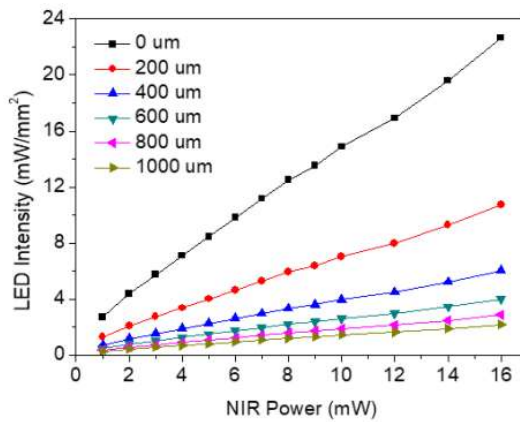


Figure 4. 27 Intensity line profile of emission of PV-LED stimulator obtained by the CCD image at 2mW of NIR power.



(a)



(b)

Figure 4. 28 Characteristics of the PV-LED device. (a) LED output power, Efficiency and (b) LED intensity according to NIR power.

The efficiency was measured to be about 8% at 1 mW of NIR power. The emission intensity of PV-LED stimulator when closest to the device was about 2.7 mW/mm² at 1 mW of NIR power.

4.3.4 In-vitro experiment

4.3.4.1 HEK cell

The expression of ChR2-EYFP had to be verified to perform ChR2 electrophysiology experiments. Under the confocal laser scanning microscope (Carl Zeiss LSM 700), the fluorescence of EYFP was detected as shown in figure 4.29. In particular, ChR2, a blue photosensitive membrane protein-tagged as EYFP, is well represented in the membrane area and inside the HEK293 cells.

In order to obtain the recording form of the whole-cell voltage-clamp of ChR2-EYFP expressed HEK293 cell, the blue light of PV-LED stimulator was exposed for 300 ms at different NIR power from 0 to 16 mW that that mean intensity range of blue light of the PV-LED stimulator is from 0 mW/mm² to 2.86/mm². Figure 4.30 shows the recording form and photocurrent of the whole-cell voltage-clamp of ChR2-EYFP expressed HEK293 stimulated by PV-LED stimulator at -80mV of holding potential depending on different NIR power. The blue light intensity of the PV-LED stimulator was sufficient to modulate ChR2 expressed cell by blue light-sensitive cation channel in HEK293 cells in vitro. With holding potential of -80 mV at a NIR power of 16 mW, the induced maximum photocurrent was measured at 148.09 pA. Because

the ChR2 channel is a cationic channel, the negative holding potential setting in whole-cell patch mode attracts more cations from outside the cell membrane to the inside of the cell than the positive holding potential. Thus, as holding potential increases to the level of 20 mV, the current-voltage characteristic was measured to inversion potential at about 20 mV of holding potential as shown in figure 4.31, which is typical for the ChR2 channel. Therefore, the photocurrent induced by the PV-LED stimulator would be enough to trigger a neural firing if it were implanted into the mammal brain.

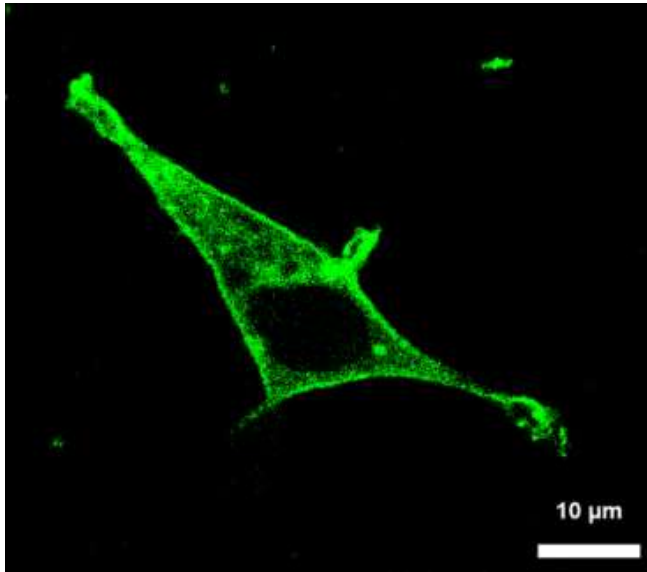
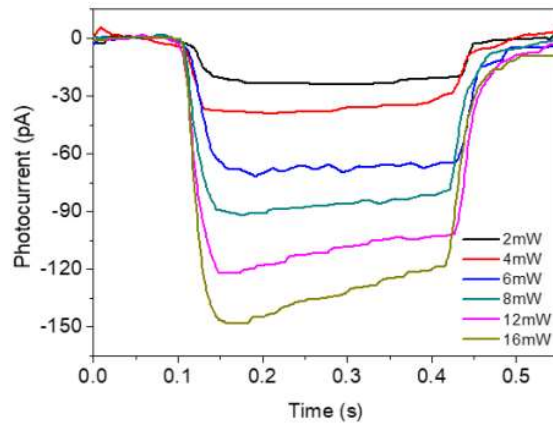
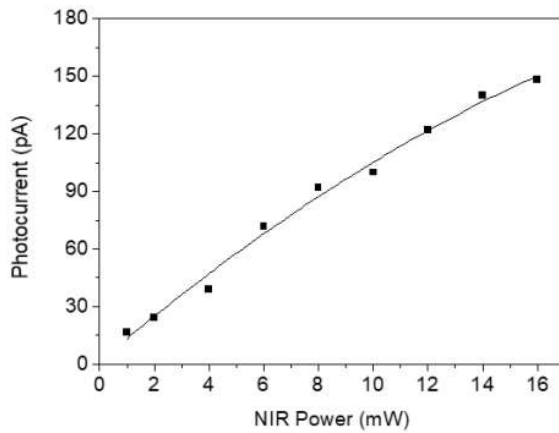


Figure 4. 29 Fluorescence image of a ChR2-EYFP expressed HEK293 cell.



(a)



(b)

Figure 4. 30 (a) Whole-cell voltage-clamp recording from ChR2-EYFP expressed HEK293 cell at different NIR power during 300 ms illumination at -80 mV holding potential. (b) Photocurrents of ChR2 with 850 nm laser power according to NIR power at -80 mV holding potential.

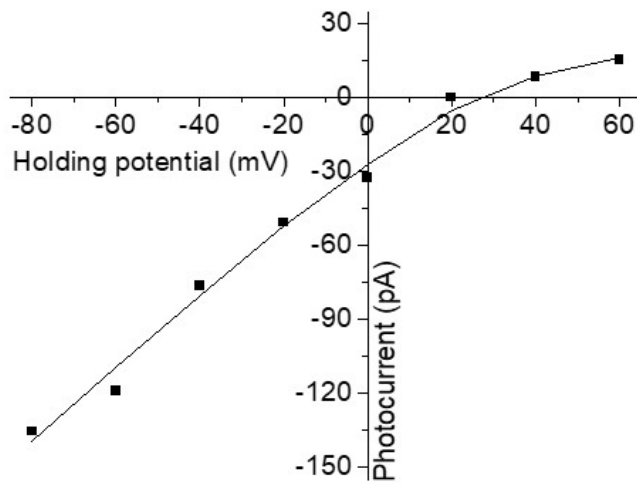


Figure 4. 31 Current-voltage characteristics of ChR2 on emission of PV-LED stimulator according to holding potential at 16 mW of NIR power.

4.3.4.2 Neuron

To check the expression of ChR2-EYFP in neurons, the fluorescence of EYFP was also detected as shown in figure 4.32 using the confocal laser scanning microscope (Carl Zeiss LSM 700).

Figure 4.33 shows the recording form of the whole-cell current-clamp of the ChR2-EYFP expressed neurons depending on different NIR power for 10 ms and 15 ms of exposure times of blue light by PV-LED stimulator. Neural firing was not observed below 7 mW of NIR power at an exposure time of 10 ms but was measured at 10 mW. The intensity of the PV-LED stimulator emissions is 1.881 mW/mm^2 at NIR power of 10 mW. For 15 ms exposure time, no spike of the neuron was observed under NIR power at 5 mW, but a spike of the neuron was found at more than 7 mW. The intensity of the PV-LED stimulator emissions is 1.414 mW/mm^2 at NIR power of 7 mW. Long exposure times allowed neurons to be stimulated by PV-LED stimulator with lower power than short exposure times. When a PV-LED stimulator is implanted into the mammal brain, neurons near the device can be stimulated sufficiently with a NIR power of less than 1 mW. The blue emission intensity near the PV-LED stimulator is 2.71 mW/mm^2 at 1 mW of NIR power as shown in Figure 4.34. The possible range of stimulation of ChR2-

expressed neurons with the PV-LED stimulator is shown in figure 3.43 as the area above the red dotted line. If the NIR power delivered to PV-LED stimulator is higher, it can stimulate not only ChR2-expressed neurons closed to stimulator but also deeper ChR2-expressed cells.

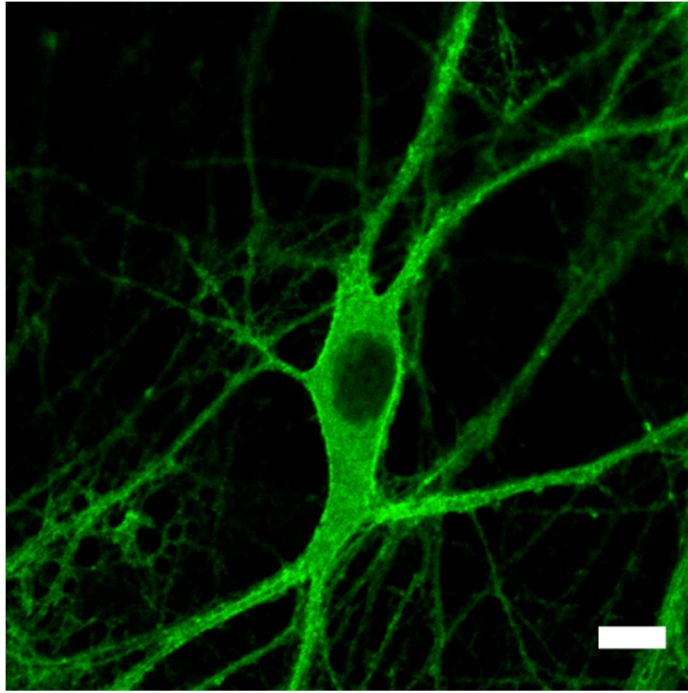


Figure 4. 32 Fluorescence image of a ChR2-EYFP expressed Neuron. The scale is 10 μm .

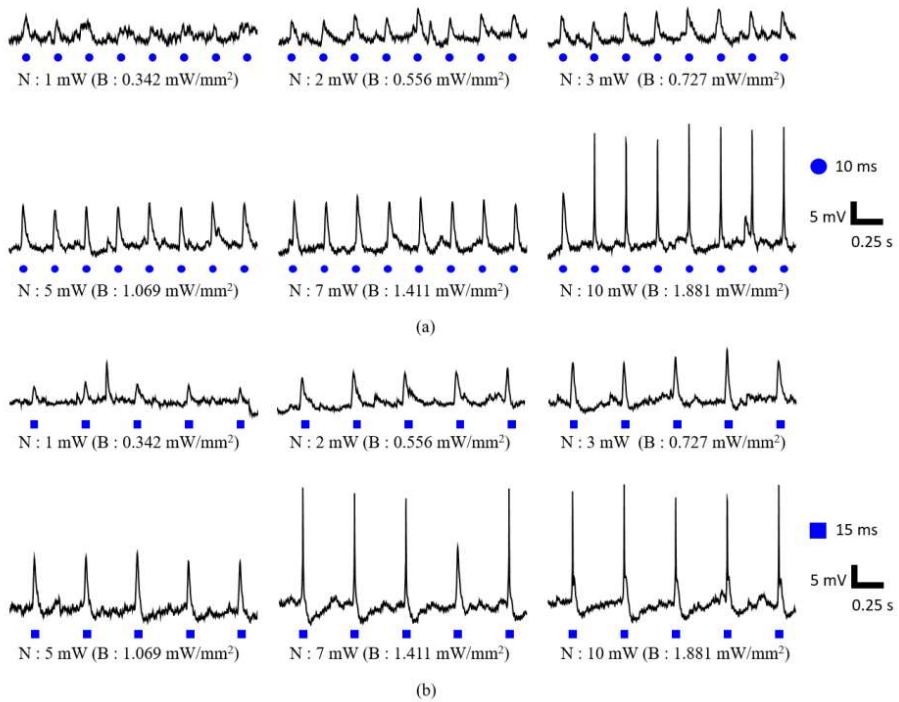


Figure 4. 33 Whole-cell current-clamp recordings from Chr2–EYFP expressed neurons at different NIR power. (a) 10 ms and (b) 15 ms of LED exposure time. N : NIR Power, B : LED intensity.

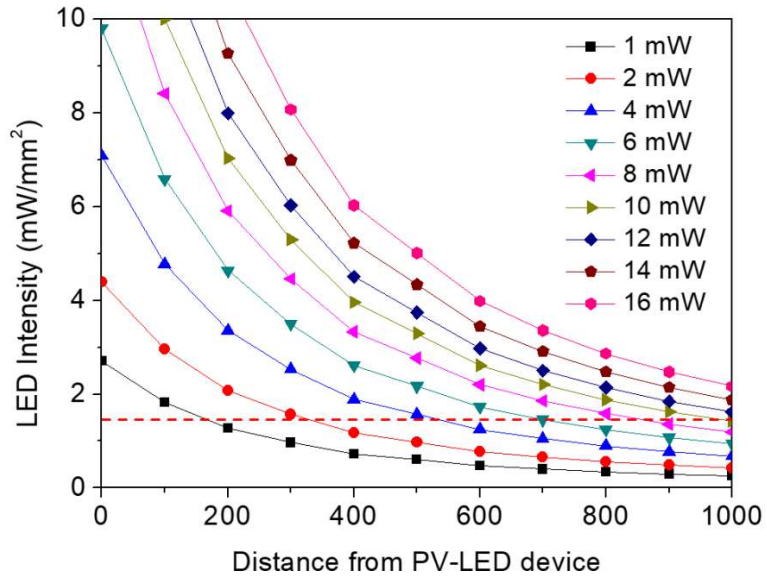


Figure 4. 34 Emission intensity of PV-LED stimulator according to distance from the PV-LED stimulator at different NIR powers. Neural stimulation using the PV-LED stimulator is possible in the region above the red dashed line.

4.4 Discussion

In this chapter, an optoelectronic neural stimulator using a light-absorbing the PV cell with through-hole via and a light-emitting micro-LED has been developed. The PV cell absorbs 820~850 nm wavelengths of light, which is good for tissue penetration and the micro-LED emits blue light (449.2 nm) to stimulate ChR2-expressed cells. The maximum power conversion efficiency of the PV cell is 35% at 6 mW of input power. After bonding the PV cell and micro-LED, efficiency was measured to be about 8% at 1 mW of NIR power. The blue light intensity of the PV-LED stimulator when closest to the device was about 2.7 mW/mm² at 1 mW of NIR power. This is sufficient intensity to stimulate ChR2-expressed neurons. In vitro experiments confirmed that ChR2-expressed neurons were stimulated at about 1.4 mW/mm² of blue light intensity and 15 ms of exposure time. The developed optoelectronic stimulator in this chapter can be fully utilized for deep brain stimulation. It can help to provide a spatially precise analysis and functional understanding of relationships in neural networks. It can also help in the study of treatments for neurological diseases such as Alzheimer's, Parkinson's, depression and anxiety.

References

- [1] G. M. Clark, "The multi-channel cochlear implant: Multi-disciplinary development of electrical stimulation of the cochlea and the resulting clinical benefit," *Hearing Research*, vol. 322, pp. 4-13, Apr, 2015.
- [2] W. F. House, "Cochlear Implants," *Annals of Otolaryngology and Laryngology*, vol. 85, no. 3, pp. 3-93, 1976.
- [3] B. S. Wilson, C. C. Finley, D. T. Lawson, R. D. Wolford, D. K. Eddington, and W. M. Rabinowitz, "Better Speech Recognition with Cochlear Implants," *Nature*, vol. 352, no. 6332, pp. 236-238, Jul 18, 1991.
- [4] S. F. Cogan, "Neural stimulation and recording electrodes," *Annu Rev Biomed Eng*, vol. 10, pp. 275-309, 2008.
- [5] T. L. Rose, E. M. Kelliher, and L. S. Robblee, "Assessment of Capacitor Electrodes for Intracortical Neural Stimulation," *Journal of Neuroscience Methods*, vol. 12, no. 3, pp. 181-193, 1985.
- [6] J. D. Weiland, D. J. Anderson, and M. S. Humayun, "In vitro electrical properties for iridium oxide versus titanium nitride stimulating electrodes," *IEEE Transactions on Biomedical Engineering*, vol. 49, no. 12, pp. 1574-1579, Dec, 2002.
- [7] S. F. Cogan, A. A. Guzelian, W. F. Agnew, T. G. H. Yuen, and D. B. McCreery, "Over-pulsing degrades activated iridium oxide films used for intracortical neural stimulation," *Journal of Neuroscience Methods*, vol. 137, no. 2, pp. 141-150, Aug 30, 2004.
- [8] J. E. B. Randles, "Kinetics of Rapid Electrode Reactions," *Discussions of the Faraday Society*, vol. 1, pp. 11-19, 1947.
- [9] K. Tybrandt, I. V. Zozoulenko, and M. Berggren, "Chemical potential-electric double layer coupling in conjugated polymer-polyelectrolyte blends," *Science Advances*, vol. 3, no. 12, eaao3659,

Dec, 2017.

- [10] N. Driscoll, A. G. Richardson, K. Maleski, B. Anasori, O. Adewole, P. Lelyukh, L. Escobedo, D. K. Cullen, T. H. Lucas, Y. Gogotsi, and F. Vitale, "Two-Dimensional Ti_3C_2 MXene for High-Resolution Neural Interfaces," *ACS Nano*, vol. 12, no. 10, pp. 10419-10429, Oct 23, 2018.
- [11] U. E. M. Janders, M. Stelzle, W. Nisch, "Novel thin film titanium nitride micro-electrodes with excellent charge transfer capability for cell stimulation and sensing applications," *18th Annual International Conference of the IEEE Engineering in Medicine and Biology Society, Amsterdam 1996*, pp. 245-247, 31 Oct.-3 Nov. 1996.
- [12] S. Shin, J. Kim, J. Jeong, T. M. Gwon, G. J. Choi, S. E. Lee, J. Kim, S. B. Jun, J. W. Chang, and S. J. Kim, "High Charge Storage Capacity Electrodeposited Iridium Oxide Film on Liquid Crystal Polymer -Based Neural Electrodes," *Sensors and Materials*, vol. 28, no. 3, pp. 243-260, 2016.
- [13] M. Ganji, A. Tanaka, V. Gilja, E. Halgren, and S. A. Dayeh, "Scaling Effects on the Electrochemical Stimulation Performance of Au, Pt, and PEDOT:PSS Electrocorticography Arrays," *Advanced Functional Materials*, vol. 27, no. 42, 1703019, Nov 10, 2017.
- [14] T. D. Y. Kozai, K. Catt, Z. H. Du, K. Na, O. Srivannavit, R. U. M. Haque, J. Seymour, K. D. Wise, E. Yoon, and X. T. Cui, "Chronic In Vivo Evaluation of PEDOT/CNT for Stable Neural Recordings," *IEEE Transactions on Biomedical Engineering*, vol. 63, no. 1, pp. 111-119, Jan, 2016.
- [15] R. Gerwig, K. Fuchsberger, B. Schroepel, G. S. Link, G. Heusel, U. Kraushaar, W. Schuhmann, A. Stett, and M. Stelzle, "PEDOT-CNT Composite Microelectrodes for Recording and Electrostimulation Applications: Fabrication, Morphology, and Electrical Properties," *Front Neuroeng*, vol. 5, pp. 8, 2012.

- [16] S. Y. Chen, W. H. Pei, Q. Gui, R. Y. Tang, Y. F. Chen, S. S. Zhao, H. Wang, and H. D. Chen, "PEDOT/MWCNT composite film coated microelectrode arrays for neural interface improvement," *Sensors and Actuators a-Physical*, vol. 193, pp. 141-148, Apr 15, 2013.
- [17] T. L. Rose, and L. S. Robblee, "Electrical stimulation with Pt electrodes. VIII. Electrochemically safe charge injection limits with 0.2 ms pulses," *IEEE Trans Biomed Eng*, vol. 37, no. 11, pp. 1118-1120, Nov, 1990.
- [18] S. F. Cogan, T. D. Plante, and J. Ehrlich, "Sputtered iridium oxide films (SIROFs) for low-impedance neural stimulation and recording electrodes," *Conf Proc IEEE Eng Med Biol Soc*, vol. 6, pp. 4153-4156, 2004.
- [19] S. Venkatraman, J. Hendricks, Z. A. King, A. J. Sereno, S. Richardson-Burns, D. Martin, and J. M. Carmena, "In vitro and in vivo evaluation of PEDOT microelectrodes for neural stimulation and recording," *IEEE Trans Neural Syst Rehabil Eng*, vol. 19, no. 3, pp. 307-316, Jun, 2011.
- [20] R. A. Green, N. H. Lovell, G. G. Wallace, and L. A. Poole-Warren, "Conducting polymers for neural interfaces: challenges in developing an effective long-term implant," *Biomaterials*, vol. 29, no. 24-25, pp. 3393-3399, Aug-Sep, 2008.
- [21] M. J. M. Lois S. Robblee, Ellen D. Lasinsky, Angela G. Kimball and S. Barry Brummer, "Charge Injection Properties of Thermally-Prepared Iridium Oxide Films," *Symposium G – Biomedical Materials*, vol. 55, 303, 1985.
- [22] F. G. Tahmid Latif, Michael Dickey, Mihail Sichitiu, Alper Bozkurt, "Using liquid metal alloy (EGaIn) to electrochemically enhance SS stimulation electrodes for biobotic applications," *2016 38th Annual International Conference of the IEEE Engineering in Medicine and Biology Society (EMBC)*, pp. 2141-2144, 2016.

- [23]R. Samba, T. Herrmann, and G. Zeck, "PEDOT-CNT coated electrodes stimulate retinal neurons at low voltage amplitudes and low charge densities," *Journal of Neural Engineering*, vol. 12, no. 1, 016014, Feb, 2015.
- [24]X. T. Cul, and D. D. Zhou, "Poly (3,4-ethylenedioxythiophene) for chronic neural stimulation," *IEEE Transactions on Neural Systems and Rehabilitation Engineering*, vol. 15, no. 4, pp. 502-508, Dec, 2007.
- [25]R. A. Green, R. T. Hassarati, L. Bouchinet, C. S. Lee, G. L. M. Cheong, J. F. Yu, C. W. Dodds, G. J. Suaning, L. A. Poole-Warren, and N. H. Lovell, "Substrate dependent stability of conducting polymer coatings on medical electrodes," *Biomaterials*, vol. 33, no. 25, pp. 5875-5886, Sep, 2012.
- [26]D. H. Kim, S. M. Richardson-Burns, J. L. Hendricks, C. Sequera, and D. C. Martin, "Effect of immobilized nerve growth factor on conductive polymers: Electrical properties and cellular response," *Advanced Functional Materials*, vol. 17, no. 1, pp. 79-86, Jan 5, 2007.
- [27]J. D. Weiland, D. J. Anderson, and M. S. Humayun, "In vitro electrical properties for iridium oxide versus titanium nitride stimulating electrodes," *IEEE Trans Biomed Eng*, vol. 49, no. 12 Pt 2, pp. 1574-1579, Dec, 2002.
- [28]O. J. Abilez, J. Wong, R. Prakash, K. Deisseroth, C. K. Zarins, and E. Kuhl, "Multiscale Computational Models for Optogenetic Control of Cardiac Function," *Biophysical Journal*, vol. 101, no. 6, pp. 1326-1334, Sep 21, 2011.
- [29]E. S. Boyden, F. Zhang, E. Bamberg, G. Nagel, and K. Deisseroth, "Millisecond-timescale, genetically targeted optical control of neural activity," *Nat Neurosci*, vol. 8, no. 9, pp. 1263-1268, Sep, 2005.

- [30]K. Deisseroth, “Optogenetics,” *Nat Methods*, vol. 8, no. 1, pp. 26-29, Jan, 2011.
- [31]G. Nagel, T. Szellas, W. Huhn, S. Kateriya, N. Adeishvili, P. Berthold, D. Ollig, P. Hegemann, and E. Bamberg, “Channelrhodopsin-2, a directly light-gated cation-selective membrane channel,” *Proc Natl Acad Sci U S A*, vol. 100, no. 24, pp. 13940-13945, Nov 25, 2003.
- [32]F. Zhang, M. Prigge, F. Beyriere, S. P. Tsunoda, J. Mattis, O. Yizhar, P. Hegemann, and K. Deisseroth, “Red-shifted optogenetic excitation: a tool for fast neural control derived from *Volvox carteri*,” *Nat Neurosci*, vol. 11, no. 6, pp. 631-633, Jun, 2008.
- [33]T. I. Kim, J. G. McCall, Y. H. Jung, X. Huang, E. R. Siuda, Y. Li, J. Song, Y. M. Song, H. A. Pao, R. H. Kim, C. Lu, S. D. Lee, I. S. Song, G. Shin, R. Al-Hasani, S. Kim, M. P. Tan, Y. Huang, F. G. Omenetto, J. A. Rogers, and M. R. Bruchas, “Injectable, cellular-scale optoelectronics with applications for wireless optogenetics,” *Science*, vol. 340, no. 6129, pp. 211-216, Apr 12, 2013.
- [34]C. Lu, U. P. Frierip, R. A. Koppes, A. Canales, V. Caggiano, J. Selvidge, E. Bizzi, and P. Anikeeva, “Polymer Fiber Probes Enable Optical Control of Spinal Cord and Muscle Function In Vivo,” *Advanced Functional Materials*, vol. 24, no. 42, pp. 6594-6600, Nov 12, 2014.
- [35]F. Pisanello, L. Sileo, I. A. Oldenburg, M. Pisanello, L. Martiradonna, J. A. Assad, B. L. Sabatini, and M. De Vittorio, “Multipoint-emitting optical fibers for spatially addressable in vivo optogenetics,” *Neuron*, vol. 82, no. 6, pp. 1245-1254, Jun 18, 2014.
- [36]H. J. L. Yoojin Son, Dohee Kim, Yun Kyung Kim, Eui-Sung Yoon, Ji Yoon Kang, Nakwon Choi, Tae Geun Kim, Il-Joo Cho, “MEMS neural probe array for multiple-site optical stimulation with low-loss optical waveguide by using thick glass cladding layer,” *2014 IEEE*

- 27th International Conference on Micro Electro Mechanical Systems (MEMS)*, pp. 853-856, 26-30 Jan. 2014, 2014.
- [37] D. Budai, A. D. Vizvari, Z. K. Bali, B. Marki, L. V. Nagy, Z. Konya, D. Madarasz, N. Henn-Mike, C. Varga, and I. Hernadi, "A novel carbon tipped single micro-optrode for combined optogenetics and electrophysiology," *Plos One*, vol. 13, no. 3, e0193836, Mar 7, 2018.
- [38] H. Cao, L. Gu, S. K. Mohanty, and J. C. Chiao, "An Integrated mu LED Optrode for Optogenetic Stimulation and Electrical Recording," *IEEE Transactions on Biomedical Engineering*, vol. 60, no. 1, pp. 225-229, Jan, 2013.
- [39] S. Dufour, and Y. De Koninck, "Optrodes for combined optogenetics and electrophysiology in live animals," *Neurophotonics*, vol. 2, no. 3, 031205, Jul-Sep, 2015.
- [40] I. Ozden, J. Wang, Y. Lu, T. May, J. Lee, W. Goo, D. J. O'Shea, P. Kalanithi, I. Diester, M. Diagne, K. Deisseroth, K. V. Shenoy, and A. V. Nurmikko, "A coaxial optrode as multifunction write-read probe for optogenetic studies in non-human primates," *Journal of Neuroscience Methods*, vol. 219, no. 1, pp. 142-154, Sep 30, 2013.
- [41] J. Wang, F. Wagner, M. Diagne, D. A. Borton, J. Y. Zhang, I. Ozden, R. D. Burwell, A. V. Nurmikko, R. van Wagenen, I. Diester, and K. Deisseroth, "Integrated device for combined optical neuromodulation and electrical recording for chronic in vivo applications" *Journal of Neural Engineering*, vol. 9, no.1, 016001, Dec, 2012.
- [42] T. Y. Chiang, M. C. Huang, and C. H. Tsai, "The effects of solvent on the electrochromic properties of poly(3,4-ethylenedioxythiophene)," *Rsc Advances*, vol. 4, no. 41, pp. 21201-21207, 2014.
- [43] M. O. P. Kara, and M. W. Frey, "Effects of Solvents on the Morphology and Conductivity of Poly(3,4-ethylenedioxythiophene):

- Poly(styrenesulfonate) Nanofibers,” *Journal of Applied Polymer Science*, vol. 131, no. 11, 40305, Jun 5, 2014.
- [44] T. R. Chou, S. H. Chen, Y. T. Chiang, Y. T. Lin, and C. Y. Chao, “Highly conductive PEDOT:PSS films by post-treatment with dimethyl sulfoxide for ITO-free liquid crystal display,” *Journal of Materials Chemistry C*, vol. 3, no. 15, pp. 3760-3766, 2015.
- [45] Q. D. Li, J. W. Yang, S. S. Chen, J. Z. Zou, W. G. Xie, and X. R. Zeng, “Highly Conductive PEDOT:PSS Transparent Hole Transporting Layer with Solvent Treatment for High Performance Silicon/Organic Hybrid Solar Cells,” *Nanoscale Research Letters*, vol. 12, 506, Aug 23, 2017.
- [46] P. Kshirsagar, S. Dickreuter, M. Mierzejewski, C. Burkhardt, T. Chasse, M. Fleischer, and P. D. Jones, “Transparent Graphene/PEDOT:PSS Microelectrodes for Electro- and Optophysiology,” *Advanced Materials Technologies*, vol. 4, no. 1, 1800318, Jan, 2019.
- [47] S. Lee, T. Eom, M. K. Kim, S. G. Yang, and B. S. Shim, “Durable soft neural micro-electrode coating by an electrochemical synthesis of PEDOT:PSS / graphene oxide composites,” *Electrochimica Acta*, vol. 313, pp. 79-90, Aug 1, 2019.
- [48] L. Ferlauto, A. N. D'Angelo, P. Vagni, M. J. I. A. Leccardi, F. M. Mor, E. A. Cuttaz, M. O. Heuschkel, L. Stoppini, and D. Ghezzi, “Development and Characterization of PEDOT:PSS/Alginate Soft Microelectrodes for Application in Neuroprosthetics,” *Frontiers in Neuroscience*, vol. 12, 648, Sep 19, 2018.
- [49] J. P. E. Grolier, and E. Wilhelm, “Excess Volumes and Excess Heat-Capacities of Water + Ethanol at 298.15-K,” *Fluid Phase Equilibria*, vol. 6, no. 3-4, pp. 283-287, 1981.
- [50] I. S. Khattab, F. Bandarkar, M. A. A. Fakhree, and A. Jouyban, “Density, viscosity, and surface tension of water plus ethanol

- mixtures from 293 to 323 K,” *Korean Journal of Chemical Engineering*, vol. 29, no. 6, pp. 812-817, Jun, 2012.
- [51] C. W. Fanglei Zhou, Weiguo Wang, Zhao Yang, Faquan Yu, Yuanxin Wu, Ruan Chi, “Effect of alcohol on cellulose hydrolysis in super/subcritical alcohol-water mixtures,” *2011 International Conference on Materials for Renewable Energy & Environment*, pp. 548-511, 2011.
- [52] Y. J. Xia, and J. Y. Ouyang, “PEDOT:PSS films with significantly enhanced conductivities induced by preferential solvation with cosolvents and their application in polymer photovoltaic cells,” *Journal of Materials Chemistry*, vol. 21, no. 13, pp. 4927-4936, 2011.
- [53] A. F. Lasagni, J. L. Hendricks, C. M. Shaw, D. J. Yuan, D. C. Martin, and S. Das, “Direct laser interference patterning of poly(3,4-ethylene dioxythiophene)-poly(styrene sulfonate) (PEDOT-PSS) thin films,” *Applied Surface Science*, vol. 255, no. 22, pp. 9186-9192, Aug 30, 2009.
- [54] N. G. Semaltianos, C. Koidis, C. Pitsalidis, P. Karagiannidis, S. Logothetidis, W. Perrie, D. Liu, S. P. Edwardson, E. Fearon, R. J. Potter, G. Dearden, and K. G. Watkins, “Picosecond laser patterning of PEDOT:PSS thin films,” *Synthetic Metals*, vol. 161, no. 5-6, pp. 431-439, Mar, 2011.
- [55] S. F. Tseng, W. T. Hsiao, K. C. Huang, and D. Y. Chiang, “Electrode patterning on PEDOT:PSS thin films by pulsed ultraviolet laser for touch panel screens,” *Applied Physics a-Materials Science & Processing*, vol. 112, no. 1, pp. 41-47, Jul, 2013.
- [56] M. S. Kim, D. H. Lee, K. B. Kim, S. H. Jung, J. K. Lee, B. H. O, S. G. Lee, and S. G. Park, “Lift-off patterning of Ag nanowire/PEDOT:PSS composite films for transparent electrodes using a fluoropolymer structure,” *Thin Solid Films*, vol. 587, pp. 100-105, Jul 31, 2015.

- [57] K. B. Kim, M. S. Kim, D. H. Lee, B. M. Choi, K. S. Jung, S. H. Jung, J. K. Lee, O. Beom-Hoan, S. G. Lee, and S. G. Park, "Lift-off patterning of multi-walled carbon nanotube and PEDOT:PSS composite films with fluorinated polymer templates," *Microelectronic Engineering*, vol. 145, pp. 160-165, Sep 1, 2015.
- [58] M. Y. Teo, N. RaviChandran, N. Kim, S. Kee, L. Stuart, K. C. Aw, and J. Stringer, "Direct Patterning of Highly Conductive PEDOT:PSS/Ionic Liquid Hydrogel via Microreactive Inkjet Printing," *ACS Applied Materials & Interfaces*, vol. 11, no. 40, pp. 37069-37076, Oct 9, 2019.
- [59] T. Mustonen, K. Kordas, S. Saukko, G. Toth, J. S. Penttilla, P. Helisto, H. Seppa, and H. Jantunen, "Inkjet printing of transparent and conductive patterns of single-walled carbon nanotubes and PEDOT-PSS composites," *Physica Status Solidi B-Basic Solid State Physics*, vol. 244, no. 11, pp. 4336-4340, Nov, 2007.
- [60] X. He, G. Z. Shen, R. B. Xu, W. J. Yang, C. Zhang, Z. H. Liu, B. H. Chen, J. Y. Liu, and M. X. Song, "Hexagonal and Square Patterned Silver Nanowires/PEDOT:PSS Composite Grids by Screen Printing for Uniformly Transparent Heaters," *Polymers*, vol. 11, no. 3, Mar 12, 2019.
- [61] D. Zielke, R. Gogolin, M. U. Halbich, C. Marquardt, W. Lovenich, R. Sauer, and J. Schmidt, "Large-Area PEDOT:PSS/c-Si Heterojunction Solar Cells With Screen-Printed Metal Contacts," *Solar Rrl*, vol. 2, no. 3, 468, Mar, 2018.
- [62] L. S. Pali, R. Jindal, and A. Garg, "Screen printed PEDOT:PSS films as transparent electrode and its application in organic solar cells on opaque substrates," *Journal of Materials Science-Materials in Electronics*, vol. 29, no. 13, pp. 11030-11038, Jul, 2018.
- [63] P. C. Taylor, J. K. Lee, A. A. Zakhidov, M. Chatzichristidi, H. H. Fong, J. A. DeFranco, G. C. Malliaras, and C. K. Ober, "Orthogonal

- Patterning of PEDOT:PSS for Organic Electronics using Hydrofluoroether Solvents,” *Advanced Materials*, vol. 21, no. 22, pp. 2314-2317, Jun 12, 2009.
- [64] D. Q. Wang, S. H. Ouyang, Y. T. Xie, T. Tan, D. L. Zhu, X. Xu, and H. H. Fong, “Two Photolithographic Patterning Schemes for PEDOT:PSS and Their Applications in Organic Light-Emitting Diodes,” *Journal of Display Technology*, vol. 12, no. 4, pp. 338-343, Apr, 2016.
- [65] S. Lee, T. Geiller, A. Jung, R. Nakajima, Y. K. Song, and B. J. Baker, “Improving a genetically encoded voltage indicator by modifying the cytoplasmic charge composition,” *Scientific Reports*, vol. 7, 8286, Aug 15, 2017.
- [66] P. Sakunpongpitorn, K. Phasukom, N. Paradee, and A. Sirivat, “Facile synthesis of highly conductive PEDOT:PSS via surfactant templates,” *Rsc Advances*, vol. 9, no. 11, pp. 6363-6378, Feb 21, 2019.
- [67] X. K. Wu, L. Lian, S. Yang, and G. F. He, “Highly conductive PEDOT:PSS and graphene oxide hybrid film from a dipping treatment with hydroiodic acid for organic light emitting diodes,” *Journal of Materials Chemistry C*, vol. 4, no. 36, pp. 8528-8534, 2016.
- [68] A. J. Olivares, I. Cosme, M. E. Sanchez-Vergara, S. Mansurova, J. C. Carrillo, H. E. Martinez, and A. Itzmoyotl, “Nanostructural Modification of PEDOT:PSS for High Charge Carrier Collection in Hybrid Frontal Interface of Solar Cells,” *Polymers*, vol. 11, no. 6, 1034, Jun 11, 2019.
- [69] J. N. Begam, “Biosynthesis and characterization of silver nanoparticles (AgNPs) using marine bacteria against certain human pathogens,” *International Journal of Advances in Scientific Research*, vol. 2, no. 7, pp. 152-156, 2016.

- [70] S. Kannan, "FT-IR and EDS analysis of the seaweeds *Sargassum wightii* (brown algae) and *Gracilaria corticata* (red algae)," *International Journal of Current Microbiology and Applied Sciences*, vol. 3, no. 4, pp. 341-351, 2014.
- [71] G. A. Camara, and T. Iwasita, "Parallel pathways of ethanol oxidation: The effect of ethanol concentration," *Journal of Electroanalytical Chemistry*, vol. 578, no. 2, pp. 315-321, May 1, 2005.
- [72] L. M. Johnson, L. Gao, C. W. Shields, M. Smith, K. Efimenko, K. Cushing, J. Genzer, and G. P. Lopez, "Elastomeric microparticles for acoustic mediated bioseparations," *Journal of Nanobiotechnology*, vol. 11, 22, Jun 28, 2013.
- [73] Y. H. Son, W. C. Jung, J. I. Jeong, N. G. Park, I. S. Kim, and I. H. Bae, "FTIR characteristics of hydrogenated amorphous carbon films prepared by ECR-PECVD," *Journal of the Korean Physical Society*, vol. 39, no. 4, pp. 713-717, Oct, 2001.
- [74] B. Friedel, P. E. Keivanidis, T. J. K. Brenner, A. Abrusci, C. R. McNeill, R. H. Friend, and N. C. Greenham, "Effects of Layer Thickness and Annealing of PEDOT:PSS Layers in Organic Photodetectors," *Macromolecules*, vol. 42, no. 17, pp. 6741-6747, Sep 8, 2009.
- [75] Q. Wang, C. C. Chueh, M. Eslamian, and A. K. Y. Jen, "Modulation of PEDOT:PSS pH for Efficient Inverted Perovskite Solar Cells with Reduced Potential Loss and Enhanced Stability," *ACS Applied Materials & Interfaces*, vol. 8, no. 46, pp. 32068-32076, Nov 23, 2016.
- [76] Y. J. Xia, and J. Y. Ouyang, "Significant Conductivity Enhancement of Conductive Poly(3,4-ethylenedioxythiophene): Poly(styrenesulfonate) Films through a Treatment with Organic Carboxylic Acids and Inorganic Acids," *ACS Applied Materials &*

- Interfaces*, vol. 2, no. 2, pp. 474-483, Feb, 2010.
- [77] A. Albert, "Ionization, Ph and Biological Activity," *Pharmacological Reviews*, vol. 4, no. 2, pp. 136-167, 1952.
- [78] J. Liigand, A. Laaniste, and A. Kruve, "pH Effects on Electrospray Ionization Efficiency," *Journal of the American Society for Mass Spectrometry*, vol. 28, no. 3, pp. 461-469, Mar, 2017.
- [79] D. A. Mengistie, P. C. Wang, and C. W. Chu, "Effect of molecular weight of additives on the conductivity of PEDOT: PSS and efficiency for ITO-free organic solar cells," *Journal of Materials Chemistry A*, vol. 1, no. 34, pp. 9907-9915, 2013.
- [80] Z. Y. Zhu, C. C. Liu, F. X. Jiang, J. K. Xu, and E. D. Liu, "Effective treatment methods on PEDOT:PSS to enhance its thermoelectric performance," *Synthetic Metals*, vol. 225, pp. 31-40, Mar, 2017.
- [81] J. Y. Kim, J. H. Jung, D. E. Lee, and J. Joo, "Enhancement of electrical conductivity of poly(3,4-ethylenedioxythiophene)/poly(4-styrenesulfonate) by a change of solvents," *Synthetic Metals*, vol. 126, no. 2-3, pp. 311-316, Feb 14, 2002.
- [82] V. Forsberg, J. Maslik, and M. Norgren, "Electronic performance of printed PEDOT:PSS lines correlated to the physical and chemical properties of coated inkjet papers," *RSC Advances*, vol. 9, no. 41, pp. 23925-23938, Aug 4, 2019.
- [83] H. Park, S. H. Lee, F. S. Kim, H. H. Choi, I. W. Cheong, and J. H. Kim, "Enhanced thermoelectric properties of PEDOT: PSS nanofilms by a chemical dedoping process," *Journal of Materials Chemistry A*, vol. 2, no. 18, pp. 6532-6539, 2014.
- [84] H. S. Wang, S. H. Kim, S. Y. Joe, S. H. Lee, I. Kim, and K. Song, "Raman Spectroscopic Studies of Ionic Liquid Effects on Electroconductive PEDOT:PSS Thin Film," *Polymer-Korea*, vol. 42, no. 1, pp. 80-86, Jan, 2018.
- [85] S. H. Chang, C. H. Chiang, F. S. Kao, C. L. Tien, and C. G. Wu,

- “Unraveling the Enhanced Electrical Conductivity of PEDOT:PSS Thin Films for ITO-Free Organic Photovoltaics,” *IEEE Photonics Journal*, vol. 6, no. 4, 8400307, Aug, 2014.
- [86] T. S. Wang, M. Farajollahi, S. Henke, T. T. Zhu, S. R. Bajpe, S. J. Sun, J. S. Barnard, J. S. Lee, J. D. W. Madden, A. K. Cheetham, and S. K. Smoukov, “Functional conductive nanomaterials via polymerisation in nano-channels: PEDOT in a MOF,” *Materials Horizons*, vol. 4, no. 1, pp. 64-71, Jan 1, 2017.
- [87] A. J. Olivares, I. Cosme, M. E. Sanchez-Vergara, S. Mansurova, J. C. Carrillo, H. E. Martinez, and A. Itzmoyotl, “Nanostructural Modification of PEDOT:PSS for High Charge Carrier Collection in Hybrid Frontal Interface of Solar Cells,” *Polymers*, vol. 11, no. 6, 1034, Jun, 2019.
- [88] M. L. Kringelbach, N. Jenkinson, S. L. F. Owen, and T. Z. Aziz, “Translational principles of deep brain stimulation,” *Nature Reviews Neuroscience*, vol. 8, no. 8, pp. 623-635, Aug, 2007.
- [89] H. S. Mayberg, A. M. Lozano, V. Voon, H. E. McNeely, D. Seminowicz, C. Hamani, J. M. Schwalb, and S. H. Kennedy, “Deep brain stimulation for treatment-resistant depression,” *Neuron*, vol. 45, no. 5, pp. 651-660, Mar 3, 2005.
- [90] T. L. Rose, and L. S. Robblee, “Electrical-Stimulation with Pt Electrodes .8. Electrochemically Safe Charge Injection Limits with 0.2 Ms Pulses,” *IEEE Transactions on Biomedical Engineering*, vol. 37, no. 11, pp. 1118-1120, Nov, 1990.
- [91] B. Rosenberg, L. Vancamp, and T. Krigas, “Inhibition of Cell Division in Escherichia Coli by Electrolysis Products from a Platinum Electrode,” *Nature*, vol. 205, no. 4972, pp. 698-699, 1965.
- [92] S. Woldring, and M. N. J. Dirken, “Spontaneous Unit-Activity in the Superficial Cortical Layers,” *Acta Physiologica Et Pharmacologica Neerlandica*, vol. 1, no. 3, pp. 369-379, 1950.

- [93] X. Y. Cui, and D. C. Martin, "Fuzzy gold electrodes for lowering impedance and improving adhesion with electrodeposited conducting polymer films," *Sensors and Actuators a-Physical*, vol. 103, no. 3, pp. 384-394, Feb 15, 2003.
- [94] P. T. McCarthy, R. Madangopal, K. J. Otto, and M. P. Rao, "Titanium-based multi-channel, micro-electrode array for recording neural signals," *Conf Proc IEEE Eng Med Biol Soc*, vol. 2009, pp. 2062-2065, 2009.
- [95] I. del Agua, D. Mantione, U. Ismailov, A. Sanchez-Sanchez, N. Aramburu, G. G. Malliaras, D. Mecerreyes, and E. Ismailova, "DVS-Crosslinked PEDOT:PSS Free-Standing and Textile Electrodes toward Wearable Health Monitoring," *Advanced Materials Technologies*, vol. 3, no. 10, 1700322, Oct, 2018.
- [96] A. Hakansson, S. B. Han, S. H. Wang, J. Lu, S. Braun, M. Fahlman, M. Berggren, X. Crispin, and S. Fabiano, "Effect of (3-Glycidyloxypropyl)Trimethoxysilane (GOPS) on the Electrical Properties of PEDOT:PSS Films," *Journal of Polymer Science Part B-Polymer Physics*, vol. 55, no. 10, pp. 814-820, May 15, 2017.
- [97] D. Mantione, I. del Agua, W. Schaafsma, M. ElMahmoudy, I. Uguz, A. Sanchez-Sanchez, H. Sardon, B. Castro, G. G. Malliaras, and D. Mecerreyes, "Low-Temperature Cross-Linking of PEDOT:PSS Films Using Divinylsulfone," *ACS Applied Materials & Interfaces*, vol. 9, no. 21, pp. 18254-18262, May 31, 2017.
- [98] M. Solazzo, K. Krukiewicz, A. Zhussupbekova, K. Fleischer, M. J. Biggs, and M. G. Monaghan, "PEDOT:PSS interfaces stabilised using a PEGylated crosslinker yield improved conductivity and biocompatibility," *Journal of Materials Chemistry B*, vol. 7, no. 31, pp. 4811-4820, Aug 21, 2019.
- [99] S. N. Cheng, I. D'cruz, M. C. Wang, M. Leitch, and C. B. Xu, "Highly Efficient Liquefaction of Woody Biomass in Hot-

- Compressed Alcohol-Water Co-solvents,” *Energy & Fuels*, vol. 24, no. 9, pp. 4659-4667, Sep, 2010.
- [100] S. N. Cheng, C. Wilks, Z. S. Yuan, M. Leitch, and C. B. Xu, “Hydrothermal degradation of alkali lignin to bio-phenolic compounds in sub/supercritical ethanol and water-ethanol co-solvent,” *Polymer Degradation and Stability*, vol. 97, no. 6, pp. 839-848, Jun, 2012.
- [101] H. K. Nguyen, S. Fujinami, and K. Nakajima, “Elastic modulus of ultrathin polymer films characterized by atomic force microscopy: The role of probe radius,” *Polymer*, vol. 87, pp. 114-122, Mar 22, 2016.
- [102] D. Passeri, A. Bettucci, A. Biagioni, M. Rossi, A. Alippi, E. Tamburri, M. Lucci, I. Davoli, and S. Berezina, “Indentation modulus and hardness of viscoelastic thin films by atomic force microscopy: A case study,” *Ultramicroscopy*, vol. 109, no. 12, pp. 1417-1427, Nov, 2009.
- [103] V. M. M. B.V Derjaguin, Yu.P Toporov, “Effect of contact deformations on the adhesion of particles,” *Journal of Colloid and Interface Science*, vol. 53, no. 2, pp. 314-326, 1975.
- [104] B. V. D. V.M. Muller, Yu.P. Toporov, “On two methods of calculation of the force of sticking of an elastic sphere to a rigid plane,” *Colloids and Surfaces*, vol. 7, no. 3, pp. 251-259, 1983.
- [105] K. K. Kenneth Langstreth Johnson, A. D. Roberts, “Surface energy and the contact of elastic solids,” *Proc. R. Soc. Lond*, vol. 324, no. 1558, pp. 301-313, 1971.
- [106] C. Y. P. P. L. Anto, Hema Tresa Varghese and Daizy Philip, “Potential-dependent SERS profile of orthanilic acid on silver electrode,” *Journal of Raman Spectroscop*, vol. 37, pp. 1265-1271, 2006.
- [107] R. S. Mcdonald, “Surface Functionality of Amorphous Silica by

- Infrared Spectroscopy,” *Journal of Physical Chemistry*, vol. 62, no. 10, pp. 1168-1178, 1958.
- [108] A. A. Issa, and A. S. Luyt, “Kinetics of Alkoxysilanes and Organoalkoxysilanes Polymerization: A Review,” *Polymers*, vol. 11, no. 3, 537, Mar 21, 2019.
- [109] G. W. S. C. Jeffery Brinker, *Sol-Gel Science: The Physics and Chemistry of Sol-Gel Processing*, pp. 127: Academic Press, INC, 1990.
- [110] S. W. Kantor, “The Hydrolysis of Methoxysilanes - Dimethylsilanediol,” *Journal of the American Chemical Society*, vol. 75, no. 11, pp. 2712-2714, 1953.
- [111] B. R. Xu, S. A. Gopalan, A. I. Gopalan, N. Muthuchamy, K. P. Lee, J. S. Lee, Y. Jiang, S. W. Lee, S. W. Kim, J. S. Kim, H. M. Jeong, J. B. Kwon, J. H. Bae, and S. W. Kang, “Functional solid additive modified PEDOT: PSS as an anode buffer layer for enhanced photovoltaic performance and stability in polymer solar cells” *Scientific Reports*, vol. 7, 45079, May 4, 2017.
- [112] N. Massonnet, A. Carella, O. Jaudouin, P. Rannou, G. Laval, C. Celle, and J. P. Simonato, “Improvement of the Seebeck coefficient of PEDOT:PSS by chemical reduction combined with a novel method for its transfer using free-standing thin films,” *Journal of Materials Chemistry C*, vol. 2, no. 7, pp. 1278-1283, Feb 21, 2014.
- [113] S. Kim, H. S. Kim, and Y. D. Park, “Doped PEDOT:PSS electrodes, patterned through wettability control, and their effects on the electrical properties of polymer thin film transistors,” *Organic Electronics*, vol. 30, pp. 296-301, Mar, 2016.
- [114] Z. A. ALOthman, “A Review: Fundamental Aspects of Silicate Mesoporous Materials,” *Materials*, vol. 5, no. 12, pp. 2874-2902, Dec, 2012.
- [115] I. Simpson, B. Rose, and W. R. Loewenstein, “Size limit of

- molecules permeating the junctional membrane channels,” *Science*, vol. 195, no. 4275, pp. 294-296, Jan 21, 1977.
- [116] D. Huber, L. Petreanu, N. Ghitani, S. Ranade, T. Hromadka, Z. Mainen, and K. Svoboda, “Sparse optical microstimulation in barrel cortex drives learned behaviour in freely moving mice,” *Nature*, vol. 451, no. 7174, pp. 61-64, Jan 3, 2008.
- [117] J. Lee, I. Ozden, Y. K. Song, and A. V. Nurmikko, “Transparent intracortical microprobe array for simultaneous spatiotemporal optical stimulation and multichannel electrical recording,” *Nature Methods*, vol. 12, no. 12, pp. 1157-1162, Dec, 2015.
- [118] G. Shin, A. M. Gomez, R. Al-Hasani, Y. R. Jeong, J. Kim, Z. Q. Xie, A. Banks, S. M. Lee, S. Y. Han, C. J. Yoo, J. L. Lee, S. H. Lee, J. Kurniawan, J. Tureb, Z. Z. Guo, J. Yoon, S. I. Park, S. Y. Bang, Y. Nam, M. C. Walicki, V. K. Samineni, A. D. Mickle, K. Lee, S. Y. Heo, J. G. McCall, T. S. Pan, L. Wang, X. Feng, T. I. Kim, J. K. Kim, Y. H. Li, Y. G. Huang, R. W. Gereau, J. S. Ha, M. R. Bruchas, and J. A. Rogers, “Flexible Near-Field Wireless Optoelectronics as Subdermal Implants for Broad Applications in Optogenetics,” *Neuron*, vol. 93, no. 3, pp. 509-521, Feb 8, 2017.
- [119] V. K. Samineni, J. Yoon, K. E. Crawford, Y. R. Jeong, K. C. McKenzie, G. Shin, Z. Xie, S. S. Sundaram, Y. Li, M. Y. Yang, J. Kim, D. Wu, Y. Xue, X. Feng, Y. Huang, A. D. Mickle, A. Banks, J. S. Ha, J. P. Golden, J. A. Rogers, and R. W. t. Gereau, “Fully implantable, battery-free wireless optoelectronic devices for spinal optogenetics,” *Pain*, vol. 158, no. 11, pp. 2108-2116, Nov, 2017.
- [120] A. Abdo, M. Sahin, D. S. Freedman, E. Cevik, P. S. Spuhler, and M. S. Unlu, “Floating light-activated microelectrical stimulators tested in the rat spinal cord,” *Journal of Neural Engineering*, vol. 8, no. 5, 056012, Oct, 2011.
- [121] D. Seo, R. M. Neely, K. Shen, U. Singhal, E. Alon, J. M. Rabaey,

- J. M. Carmena, and M. M. Maharbiz, "Wireless Recording in the Peripheral Nervous System with Ultrasonic Neural Dust," *Neuron*, vol. 91, no. 3, pp. 529-539, Aug 3, 2016.
- [122] H. R. Eggert, and V. Blazek, "Optical properties of human brain tissue, meninges, and brain tumors in the spectral range of 200 to 900 nm," *Neurosurgery*, vol. 21, no. 4, pp. 459-464, Oct, 1987.
- [123] J. Defelipe, "The evolution of the brain, the human nature of cortical circuits, and intellectual creativity," *Front Neuroanat*, vol. 5, pp. 29, 2011.
- [124] Y. K. Song, J. Stein, W. R. Patterson, C. W. Bull, K. M. Davitt, M. D. Serruya, J. Zhang, A. V. Nurmikko, and J. P. Donoghue, "A microscale photovoltaic neurostimulator for fiber optic delivery of functional electrical stimulation," *Journal of Neural Engineering*, vol. 4, no. 3, pp. 213-218, Sep, 2007.
- [125] G. R. P. R.A. Brucea, "An improved Au-Ge-Ni ohmic contact to n-type GaAs," *Solid-State Electronics*, vol. 30, no. 7, pp. 729-737, 1987.
- [126] R. W. F. Clayton, D. Johnson, "Characterization of a Manufacturable High Rate GaAs Via Etch Process," *2002 CS Mantech Technical Digest*, pp. 121-124, 2002.
- [127] A. K. D.S. Rawal, H.S. Sharma, B.K. Sehgal, Hitendra K. Malik, "A Highly Selective Low Pressure Inductively Coupled Plasma Etching Process for GaAs Using Photoresist Mask," *The Open Plasma Physics Journal*, vol. 4, pp. 34-39, 2011.
- [128] H. Ning, J. Chen, Z. Fang, R. Tao, W. Cai, R. Yao, S. Hu, Z. Zhu, Y. Zhou, C. Yang, and J. Peng, "Direct Inkjet Printing of Silver Source/Drain Electrodes on an Amorphous InGaZnO Layer for Thin-Film Transistors," *Materials (Basel)*, vol. 10, no. 1, Jan 10, 51, 2017.
- [129] M. H. Tsai, W. S. Hwang, H. H. Chou, and P. H. Hsieh, "Effects

- of pulse voltage on inkjet printing of a silver nanopowder suspension,” *Nanotechnology*, vol. 19, no. 33, pp. 335304, Aug 20, 2008.
- [130] M. Kang, and K. T. Kang, “Flexible 2-Layer Paper Printed Circuit Board Fabricated by Inkjet Printing for 3-D Origami Electronics,” *International Journal of Precision Engineering and Manufacturing-Green Technology*, vol. 5, no. 3, pp. 421-426, Jul, 2018.
- [131] D. J. Finn, M. Lotya, and J. N. Coleman, “Inkjet printing of silver nanowire networks,” *ACS Appl Mater Interfaces*, vol. 7, no. 17, pp. 9254-9261, May 6, 2015.
- [132] J. Perelaer, C. E. Hendriks, A. W. M. de Laat, and U. S. Schubert, “One-step inkjet printing of conductive silver tracks on polymer substrates,” *Nanotechnology*, vol. 20, no. 16, pp. 165303, Apr 22, 2009.
- [133] H. L. Hao, L. K. Wu, W. J. Chung, Y. Zhang, and W. Z. Shen, “Process optimization of RTA on the characteristics of ITO-coated GaN-based LEDs,” *Microelectronics Reliability*, vol. 55, no. 11, pp. 2263-2268, Nov, 2015.
- [134] D. S. Rawal, H. K. Malik, V. R. Agarwal, A. K. Kapoor, B. K. Sehgal, and R. Muralidharan, “BCl₃/Cl₂-Based Inductively Coupled Plasma Etching of GaN/AlGa_N Using Photoresist Mask,” *Ieee Transactions on Plasma Science*, vol. 40, no. 9, pp. 2211-2220, Sep, 2012.
- [135] G. Y. Y. H. S. Kim, J. W. Lee, T. I. Kim, “Characteristics of inductively coupled Cl₂/BCl₃ plasmas during GaN etching,” *Journal of Vacuum Science & Technology A*, vol. 17, no. 4, pp. 2214-2219, 1999.
- [136] Z. X. Qin, Z. Z. Chen, Y. Z. Tong, X. M. Ding, X. D. Hu, T. J. Yu, and G. Y. Zhang, “Study of Ti/Au, Ti/Al/Au, and Ti/Al/Ni/Au ohmic

- contacts to n-GaN,” *Applied Physics a-Materials Science & Processing*, vol. 78, no. 5, pp. 729-731, Mar, 2004.
- [137] F. Zhang, L. P. Wang, E. S. Boyden, and K. Deisseroth, “Channelrhodopsin-2 and optical control of excitable cells,” *Nat Methods*, vol. 3, no. 10, pp. 785-792, Oct, 2006.
- [138] G. Nagel, M. Brauner, J. F. Liewald, N. Adeishvili, E. Bamberg, and A. Gottschalk, “Light activation of channelrhodopsin-2 in excitable cells of *Caenorhabditis elegans* triggers rapid Behavioral responses,” *Current Biology*, vol. 15, no. 24, pp. 2279-2284, Dec 20, 2005.
- [139] E. S. Boyden, F. Zhang, E. Bamberg, G. Nagel, and K. Deisseroth, “Millisecond-timescale, genetically targeted optical control of neural activity,” *Nature Neuroscience*, vol. 8, no. 9, pp. 1263-1268, Sep, 2005.
- [140] Y. P. Zhang, and T. G. Oertner, “Optical induction of synaptic plasticity using a light-sensitive channel,” *Nature Methods*, vol. 4, no. 2, pp. 139-141, Feb, 2007.

국 문 초 록

전기 자극은 현대 의학에 적용되고 수십 년에 걸쳐 개선된 가장 일반적인 신경 자극 기술이다. 그러나, 전기 자극 일반적으로 이웃 뉴런에 영향을 미치고 단일 세포 메커니즘의 분류를 어렵게 만든다. 광유전학의 발전은 이런 전기 자극의 단점을 보완해주었다. 빛에 의해 자극이 되기 때문에 선택적으로 자극이 가능하게 되었고, 신경 기록과 자극을 동시에 가능하게 되었다. 그러나 일반적으로 많이 쓰이는 Channelrhodopsin-2 (ChR2) 는 파랑 빛에 의해 자극이 이루어 지게 되고 이는 낮은 침투 두께로 깊은 영역에서의 빛에 의한 자극이 어려워지게 된다. 이를 극복하기 위해 깊은 침투 두께의 특징을 가지고 있는 근적외선(NIR, Near-infrared) 영역은 좀 더 깊은 영역에서의 신경 세포 자극이 용이하게 해 줄 수 있다.

전기적 방식의 신경 자극기에 경우, 전극의 특성은 매우 중요하며, 특히 전극의 임피던스 및 전하 주입 밀도는 전극을 평가 하는데 중요한 요소이다. 다양한 전극 물질 중에 Poly(3,4-ethylenedioxythiophene):poly(styrenesulfonate) (PEDOT:PSS) 는 생체 적합하며 낮은 임피던스를 가지고 있기 때문에 그에 대한 연구는 지속적으로 진행되고 있다.

본 학위 논문은 첨단 신경 공학 응용을 위한 광학 및 전

기 신경 자극기 개발 대해 다루고 있다. 전기적 신경 자극에서 전극 물질로서 PEDOT:PSS 의 연구는 낮은 임피던스와 높은 충전 저장 용량 (CSC, Charge Storage Capacity) 값을 가진다. 본 학위 논문에서는 에탄올의 추가로 기존의 PEDOT:PSS 물질과 비교하여 더 낮은 임피던스와 더 높은 CSC 값을 가지는 것을 보여준다. 이는 에탄올의 산화로 생긴 아세트산과 pH 값의 증가로 인한 이온화로 PEDOT 의 도핑 증가로 나타난다. 또한 에탄올의 추가는 가교제인 (3-glycidyloxypropyl)trimethoxysilane (GOPS) 의 향상 된 가교 효율을 보여준다. 에탄올의 추가로 인해 적은 양의 GOPS 함량에도 PEDOT:PSS-GOPS 의 기계적 특성 및 안정성의 증가는 신경 자극기로써 더욱 용이하게 쓰일 수 있다. 형광 전압 표식자 (Bongwoori-R3) 가 발현 된 포유류 세포 (HEK 293 cell)의 자극 실험을 통한 형광 변화는 PEDOT:PSS 전극의 실행 가능성을 확인하였다.

마지막으로, NIR 동작하는 광전지와 Blue LED를 결합하여 광유전학을 이용하여 깊은 영역에서의 신경 세포를 자극 시키는 기술을 개발하는 것을 다루고 있다. 이전 연구에서 NIR 광전지와 Blue LED 의 단순 결합은 NIR 의 방향과 파랑 빛의 방사 방향이 일치하여 더 깊은 곳으로의 신경 자극이 어려웠다. 그러나 이번 연구에서는 다양한 반도체 공정 및 용액 공정을

이용하여 NIR 광전지에 through hole via 를 적용하여 NIR 방향과 LED의 파랑 빛의 방향을 바꿔주어 더 깊은 곳으로의 신경 자극이 가능하도록 하였다. 또한 광전지와 LED가 결합된 자극기에 의해 ChR2가 발현된 포유류 세포 및 신경 세포에서 자극이 됨을 확인하였다.

학 번 : 2009-22457